

Die approbierte Originalversion dieser Diplom-/Masterarbeit ist an der Hauptbibliothek der Technischen Universität Wien aufgestellt (<http://www.ub.tuwien.ac.at>).

The approved original version of this diploma or master thesis is available at the main library of the Vienna University of Technology (<http://www.ub.tuwien.ac.at/englweb/>).

# Parametric Excitation in Microelectromechanical Systems (MEMS)

Master's Thesis

submitted in partial fulfillment of the requirements for the degree of

**Master of Science**

in

**Engineering**

by

**Johannes Welte**

Registration Number 0926313

To the Institute of Mechanics and Mechatronics  
at the Vienna University of Technology

Advisor: Ao.Univ.Prof. Dipl.-Ing. Dr.techn. Horst Ecker  
Assistance: Univ.Prof. Dipl.-Phys. Dr.rer.nat. Ulrich Schmid

Vienna, 21.03.2012

Vienna University of Technology  
A-1040 Vienna - Karlsplatz 13 - Tel. +43-1-58801-0 - [www.tuwien.ac.at](http://www.tuwien.ac.at)



# Acknowledgements

First of all I want to thank Prof. Dr. Horst Ecker for introducing me to the very interesting field of parametric excitation and giving me the opportunity to write this thesis. I very much appreciate the guidance and assistance provided throughout the whole development process along with the possibility to present my research findings at the 7<sup>th</sup> Vienna International Conference on Mathematical Modelling.

I would also like to thank Prof. Dr. Ulrich Schmid from the Institute of Sensor and Actuator Systems, Department for Microsystems Technology at the Vienna University of Technology for contributing his knowledge and providing useful literature references on microelectromechanical systems.



# Abstract

The present master's thesis deals with parametrically excited oscillations in microelectromechanical systems (MEMS). Parametric excitation occurs in mechanical systems, which are described by differential equations, whose coefficients are time-dependent. On the basis of a nonlinear parametrically excited MEMS with a single degree of freedom, the occurring resonance phenomena, as well as the influence of the nonlinearities are investigated. This is done using both an analytical method as well as numerical simulation. Similar single degree of freedom MEMS are already discussed in the relevant literature and possible applications are presented mainly in the field of sensor optimization and electronic filters.

Based on the investigations concerning the single degree of freedom system, a parametrically excited system with two degrees of freedom is created, which has not yet been investigated in connection with MEMS. The additional degree of freedom extends the frequency ranges in which parametric resonances occur. These additional regions of instability are determined and investigated by means of numerical simulation. Particular attention is paid to the so-called parametric anti-resonance effect. This phenomenon has, in contrast to the other parametric resonances, no destabilizing character, but on the contrary provides additional vibration damping. The related system parameters are then optimized with respect to the anti-resonance effect by applying a numerical parameter study. The final outcome of this thesis is a design proposal of the optimized system with the aim to manufacture the MEMS in a possible further step, in order to confirm the parametric anti-resonance effect experimentally.



# Kurzfassung

Die vorliegende Masterarbeit beschäftigt sich mit parametererregten Schwingungen in Mikro-Elektro-Mechanischen Systemen (MEMS). Parametererregung tritt bei mechanischen Systemen auf, die durch Differentialgleichungen beschrieben werden, deren Koeffizienten von der Zeit abhängen. Anhand eines nichtlinearen parametererregten MEMS mit einem Freiheitsgrad werden die auftretenden Resonanzphänomene sowie der Einfluss der Nichtlinearitäten untersucht. Dies erfolgt sowohl unter Zuhilfenahme einer analytischen Methode, als auch mittels numerischer Simulation. Ähnlich aufgebaute MEMS mit ebenfalls nur einem Freiheitsgrad sind in der einschlägigen Literatur ausführlich behandelt und mögliche Anwendungen werden vor allem im Bereich der Sensoroptimierung bzw. Filtertechnik aufgezeigt.

Aufbauend auf den Untersuchungen am Einfreiheitsgradsystem, wird ein parametererregtes System mit zwei Freiheitsgraden kreiert, welches im Kontext von MEMS noch nicht untersucht wurde. Durch den zusätzlichen Freiheitsgrad vermehren sich die Frequenzbereiche in denen Parameterresonanzen auftreten. Diese werden mit Hilfe von numerischer Simulation bestimmt und untersucht. Besonderes Augenmerk wird dabei auf die sogenannte parameter Anti-Resonanz gelegt. Diese besitzt im Gegensatz zu den restlichen Parameterresonanzen keinen destabilisierenden Charakter, sondern sorgt im Gegenteil für zusätzlich auftretende Schwingungsdämpfung. Weiterführend werden durch eine numerische Parameterstudie die Systemparameter in Hinblick auf ein maximales Auftreten des Anti-Resonanz Effektes optimiert. Das Endergebnis dieser Masterarbeit bildet ein Konstruktionsentwurf des optimierten Systems, mit dem Ziel dies in einem möglichen weiterführenden Arbeitsschritt in Hardware zu realisieren, um den Effekt der Anti-Resonanz messtechnisch zu bestätigen.



# Contents

<b>1</b>	<b>Introduction</b>	<b>1</b>
<b>2</b>	<b>Microelectromechanical systems</b>	<b>3</b>
2.1	Lithography . . . . .	3
2.2	Pattern transfer . . . . .	5
2.3	Wet bulk micromachining . . . . .	6
2.4	Surface micromachining . . . . .	8
2.5	LIGA . . . . .	10
<b>3</b>	<b>Parametric excitation</b>	<b>13</b>
3.1	Parametric resonance . . . . .	14
3.2	Parametric anti-resonance . . . . .	16
3.3	Methods for analyzing parametrically excited systems . . . . .	17
3.4	Perturbation analysis and averaging . . . . .	19
3.5	Floquet method . . . . .	21
<b>4</b>	<b>Parametric excitation in microelectromechanical systems</b>	<b>25</b>
4.1	Systems with one degree of freedom . . . . .	25
4.1.1	Mass sensor . . . . .	26
4.1.2	Electronic filter . . . . .	27
4.1.3	Parametric amplification . . . . .	29
4.2	Systems with multiple degrees of freedom . . . . .	30
<b>5</b>	<b>Investigation of a single degree of freedom parametrically excited MEMS</b>	<b>31</b>
5.1	Modeling . . . . .	31
5.1.1	Rescaling displacement and time . . . . .	34

## Contents

5.1.2	System parameters . . . . .	35
5.2	Stability investigation . . . . .	41
5.2.1	Analytical stability investigation . . . . .	41
5.2.2	Numerical stability investigation . . . . .	46
<b>6</b>	<b>Investigation of a two degree of freedom parametrically excited MEMS</b>	<b>53</b>
6.1	Modeling . . . . .	53
6.1.1	Rescaling displacement and time . . . . .	56
6.1.2	System parameters . . . . .	58
6.2	Linear system . . . . .	60
6.2.1	Numerical stability investigation . . . . .	60
6.2.2	Parameter study . . . . .	63
6.3	Nonlinear system . . . . .	82
6.3.1	Numerical stability investigation . . . . .	83
<b>7</b>	<b>Optimized MEMS design with respect to the parametric anti-resonance phenomenon</b>	<b>85</b>
7.1	Mechanical stiffness . . . . .	85
7.2	Electrostatic restoring force and mass ratio . . . . .	86
7.3	Damping . . . . .	88
7.4	Oscillator design . . . . .	88
<b>8</b>	<b>Conclusions and future work</b>	<b>91</b>
	<b>Bibliography</b>	<b>93</b>

# List of Figures

2.1	Basic photolithography and pattern transfer using a Si wafer and negative photoresist. . . . .	4
2.2	Classification of various dry etching techniques according to their setup. . . . .	6
2.3	Wet bulk micromachining process used to realize a pressure sensor. . . . .	7
2.4	Basic surface micromachining process sequence. . . . .	8
2.5	Scanning electron image of a MEMS oscillator. . . . .	9
2.6	Illustration of the basic LIGA process steps. . . . .	10
3.1	Strutt-Ince stability chart for a PE single degree of freedom oscillator. . . . .	14
3.2	Two mass system with self excitation due to negative damping $c_{02} < 0$ . . . . .	17
3.3	Stability chart for the system shown in Fig. 3.2. . . . .	18
4.1	Simulation results of a parametrically excited MEMS bandpass filter. . . . .	28
5.1	Basic design of a single degree of freedom MEMS oscillator. . . . .	32
5.2	Mechanical model of a single degree of freedom MEMS oscillator. . . . .	32
5.3	Basic layout of a single degree of freedom MEMS oscillator. . . . .	36
5.4	Mechanical models used for nonlinear finite element analyses. . . . .	37
5.5	Calculated force displacement curve using ABAQUS. . . . .	38
5.6	Detailed layout of the backbone with attached comb drive. . . . .	39
5.7	Nonlinear characteristics examined in the $\chi$ - $\lambda_3$ parameter space. . . . .	45
5.8	Amplitude responses for different sections corresponding to Fig. 5.7. . . . .	47
5.9	Frequency responses for different sections corresponding to Fig. 5.7. . . . .	48
5.10	Displacement plots near the first parametric resonance with $V_A = 20V$ . . . . .	49
5.11	First parametric region of instability. . . . .	50

## List of Figures

5.12	Oscillation and velocity amplitude of the nonlinear system at $\Omega = 2.02$ and $V_A = 20V$ . . . . .	50
6.1	Basic design of a two degree of freedom MEMS oscillator. . . . .	54
6.2	Mechanical model of a two degree of freedom MEMS oscillator. . . . .	54
6.3	Numerical study for PE-Frequency $\Omega$ and input voltage $V_A$ . . . . .	62
6.4	Numerical study for PE-Frequency $\Omega$ and input voltage $V_A$ showing first anti-resonance $\Omega_2 - \Omega_1$ . . . . .	62
6.5	Displacements $z_1, z_2$ at PE-Resonances $\Omega_1, 2\Omega_1, 2\Omega_2$ and $\Omega_1 + \Omega_2$ . . . . .	64
6.6	Displacements $z_1, z_2$ at PE-Frequency $\Omega = 2.2$ and first anti-resonance $\Omega_2 - \Omega_1$ . . . . .	65
6.7	Method to detect the maximum occurrence of the first anti-resonance $\Omega_2 - \Omega_1$ . . . . .	66
6.8	Numerical study for PE-Frequency $\Omega$ and mass $m_1$ . . . . .	69
6.9	Numerical study for PE-Frequency $\Omega$ and mass $m_2$ . . . . .	70
6.10	Numerical study for PE-Frequency $\Omega$ and damping coefficient $c_{01}$ . . . . .	71
6.11	Numerical study for PE-Frequency $\Omega$ and damping coefficient $c_{12}$ . . . . .	72
6.12	Numerical study for PE-Frequency $\Omega$ and damping coefficient $c_{02}$ . . . . .	73
6.13	Numerical study for PE-Frequency $\Omega$ and mechanical stiffness coefficient $k_{01}^{lin}$ . . . . .	74
6.14	Numerical study for PE-Frequency $\Omega$ and mechanical stiffness coefficient $k_{12}^{lin}$ . . . . .	75
6.15	Numerical study for PE-Frequency $\Omega$ and mechanical stiffness coefficient $k_{02}^{lin}$ . . . . .	76
6.16	Numerical study for PE-Frequency $\Omega$ and electrostatic coefficient $r_{1A}$ . . . . .	77
6.17	Numerical study for PE-Frequency $\Omega$ and alternating voltage amplitude $V_A$ . . . . .	78
6.18	Approximated global anti-resonance optimum for PE-Frequency $\Omega$ and stiffness coefficient $k_{02}^{lin}$ . . . . .	80
6.19	Stability charts showing first anti-resonance at $\Omega = \Omega_2 - \Omega_1$ with different sets of parameters. . . . .	81
6.20	Displacements $z_1, z_2$ at $\Omega = \Omega_2 - \Omega_1$ with different sets of parameters. . . . .	82
6.21	Displacements $z_1, z_2$ at PE-Resonances $2\Omega_1, 2\Omega_2, \Omega_1 + \Omega_2$ and $\Omega_2 - \Omega_1$ . . . . .	84
7.1	Calculated nonlinear force displacement relations for springs $k_{01}, k_{12}$ and $k_{02}$ . . . . .	87
7.2	MEMS design proposal for maximum occurrence of the anti-resonance effect. . . . .	89

# List of Tables

5.1	Nondimensional parameter definitions corresponding to Eq. (5.1.11). . . . .	35
5.2	Dimensions of the single degree of freedom MEMS oscillator. . . . .	36
5.3	Comparison of the stiffness coefficients for fixed-fixed and folded beam configuration. . . . .	38
5.4	Dimensions of the backbone and the non-interdigitated comb drive. . . . .	40
5.5	Calculated linear electrostatic stiffness $r_{1A}$ and cubic electrostatic stiffness $r_{3A}$ . . . . .	40
5.6	Parameter values of the single degree of freedom MEMS oscillator. . . . .	41
6.1	Nondimensional parameter definitions corresponding to Eqs. (6.1.11). . . . .	58
6.2	Parameter values of the two degree of freedom MEMS oscillator. . . . .	59
6.3	Nondimensional parametric resonances and combination resonances obtained through modal analysis. . . . .	61
6.4	Optimized parameter values of the linearized two degree of freedom MEMS. . . . .	68
7.1	Calculated beam lengths for springs $k_{01}$ , $k_{12}$ and $k_{02}$ using finite element analysis. . . . .	86
7.2	Optimized dimensions of the two degree of freedom MEMS oscillator. . . . .	89
7.3	Optimized system parameters of the two degree of freedom MEMS. . . . .	89



# CHAPTER 1

## Introduction

Microelectromechanical systems (MEMS) are becoming more and more important for all kinds of industrial applications, like filters in communication devices or sensors for example. To further improve the performance of such applications, the use of parametric excitation within MEMS has been investigated in recent developments. The objective was to take advantage of a parametric resonance. Since these investigations have been limited to systems with a single degree of freedom, the motivation for this thesis is to create and analyze a MEMS design with two degrees of freedom. This results not only in a wider range of parametric resonance frequencies to be used, but may also lead to a parametric anti-resonance phenomenon, which may improve the vibration damping of such systems. Modeling aspects of a MEMS with two degrees of freedom and some first and novel results are the focus of this thesis.

The following Chapter 2 provides a brief introduction to the most common MEMS manufacturing processes, trying to give the reader a better idea of how MEMS are fabricated and what types of materials are used. Subsequently, Chapter 3 deals with parametric excitation in general and outlines two methods that are used later in this thesis to analyze such systems. Chapter 4 reviews three recent investigations concerning parametric excitation within MEMS, including a mass sensor, an electronic bandpass filter as well as a parametric amplifier. The following Chapter 5 consist of a detailed investigation concerning a single degree of freedom MEMS oscillator including modeling aspects, parameter acquisition and stability analyses. Moreover, the effect of the nonlinearities on the system behavior is studied analytically as well as numerically. Chapter 6 deals with a MEMS oscillator consisting

of two degrees of freedom. First, a mathematical model is obtained and subsequently the system parameters are defined. Using numeric simulation the parametric anti-resonance effect is detected and the system parameters are optimized with respect to this phenomenon. Chapter 7 deals with the transformation of the optimized system parameters into a MEMS design concept. The last chapter summarizes the obtained findings and provides an outlook for future work.

# Microelectromechanical systems

In the relevant literature several terms are used when talking about microelectromechanical systems (MEMS). These include micromachining, microfabrication, micromanufacturing and microelectromechanical systems itself. These terms all refer to technical devices with physical dimensions in the micrometer range, or manufacturing processes which are therefore required. Additionally, MEMS stands for a combination of mechanical and electronic components in one device. In this thesis only the term microelectromechanical system or its acronym MEMS will be used.

This chapter provides a brief overview of the different processes, which are used to manufacture microelectromechanical systems. It starts with the important photolithographic process that is used to transfer a certain pattern onto a surface and continues with etching processes followed by micromachining and micromolding, respectively.

## 2.1 Lithography

The most common form of lithography in MEMS fabrication is the so-called photolithography. It basically consists of six different process steps which are shown in Fig. 2.1 for a Si wafer and a negative photoresist system.

Figure 2.1 A shows the first process step where a thin layer of oxide is grown on the wafer by raising the temperature up to between 900 and 1150 °C, providing in addition an oxygen rich atmosphere being either dry or humidified.

## 2.1. Lithography

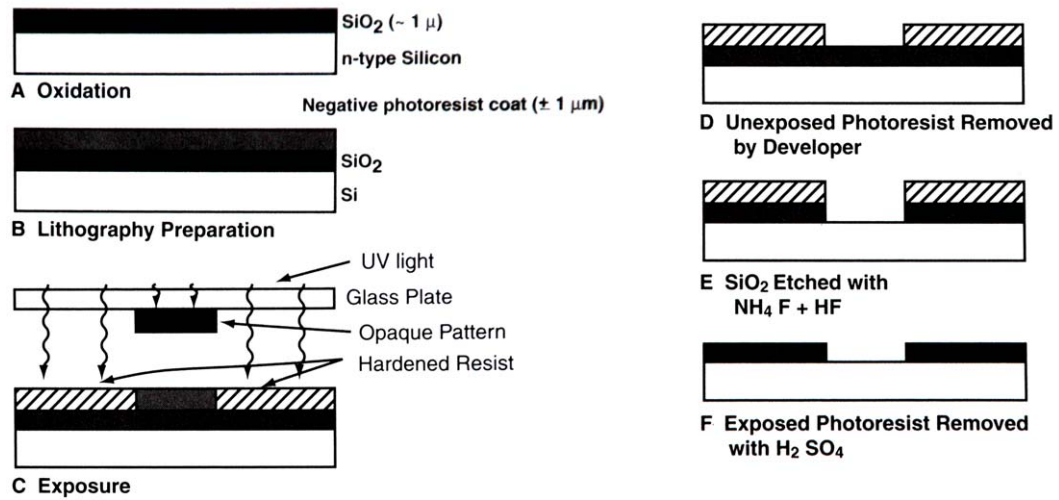


Figure 2.1: Basic photolithography and pattern transfer using a Si wafer and negative photoresist [8].

The following process step is shown in Fig. 2.1 B. A thin layer of a photoresist sensitive to ultraviolet radiation is deposited on the oxide surface. The wafer is then placed in a resist spinner where a vacuum chuck holds it in place. According to [8], the spinner rotates at a speed of about 1500 to 8000 rotations per minute (rpm). Due to the rotation of the wafer a uniform photoresist film is created on top of the oxide.

Subsequently, the wafer is exposed to an illumination unit, where the desired pattern is transferred via a mask into the resist. This can be seen in Fig. 2.1 C. Depending on the use of a positive or a negative resist, the illuminated areas will have different photochemical reactions during exposure. A positive resist typically becomes more soluble in developing solutions and a negative one strengthens itself. The wavelengths of the light source used for the exposure process can vary from extreme ultraviolet (EUV) (10 to 14 nm) to deep ultraviolet (DUV) (150 to 300 nm) to near ultraviolet (UV) (350 to 500 nm).

During development (see Fig. 2.1 D) the unexposed negative photoresist is removed by the developer. The remaining photoresist serves as a mask for upcoming subtractive or additive process steps, which will be covered in Chapter 2.2. The two main technologies used for developing are wet and dry development. The first one is, according to [8], mainly used for circuit and miniaturization manufacture in general, while the latter one is more and more used for some ultimate line width resolution applications.

After the development process a so-called de-scumming and postbaking process fol-

lows. With de-scumming remaining undesired photoresist can be removed from the wafer and postbaking among other things increases the resistance of the photoresist to following etching processes (see Fig. 2.1 E). The various etching principles are covered in more detail in Chapter 2.2 and 2.3.

The last step of the photolithographic process shown in Fig. 2.1 F is called resist stripping. Its objective is to completely remove the exposed photoresist without damaging the oxide film placed underneath. In [8] various sorts of liquids are mentioned to be used for wet stripping, including strong acids such as  $H_2SO_4$ , organic solvent strippers, alkaline strippers and acetone. Dry stripping on the other hand is growing in application, because of its fewer disposal problems, less corrosion of metal features and less undercutting and broadening of photoresist features.

## 2.2 Pattern transfer

Pattern transfer is understood as the process of transferring a desired structure onto a wafer, respectively its oxide layer (see Fig. 2.1 E). This transfer can be carried out either with subtractive or additive processes. Both processes will be described in the following, beginning with the subtractive dry etching technique.

Dry etching is a manufacturing process where a certain solid material is etched away physically, chemically, or by a combination of both. Figure 2.2 shows a classification of various dry etching techniques according to the required setup. Glow discharge techniques use plasma that is generated in the same vacuum chamber where the wafer is located. In contrast, ion-beam techniques use plasma that is generated in a separate chamber and then redirected in a beam towards the wafer.

Ion etching or sputtering is a technique where a surface is bombarded with ions of sufficient energy, which causes ballistic material ejection. The kinetic energy of the ions largely dictates the events that occur at the bombarded surface. For sputtering, the ion energy needs to be about 10 to 5000 eV. Ion beam milling is a manufacturing technique where the plasma source is decoupled from the substrate. Therefore a triode setup is needed. Plasma etching uses reactive neutral chemical species (e.g. chlorine or fluorine atoms) and molecular species generated in the plasma to diffuse to the substrate where they form volatile products with the layer to be removed. The plasma thereby supplies gaseous, reactive etchant species. Deep reactive ion etching is another manufacturing process mainly used to realize

### 2.3. Wet bulk micromachining

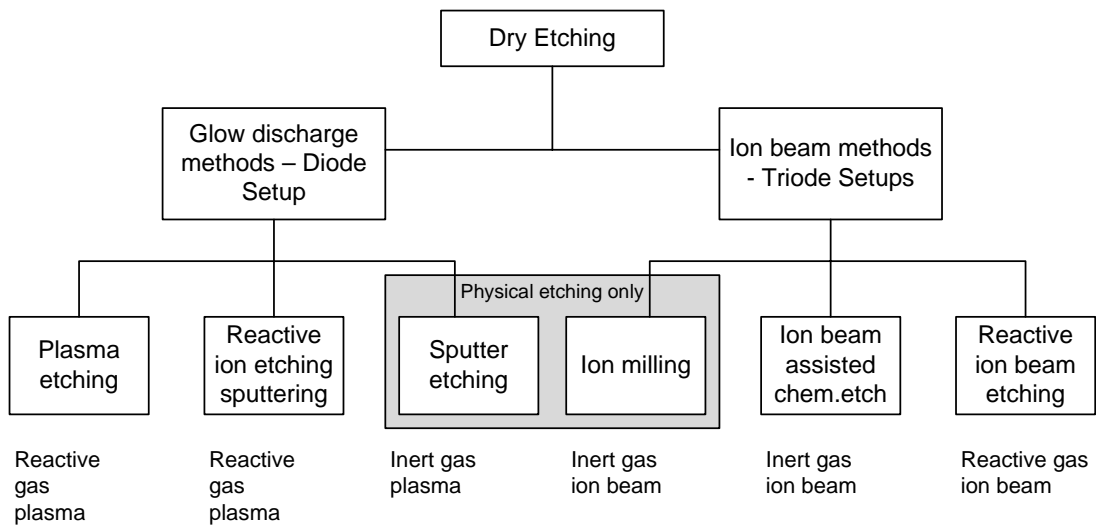


Figure 2.2: Classification of various dry etching techniques according to their setup, adapted from [8].

high aspect ratios. [8]

In comparison to the subtractive manufacturing processes, the additive ones deposit solids onto a wafer using different techniques. Such common techniques are for example the oxidation of silicon (see Fig. 2.1 A), physical and chemical vapour deposition, silk-screening, sol-gel deposition, tape casting and plasma spraying.

## 2.3 Wet bulk micromachining

Wet Bulk Micromachining is a technique to build features in the bulk of a material by wet etching. This can be achieved either with an isotropic or an anisotropic process, depending on the used etchant. Figure 2.3 shows a typical wet bulk micromachining process used to realize a membrane with piezoresistive elements.

The most common used wafer material for wet bulk micromachining is silicon, but quartz, crystalline Ge, SiC, GaAs, GaP and InP may also be used. Especially for mechanical components in MEMS silicon is widely spread because of its advantageous properties. Its density is lower than that of aluminum and the Young's modulus is approaching that of stainless steel and is certainly above that of quartz. The yield strength is even higher than that of steel and moreover single crystal silicon can be made practically without defects, which means that at room temperature silicon can be deformed only elastically. All these

### 2.3. Wet bulk micromachining

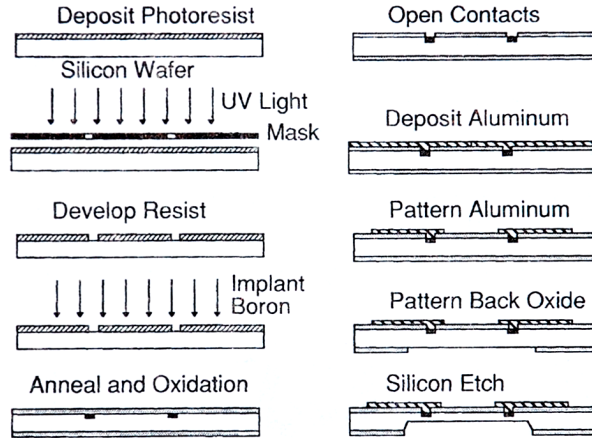


Figure 2.3: Wet bulk micromachining process used to realize a pressure sensor [8].

properties make silicon a material superior to any metal in most MEMS applications. [8]

For strength or stiffness calculations one has to keep in mind, that single crystal silicon has orthotropic material behavior, which leads to different mechanical stiffness values, depending on the orientation of the material. The most common use of the orthotropic expressions for silicon, according to [16], is to provide the elasticity values in the frame of reference of a standard (100) silicon wafer. Equation 2.3.1 shows the emerging orthotropic stiffness matrix with its values given in GPa.

$$\begin{bmatrix} \sigma_1 \\ \sigma_2 \\ \sigma_3 \\ \sigma_4 \\ \sigma_5 \\ \sigma_6 \end{bmatrix} = \begin{bmatrix} 194.5 & 35.7 & 64.1 & 0 & 0 & 0 \\ 35.7 & 194.5 & 64.1 & 0 & 0 & 0 \\ 64.1 & 64.1 & 165.7 & 0 & 0 & 0 \\ 0 & 0 & 0 & 79.6 & 0 & 0 \\ 0 & 0 & 0 & 0 & 79.6 & 0 \\ 0 & 0 & 0 & 0 & 0 & 50.9 \end{bmatrix} \begin{bmatrix} \epsilon_1 \\ \epsilon_2 \\ \epsilon_3 \\ \epsilon_4 \\ \epsilon_5 \\ \epsilon_6 \end{bmatrix} \quad (2.3.1)$$

As can be seen in Fig. 2.3, wet etching is a vital step in the process of bulk micromachining. Wet etching is in general used for cleaning, shaping three-dimensional structures, polishing and characterizing structural and compositional features. Compared to dry etching, wet etching is usually faster. Isotropic etchants remove material in all crystallographic directions at the same rate, whereas orthotropic etchants etch at different rates depending on the orientation of the wafer. The most common etchants for isotropic etching of silicon are mixtures of nitric acid ( $\text{HNO}_3$ ) and hydrofluoric acids (HF). For anisotropic etching a wider variety of etchants can be used including KOH as standard etchant, as well as NaOH, LiOH, CsOH, RbOH and  $\text{NH}_4\text{OH}$ . Anisotropic wet etching has several advantages over

## 2.4. Surface micromachining

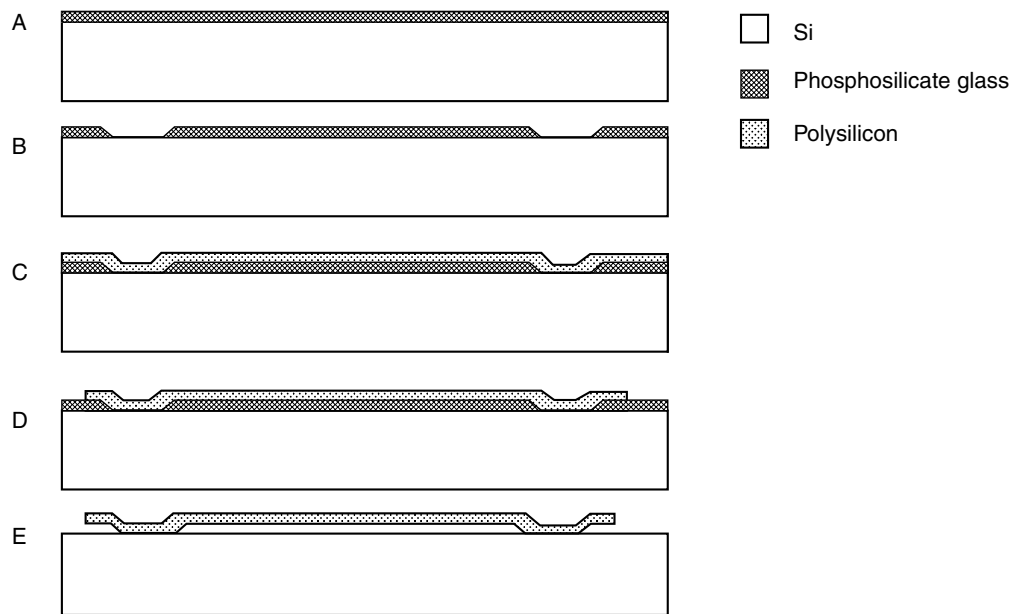


Figure 2.4: Basic surface micromachining process sequence [8].

orthotropic wet etching due to the gain of lateral control, but it also has some disadvantages like very small etching rates ( $< 1\mu\text{m}/\text{min}$  compared to tens of microns per min for isotropic wet etching) and high operating temperatures (80 to 115 °C), precluding many simple masking options. These disadvantages can be compensated using an anisotropic dry etching process like deep reactive ion etching for example. [8]

## 2.4 Surface micromachining

While in wet bulk micromachining structures are etched into the substrate, surface micromachined features are built up layer by layer. Dry etching is therefore used to create the surface features in the plane parallel to the wafer top face and dry etching releases them from that plane by undercutting. Figure 2.4 shows a basic surface micromachining process sequence.

The first process step may comprise to place a thin dielectric insulator layer on the silicon substrate. Then a so-called spacer layer is deposited on the silicon substrate. This is shown in Fig. 2.4 A. Next, the spacer layer needs to be densified by heating the wafer up to 950 to 1100 °C. This enables a uniform etch rate. The next step is to pattern the spacer layer

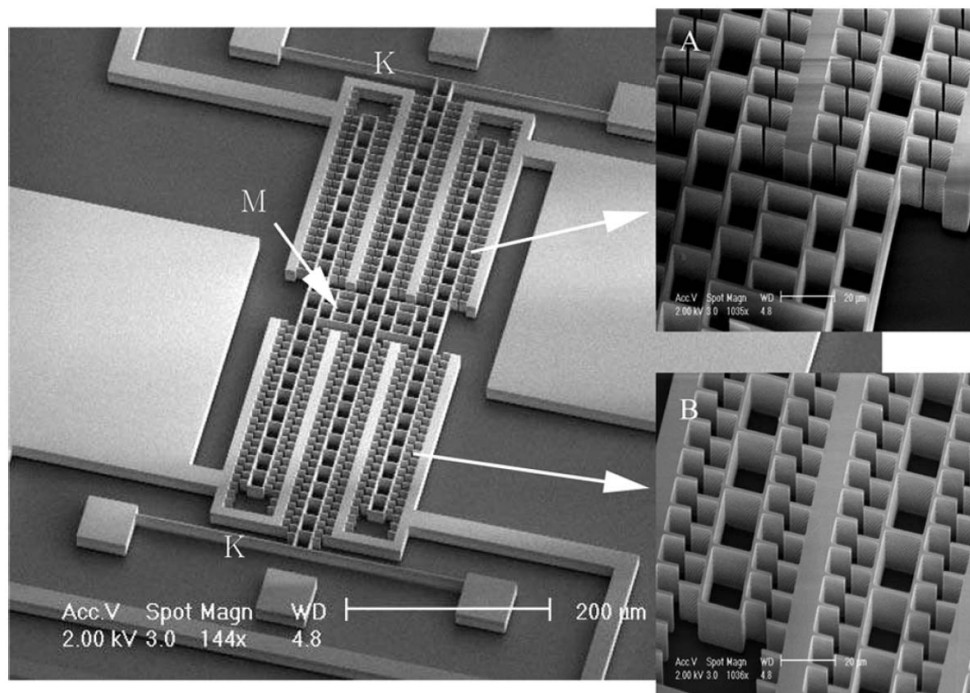


Figure 2.5: Scanning electron image of a MEMS oscillator [3].

with a mask that consists of the desired layout (see Fig. 2.4 B). A microstructural thin film is then deposited over the spacer layer and again patterned by a second mask and usually a dry etching technique (see Fig. 2.4 C and D). The last step of the surface micromachining process is a selective etching of the spacer layer to gain a freestanding micromechanical structure (see Fig. 2.4 E). A surface micromachining stack may contain up to five spacer and five structural layers. [8]

As the surface micromachining process is capable of producing complex MEMS structures it is of vital importance for this thesis. For that reason an example of a MEMS oscillator manufactured using surface micromachining is presented in Fig. 2.5.

The oscillator consists of two non-interdigitated comb drives (A and B), two flexures (K) and a backbone (M). By applying an AC signal to the comb drives the backbone is able to perform an oscillating vertical movement due to the arising electrostatic forces. A detailed analysis of such a MEMS oscillator can be found in Chapter 5.

Additionally to the well established surface micromachining processes, silicon on insulator (SOI) is an alternative approach to manufacture MEMS. In SOI the typically used bulk silicon wafers are replaced by wafers that have three layers. A thin surface layer of silicon,

## 2.5. LIGA

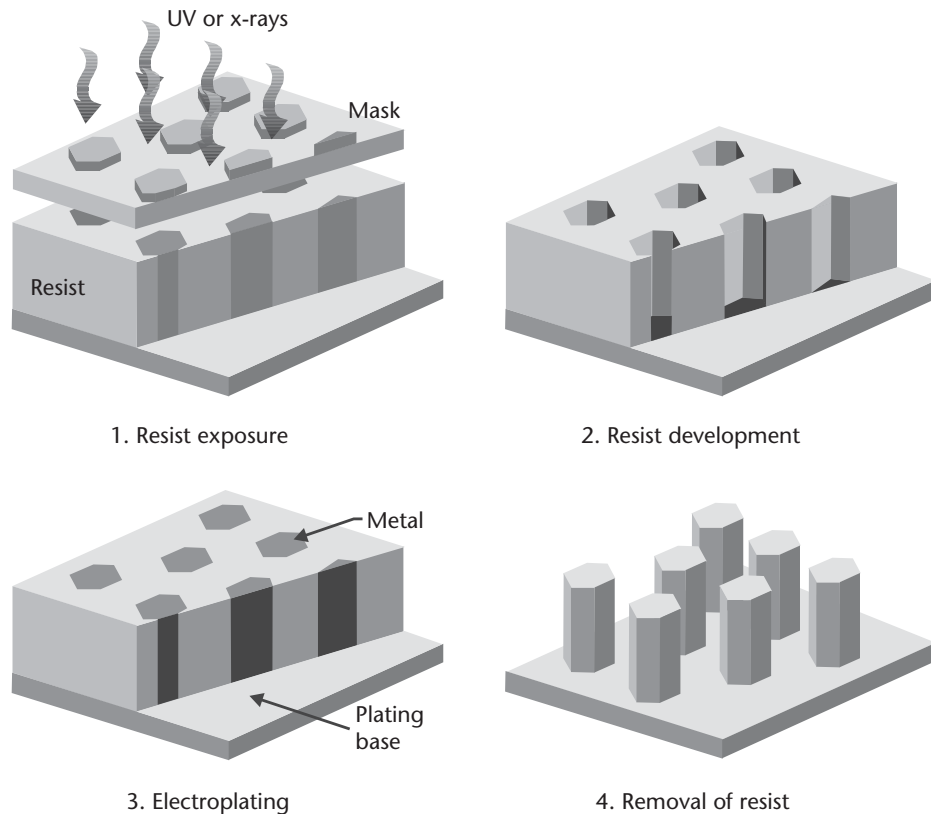


Figure 2.6: Illustration of the basic LIGA process steps [9].

an underlying layer of insulating material and a supporting silicon layer. In most cases SOI surface micromachining uses dry anisotropic etching to pattern a certain structure into the silicon layer on top of the insulator. These structures are then undercut by etching the sacrificial buried  $\text{SiO}_2$  insulator layer.

## 2.5 LIGA

LIGA is a German acronym for the process steps lithography, electroplating and micro-molding. It refers to a special surface micromachining technique that was invented in Germany at the beginning of the 1980s. The process is very suitable for producing microstructures with high aspect ratios and features materials such as metals, plastics and ceramics. The basic process steps of the LIGA technique are shown in Fig. 2.6.

First the substrate gets covered with an electrical seed layer, typically through sputtering or evaporation. Afterwards a polymer layer (resist) is placed on top of it. After soft-baking

a certain pattern is deposited on the polymer by an X-Ray or UV lithographic process (see Fig. 2.6 1). During the development process, which can be seen in Fig. 2.6 2, the resist is patterned. After development the microstructures are dried. At that stage the microstructure can be the final product, or as shown in Fig. 2.6 3, can be used for additional electroplating. In this process step a certain metal is plated into the voids left by the removed resist. Finally the resist and sometimes even the seed layer are stripped off (see Fig. 2.6 4). This can be done with either a solvent or plasma etching. [6]



## Parametric excitation

This chapter is devoted to parametric excitation (PE) in engineering systems and the various methods used to analyze it. The research on parametrically excited systems dates back to 1831 when M. Faraday studied sloshing liquids in a container. In 1868 E. Mathieu introduced his famous equation named after him, which paved the way for further investigations into parametric excitation, that are still going on at present.

A mechanical or electronic system is called parametrically excited, if its related differential equation consists of time varying coefficients. These coefficients could be for example the mass, stiffness or damping of the system. Some engineering systems that exhibit parametric excitation are for instance an axially excited beam, a sloshing liquid, a simple pendulum with a time dependent effective length or a parallel tuned electronic circuit with a time variant capacitance. These systems can all be mathematically modeled by the aforementioned Mathieu equation or a slight alteration of it

$$\ddot{x} + (\omega_0^2 + a \cos \omega t)x = 0. \quad (3.0.1)$$

The Hill equation is a more generalized version of the Mathieu equation where the excitation function  $f(t)$  is periodic but not necessarily harmonic

$$\ddot{x} + (\omega_0^2 + f(t))x = 0. \quad (3.0.2)$$

The main reason for applying parametric excitation to engineering systems is that they may exhibit special vibration responses which are called parametric resonances. This phenomenon will be covered in the next two sections.

### 3.1. Parametric resonance

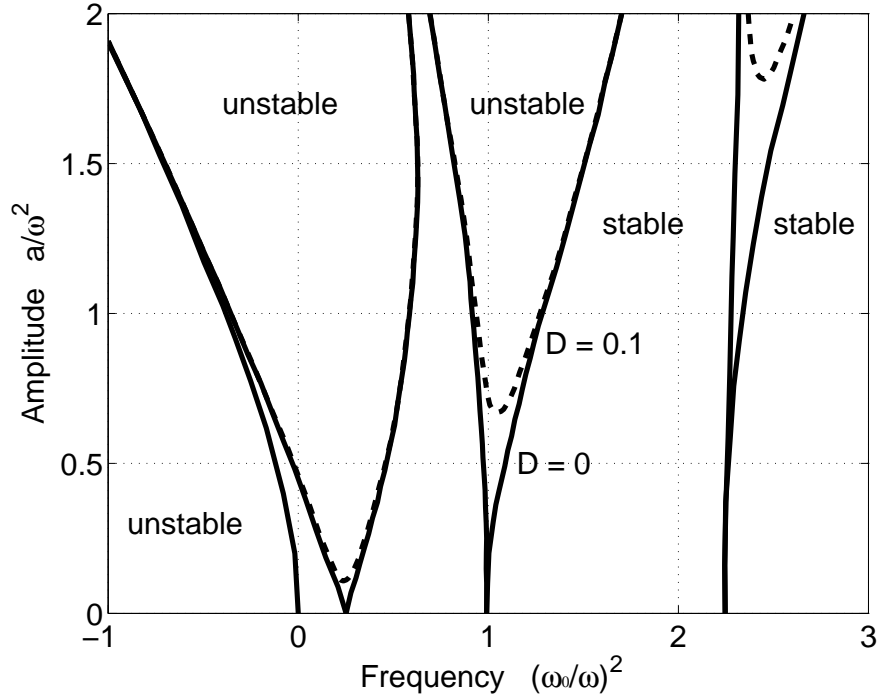


Figure 3.1: Strutt-Ince stability chart for a parametrically excited single degree of freedom oscillator [5].

## 3.1 Parametric resonance

The effect of parametric resonances can be shown best by establishing the so-called Strutt-Ince stability chart for the Mathieu equation given in Eq. (3.0.1). Such a stability chart is depicted in Fig. 3.1, showing the system behavior as a function of the normalized and squared values of the parametric excitation frequency and amplitude.

If the case where  $a = 0$  is first analyzed, it is quite obvious that Eq. (3.0.1) can be rewritten as follows

$$\ddot{x} + \omega_0^2 x = 0. \quad (3.1.1)$$

It is well known that for positive values of  $\omega_0^2$  the solution of the above mentioned second order differential equation consists of periodic trigonometric functions with an angular frequency of  $\omega_0$ . These harmonic oscillations can be considered as stable and are represented by the positive  $(\omega_0/\omega)^2$  axis in Fig. 3.1. If  $\omega_0^2$  is considered to be negative, the solution to the differential equation consists of exponential functions with a positive exponent. Due to

the exponential growth of the vibration amplitude, the system is said to be unstable, which is represented by the negative  $(\omega_0/\omega)^2$  axis in Fig. 3.1.

If the parametric excitation amplitude  $a$  is considered to be of a constant value, the oscillators system behavior represented by Eq. (3.0.1) is determined by the coefficient  $\omega_0^2$ . As can be seen in Fig. 3.1, the roots of the instability regions intersect with the frequency axis at distinct values of

$$\left(\frac{\omega_0}{\omega}\right)^2 = \left(\frac{n}{2}\right)^2, \quad (n = 1, 2, 3, \dots). \quad (3.1.2)$$

The width of the instability regions is decreasing with growing numbers of  $n$ . This occurs due to damping effects, which have obviously not been accounted in this examination, but always exist within practical problems. Additionally, in [5] the author mentions that the excitation amplitude  $a$  needs to exceed a certain critical value of

$$a_{critical} \approx D^{1/n}, \quad (3.1.3)$$

to destabilize the system, where  $D$  represents the damping coefficient of the oscillating system. This condition indicates that higher order parametric resonances ( $n > 2$ ) are of no vital importance.

In [2], the author carries out detailed stability investigations on the Mathieu equation and postulates that a parametrically excited single degree of freedom system may exhibit principle parametric resonances at angular frequencies of

$$\omega = \frac{2\omega_0}{n}, \quad (n = 1, 2, 3, \dots), \quad (3.1.4)$$

where  $\omega_0$  is the natural frequency of the oscillator and  $n$  represents the order of the parametric resonance being any integer number greater or equal to one. This more general expression is consistent with the one given in Eq. (3.1.2).

Expanding the investigations done so far to parametrically excited systems with multiple degrees of freedom, may lead to the following differential equation in matrix form

$$\ddot{\mathbf{x}} + (\mathbf{\Omega}^2 + \mathbf{A} \cos \omega t)\mathbf{x} = 0, \quad (3.1.5)$$

with  $k$  generalized coordinates (degrees of freedom). The  $\mathbf{\Omega}$  matrix consists of the natural frequencies of the system, whereas the  $\mathbf{A}$  matrix denotes the parametric excitation amplitudes at frequency  $\omega$

### 3.2. Parametric anti-resonance

$$\mathbf{x} = \begin{bmatrix} x_1 \\ \vdots \\ x_k \end{bmatrix}, \quad \mathbf{\Omega}^2 = \begin{bmatrix} \omega_1^2 & & \\ & \ddots & \\ & & \omega_k^2 \end{bmatrix}, \quad \mathbf{A} = \begin{bmatrix} a_{11} & \dots & a_{1k} \\ \vdots & \ddots & \vdots \\ a_{k1} & \dots & a_{kk} \end{bmatrix}. \quad (3.1.6)$$

Even if the Mathieu equation has been expanded to  $k$  degrees of freedom, the resonance condition (3.1.4) is still valid. It just gets supplemented by the additional natural frequencies  $\omega_j$

$$\omega = \frac{2\omega_j}{n}, \quad (n = 1, 2, 3, \dots), \quad (j = 1, \dots, k). \quad (3.1.7)$$

A very interesting phenomenon that appears in parametrically excited systems with multiple degrees of freedom are the so-called parametric combination resonances. Such a system not only has instability regions at multiples of the existing natural frequencies, but also at combinations of those frequencies and multiples of it [4]

$$\omega = \frac{\omega_i \pm \omega_j}{n}, \quad (n = 1, 2, 3, \dots), \quad (i, j = 1, \dots, k). \quad (3.1.8)$$

The additive combination resonances in Eq. (3.1.8) are of the same characteristic as the parametric resonances obtained from Eq. (3.1.4). The subtractive combination resonances on the other hand are often referred to as parametric anti-resonances [5]. This type of resonance will be covered in more detail in the next section.

## 3.2 Parametric anti-resonance

The parametric anti-resonances occurring at frequencies  $(\omega_i - \omega_j)/n$  have different characteristics than parametric resonances and also additive combination resonances. Investigating a parametrically excited system with more than one degree of freedom in the time domain shows, that if the system is excited by a small perturbation with a certain amplitude and frequency (no PE resonance frequency), the resulting system vibration will decrease with time. Given that situation one may call this a stable system behavior. If, on the other hand, the system is excited by a frequency near a parametric resonance or (additive) combination resonance, the resulting vibration will increase with time and therefore the system is said to be unstable. If in a third case the system is excited at a frequency near a parametric anti-resonance it will again show stable behavior and the resulting system vibrations

### 3.3. Methods for analyzing parametrically excited systems

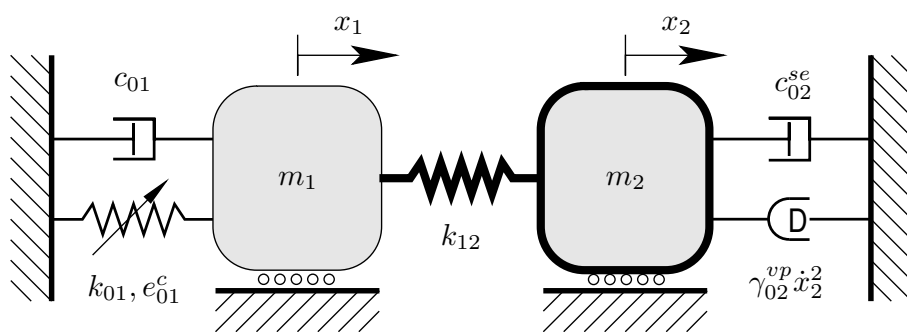


Figure 3.2: Two mass system with self excitation due to negative damping  $c_{02} < 0$  [5].

will decrease with time. They will, in fact, decrease even faster than at any other (stable) parametric excitation frequency. This characteristic can be of advantage when used in an engineering system. H. Ecker has for example shown in [5] the great potential of suppressing self excited vibrations by parametric excitation. In the following, one example discussed in that work is briefly presented for better understanding of the anti-resonance phenomenon and its potential beneficial usage.

The system to be considered is a mechanical two mass oscillator, shown in Fig. 3.2. One mechanical stiffness coefficient is periodically changed according to  $k_{01}(t) = k_{01}(1 + e_{01}^c \cos \omega t)$ . The damping element  $c_{02}$  is designed to act as a negative damper in order to force the system to exhibit self excited vibrations.

To investigate the characteristics of the present system, the author carries out a numerical stability analysis for the critical value of the negative damping parameter  $c_{02}$ . The resulting stability chart can be seen in Fig. 3.3, where the stable region is colored white and the unstable region is colored grey.

One can see easily the positive effect of the anti-resonance at  $\Omega_2 - \Omega_1$ , as the coefficient  $c_{02}$ , responsible for the self excitation mechanism, can take greater absolute values without destabilizing the system. This effect can be turned upside down by varying the stiffness  $k_{01}$  at the additive combination resonance frequency  $\Omega_1 + \Omega_2$ .

### 3.3 Methods for analyzing parametrically excited systems

Since parametric excitation has been investigated for such a long time, a wide range of mathematical methods are available to study the behavior of such systems. These methods all have different advantages and disadvantages, various fields of practicability and limita-

### 3.3. Methods for analyzing parametrically excited systems

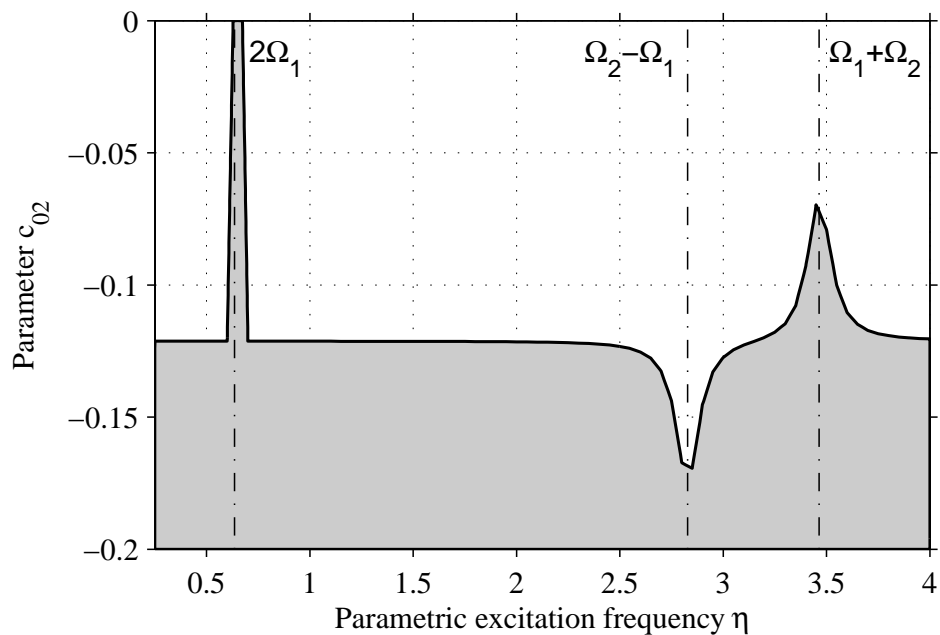


Figure 3.3: Stability chart for the system shown in Fig. 3.2 [5].

tions of application. This chapter tries to give a very brief overview of common analyzing methods concerning parametric excitation and deals with two of them in more detail. A more extensive discussion on analyzing systems with periodic coefficients, along with practical literature references, can be found in [5].

The most common methods to analyze differential equations with time periodic coefficients are listed below:

- Method of successive approximation
- Averaging method
- Tondl-Floquet method
- Harmonic balance
- Method of multiple scales
- Poincaré-Linsted method
- Method by E.Mettler

- Numerical methods

The selection of one of the above mentioned methods is depending on the characteristics of the system to be analyzed. It is for example of vital importance to know if the system is linear or at least can be linearized. Among other factors the dimension of the system is of importance as well. In this thesis the averaging method and a numerical method based on Floquet's theorem are along with simple numerical simulation used to analyze the parametrically excited oscillators presented in Chapter 5 and 6, respectively. Therefore these two methods will be explained in more detail in the following two sections.

### 3.4 Perturbation analysis and averaging

Perturbation analysis or theory is a method to approximate solutions for mathematical problems e.g. differential equations. By applying a singular perturbation, a small parameter (mostly labeled  $\epsilon$ ) is introduced and multiplied with the highest derivative of the differential equation. The emerging problem, including the parameter  $\epsilon$ , has the solution  $x(t, \epsilon)$ . Additionally an unperturbed problem with a solution of the form  $x(t, 0)$  is defined. One obtains a singular perturbation problem if the normed difference of the two solutions  $x(t, \epsilon)$  and  $x(t, 0)$  does not tend to zero when the parameter  $\epsilon$  tends to zero. [19]

For this thesis only singular perturbation, in particular the averaging method, will be used to analyze differential equations. In order to get a better understanding of the averaging method, an example is carried out in the following. Therefore the already mentioned Mathieu equation is used to demonstrate all necessary calculation steps. Based on an example mentioned in [19], Eq. (3.0.1) is simplified by defining its parameters as follows

$$\omega_0^2 = 1, \quad a = 4\epsilon, \quad \omega = 2. \quad (3.4.1)$$

Carrying out these substitutions leads to a Mathieu equation of the following form

$$\ddot{x} + (1 + 4\epsilon \cos(2t))x = 0. \quad (3.4.2)$$

If the perturbation parameter  $\epsilon$  is set to zero, Eq. (3.4.2) can be rewritten as

$$\ddot{x} + x = 0, \quad (3.4.3)$$

### 3.4. Perturbation analysis and averaging

with the solution of the differential equation known to be

$$x(t) = a_0 \cos(t) + b_0 \sin(t) = r_0 \cos(t + \psi_0). \quad (3.4.4)$$

The parameters  $r_0$  and  $\psi_0$  are determined by the initial conditions. To study the perturbed problem, these two parameters are considered to be functions of the time  $t$ . So Eq. (3.4.4) can be rewritten as

$$x(t) = r(t) \cos(t + \psi(t)). \quad (3.4.5)$$

To obtain another condition for the three unknowns  $y$ ,  $a$  and  $\psi$  Eq. (3.4.4) is differentiated with respect to the time  $t$

$$\dot{x}(t) = -r_0 \sin(t + \psi_0) = -r(t) \sin(t + \psi(t)). \quad (3.4.6)$$

The derivative of Eq. (3.4.5) yields the following equation

$$\dot{x}(t) = -r \sin(t + \psi) + \dot{r} \cos(t + \psi) - r\dot{\psi} \sin(t + \psi). \quad (3.4.7)$$

Comparing Eq. (3.4.6) and (3.4.7) results in the following condition

$$\dot{r} \cos(t + \psi) - r\dot{\psi} \sin(t + \psi) = 0. \quad (3.4.8)$$

By differentiating Eq. (3.4.6) with respect to the time  $t$  one obtains

$$\ddot{x}(t) = -r \cos(t + \psi) - \dot{r} \sin(t + \psi) - r\dot{\psi} \cos(t + \psi), \quad (3.4.9)$$

which enables to substitute for  $\ddot{x}$  and  $x$  in the Mathieu equation. This results in the following condition

$$-\dot{r} \sin(t + \psi) - r\dot{\psi} \cos(t + \psi) + 4\epsilon r \cos(2t) \cos(t + \psi) = 0. \quad (3.4.10)$$

Equations (3.4.8) and (3.4.10) form a system of algebraic equations. Solving that problem for the derivatives  $\dot{r}$  and  $\dot{\psi}$  results in the following two equations

$$\dot{r} = 4\epsilon r \sin(t + \psi) \cos(2t) \cos(t + \psi), \quad (3.4.11)$$

$$\dot{\psi} = 4\epsilon \cos^2(t + \psi) \cos(2t). \quad (3.4.12)$$

Both equations show that for a small parameter value of  $\epsilon$ , also  $\dot{r}$  and  $\dot{\psi}$  will be small. Moreover,  $r$  and  $\psi$  will change slower with time compared to the argument of the trigonometric function  $t + \psi$ . This characteristic can be used to average Eqs. (3.4.11) and (3.4.12) over one period ( $2\pi$ ) resulting in

$$\dot{r}_a = \frac{2\epsilon r}{\pi} \int_0^{2\pi} \sin(t + \psi) \cos(2t) \cos(t + \psi), \quad (3.4.13)$$

$$\dot{\psi}_a = \frac{2\epsilon}{\pi} \int_0^{2\pi} \cos^2(t + \phi) \cos(2t). \quad (3.4.14)$$

Carrying out the integrations results in the averaged expressions  $\dot{r}_a$  and  $\dot{\psi}_a$  given below

$$\dot{r}_a = \epsilon r_a \sin(2\psi_a), \quad (3.4.15)$$

$$\dot{\psi}_a = \epsilon \cos(2\psi_a). \quad (3.4.16)$$

The presented averaging method is applied to the parametrically excited MEMS oscillator covered in Chapter 5, to investigate the characteristics of the occurring nonlinearities and approximate the first parametric region of instability. An expansion of the averaging method to systems with multiple degrees of freedom is discussed in [5].

## 3.5 Floquet method

The Floquet method, as it is presented here, allows one to determine the stability of a differential equation with time periodic coefficients. This method is postulated in [5] and will briefly be repeated in the following.

The method based on Floquet's theorem reduces the computational time significantly compared to a straight forward numerical simulation, but can in return only be applied to systems represented by linear homogeneous ordinary differential equations with time periodic coefficients. Furthermore the method only indicates if the analyzed system is stable or unstable.

Assuming a system of first order differential equations with a  $T$ -periodic matrix  $\mathbf{A}(\tau)$

$$\mathbf{y}' = \mathbf{A}(\tau)\mathbf{y}, \quad (3.5.1)$$

$$\mathbf{A}(\tau) = \mathbf{A}(\tau + T), \quad (3.5.2)$$

### 3.5. Floquet method

Floquet's theorem suggests that each fundamental matrix  $\mathbf{M}(\tau)$  of the system can be represented as a product of two factors

$$\mathbf{M}(\tau) = \mathbf{P}(\tau)e^{\mathbf{C}\tau}, \quad (3.5.3)$$

where  $\mathbf{M}(\tau)$  is the so-called monodromy matrix (state transition matrix evaluated after a period  $T$ ),  $\mathbf{P}(\tau)$  is a  $T$ -periodic matrix function and  $\mathbf{C}$  is a constant matrix, often referred to as the Floquet exponent matrix.

The stability of the system in consideration can be determined either by analyzing the eigenvalues of the monodromy matrix  $\mathbf{M}$  or the Floquet exponent matrix  $\mathbf{C}$ . In principal the Floquet method can also be applied analytically, but in the course of this thesis it is only applied numerically. The monodromy matrix can be numerically calculated by repeated integration of the system equations over one period  $T$ . The thereby used set of initial conditions has to be independent of each other. According to [5] it is beneficial to use the columns of the identity matrix  $\mathbf{I}$  as initial vectors for the integration. The first step of the numerical procedure is to solve  $n$  initial value problems over on period  $T$

$$\mathbf{y}' = \mathbf{A}(\tau)\mathbf{y}, \quad \mathbf{I} = [\mathbf{y}(0)_1, \mathbf{y}(0)_2, \dots, \mathbf{y}(0)_n], \quad \tau = [0, T], \quad (3.5.4)$$

and gather the monodromy matrix  $\mathbf{M}$  by arranging the results as follows

$$\mathbf{M}(T) = [\mathbf{y}(T)_1, \mathbf{y}(T)_2, \dots, \mathbf{y}(T)_n]. \quad (3.5.5)$$

To determine the stability of the system, the eigenvalues of the monodromy matrix are calculated using a common numerical method

$$\Lambda = \text{eig}[\mathbf{M}(T)]. \quad (3.5.6)$$

If one of the calculated eigenvalues is in its magnitude greater than one, the system is unstable. If on the other hand all eigenvalues are less than one, the system is stable

$$\max(|\Lambda_1|, |\Lambda_2|, \dots, |\Lambda_n|) \begin{cases} < 1 & \text{stable} \\ > 1 & \text{unstable.} \end{cases} \quad (3.5.7)$$

As already mentioned in the beginning of this section, the computational time will be reduced compared to an ordinary numerical simulation. The stability of a mechanical system

### 3.5. Floquet method

with  $n$  degrees of freedom can be determined by only  $2n$  numerical integrations and the eigenvalue calculation of a  $(2n \times 2n)$  matrix. This beneficial characteristic is used when carrying out the numerical parameter study described in Chapter 6.



# Parametric excitation in microelectromechanical systems

The use of parametric excitation in microelectromechanical systems has been largely investigated over the last few years. This chapter tries to give an insight into that topic by presenting three recently investigated MEMS applications in more detail. Emphasis is put on the basic function rather than technical details.

## 4.1 Systems with one degree of freedom

The single degree of freedom MEMS covered in this chapter are in principle of the same design as the oscillator previously shown in Fig. 2.5. Sometimes an additional pair of interdigitated comb drives is attached to both ends of the backbone, to allow an independent tuning of either the linear or the nonlinear electrostatic coefficient. The system is driven by applying a certain alternating voltage to the comb drives and hence the parametric excitation is provided by the resulting time dependent electrostatic stiffness.

As mentioned in the previous chapter it is a common characteristic to all parametrically excited systems, that they may exhibit parametric resonances at oscillation frequencies near  $2\omega_0/n$ , where  $n$  is an integer number greater or equal to one ( $n \geq 1$ ) and  $\omega_0$  is the purely elastic natural frequency defined as

$$\omega_0 = \sqrt{\frac{k_1}{m}}. \quad (4.1.1)$$

## 4.1. Systems with one degree of freedom

The coefficient  $k_1$  represents the linear mechanical stiffness of the system, whereas  $m$  represents its mass. A visualization of the first parametric region of instability ( $n = 1$ ) of a single degree of freedom MEMS is shown in Fig. 5.11. If the oscillator is operated outside the first instability wedge ( $\Omega = 2\omega_0$ ), it will be stable. If on the other hand the oscillator is operated inside the instability wedge, it will become unstable, indicated by a growth of the oscillation amplitude with time. Compared to an ordinary resonance phenomenon of a linear time-invariant system, which causes the oscillation amplitude to grow linearly with time, the parametric resonance causes the oscillation amplitude to grow exponentially with time. Many MEMS applications take advantage of this effect, to improve the system behavior with regard to its mechanical or electronic characteristics. In the following sections three very interesting MEMS applications will be explained in more detail.

### 4.1.1 Mass sensor

A common MEMS resonator for mass sensing consists of a simple microcantilever. In case of a single degree of freedom system, the resonator can be modeled by the following well known differential equation, where  $x$  represents the deflection,  $k$  the mechanical stiffness and  $m$  the mass of the cantilever

$$m\ddot{x} + kx = 0. \quad (4.1.2)$$

By dividing the differential equation by  $m$  and introducing the parameter  $\omega_0$ , Eq. (4.1.2) can be rewritten as follows

$$\ddot{x} + \omega_0^2 x = 0. \quad (4.1.3)$$

The solution of the differential equation is a harmonic oscillation with an angular frequency  $\omega_0$ . As can be seen in Eq. (4.1.1), the natural frequency is only dependent on the mechanical stiffness and the mass of the system. A common principle of mass sensing is to determine the shift of the natural frequency due to additionally attached mass. Therefore the mechanical stiffness has to be kept constant. The following equation exemplifies the frequency shift quite clearly

$$f = \frac{1}{2\pi} \sqrt{\frac{k}{m_{system} + m_{added}}}. \quad (4.1.4)$$

## 4.1. Systems with one degree of freedom

The detection of the shift in natural frequency can be carried out with several electronic measurement methods and according to [23] leads to detectable mass changes in the picogram (pg) region, or even femtogram (fg) when using nanoscale cantilevers.

The use of parametrically excited mass sensors has some advantages over the simple harmonic resonance (SHR) sensors and is therefore largely investigated by Turner and Zhang in [20–23]. The basic aim is to take advantage of the sharp transition between the stable and unstable state of motion of the oscillator, as shown in Fig. 5.11. The sharp transition allows the sensor to be more accurate, because even a small change in mass may lead to an unstable system. Operating the oscillator in that unstable mode causes the oscillation amplitude to grow exponentially, limited only by existing nonlinearities. Due to the large amplitude, the impact of occurring noise is reduced and eases further signal processing.

### 4.1.2 Electronic filter

Microelectromechanical system-based filters are a very interesting field of research, because they combine a number of advantages over more conventional designs. Most important, MEMS filters are very small, consume little power and are easy to integrate with electrical circuitry. Additionally, they are well tunable and able to perform parametrically excited oscillations. Such a parametrically excited filter design is discussed in [14], where the authors try to design a bandpass filter with almost ideal characteristics.

The design approach is to take advantage of the sharp transition between the stable and unstable state of motion of the oscillator. Whereas the parametric excitation has some desirable features concerning filter design, it also implicates certain problems. The center frequency and the bandwidth of the passband are dependent on the amplitude of the input signal. Furthermore, the relationship between that input and the output signal is nonlinear. Another problem is the existence of higher order resonances as can be seen in Eq. (3.1.4), where  $n$  can be any integer number greater or equal to one. The height of the first instability base point, located at the nondimensional frequency of  $\Omega = 2$  (see Fig. 5.11), is highly dependent on the system damping. This results in a minimal amplitude of the AC input signal, required for proper operation. Both problems can be solved by operating the oscillator near vacuum to reduce dissipative aerodynamic effects and amplifying the input signal.

To obtain a filter with steep edges, it is of vital importance to eliminate the dependence of the instability frequency on the amplitude of the AC input signal. In other words, the

#### 4.1. Systems with one degree of freedom

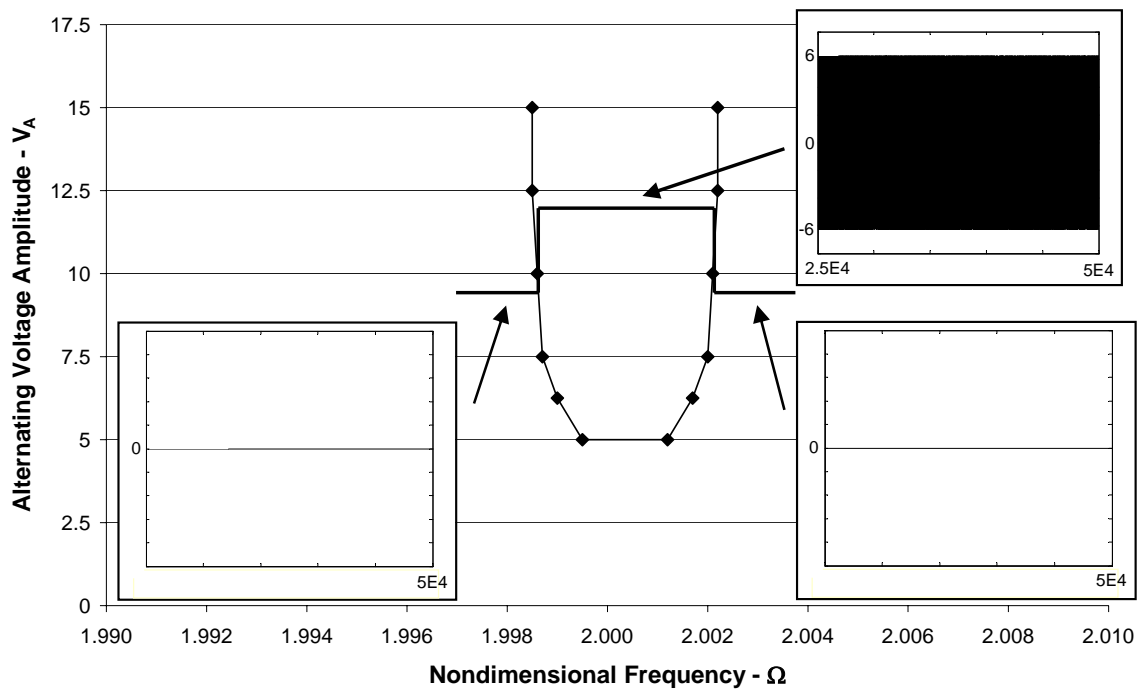


Figure 4.1: Simulation results of a parametrically excited MEMS bandpass filter [14].

boundaries of the instability wedge shown in Fig. 5.11 should be vertical lines. Rhoads and Shaw achieve that by attaching two sets of comb drives to the oscillator's backbone. One is driven by an AC signal, which is the one to be filtered, and the other one is driven by a DC signal. The oscillator is tuned in a way that the amplitude of the DC signal is dependent on the AC signal amplitude and the linear electrostatic stiffness coefficient is related to the linear excitation amplitude. By varying certain system parameters, one is able to rotate the instability wedge to a desired position.

The final bandpass filter design consists of two oscillators. One is a high pass switch with a tuned hardening nonlinearity and the other one is a low pass switch with a tuned softening nonlinearity. The passband is created by tuning the linear mechanical frequencies of both oscillators, such that their parametric resonance frequencies are slightly shifted. Figure 4.1 shows simulation results of the described bandpass filter.

It is quite obvious that the described filter concept shows almost ideal filter characteristics, although it is just a simulation and needs to be experimentally tested. However, the occurrence of higher order resonance frequencies, the design robustness, transient behavior and phase response require further investigations.

### 4.1.3 Parametric amplification

There are two different applications for parametrically excited microelectromechanical system-based amplifiers mentioned in the relevant literature. Rugar and Grütter describe a mechanical parametric amplifier in [15], whereas Raskin, Brown, Khuri-Yakub and Rebeiz investigate a more electronic based parametric MEMS amplifier in [12].

The mechanical parametric amplifier is used to increase the motional response of a microcantilever for small harmonic force excitations. A measurement system typically converts a physical phenomenon into an electronic signal via a sensor and then amplifies it for further processing. The mechanical parametric amplifier presented in [15] is used to preamplify the motion of the oscillator before transducing it. Such an amplifier is of particular interest, because in principle it can be noise-free and in practical applications may be used for signals where noise and backaction effects have a major impact. Additionally, the parametric amplifier can be used to produce mechanical squeezed states, which leads to thermomechanical noise squeezing.

The parametrically excited amplifier presented in [12] uses as MEMS time varying capacitor  $C(t)$ , which is composed of an array of low-stress metallized silicon-nitride diaphragms, to achieve parametric excitation. The capacitor is modeled as a suspended resonator and its behavior is described by the following differential equation

$$m\ddot{x} + c\dot{x} + kx = F_{es}(x, t), \quad (4.1.5)$$

where  $m$  is the mass of the movable structure,  $c$  the damping coefficient,  $k$  the mechanical stiffness coefficient and  $F_{es}$  the applied electrostatic external force.

The amplifier is provided with a 200 kHz input signal and the capacitor is pumped by a large signal voltage at 1.64 MHz. That leads to an output signal of 1.84 MHz, due to the power transfer from the pump frequency to the signal frequency. This results in an up-conversion ratio of 9:1. One advantage of such parametric amplifiers is that they are not based on neither semiconductors, nor resistors and therefore do not suffer from  $1/f$  noise. It is also possible to operate them at very high temperatures and under high particle bombardment. Due to these beneficial characteristics, microelectromechanical system-based amplifiers are very practical for the design of low noise circuits.

## **4.2 Systems with multiple degrees of freedom**

The papers concerning parametric excitation in microelectromechanical systems are limited to single degree of freedom systems only. Due to that fact this thesis is focusing on investigations concerning a parametrically excited MEMS oscillator with two degrees of freedom. Thereby, the main expectation is to detect the parametric anti-resonances effect and point out its potential beneficial characteristics. A detailed investigation of a MEMS oscillator with two degrees of freedom is presented in Chapter 6.

# Investigation of a single degree of freedom parametrically excited MEMS

This chapter is dealing with a single degree of freedom parametrically excited microelectromechanical system, comparable to the one previously shown in Fig. 2.5. The first step is to gain a suitable mechanical model and derive the equation of motion. Then the various system parameters are defined, followed by a detailed stability investigation using both an analytical and a numerical method. The influence of the mechanical and electrostatic nonlinearities is thereby also considered.

## 5.1 Modeling

To obtain a mechanical model for the microelectromechanical system, the device components need to be identified. Figure 5.1 shows the basic design of the MEMS oscillator under investigation. Such a system design is well established in the relevant literature e.g. [1, 13, 21, 22] and as already mentioned in Chapter 4, may be used for sensors or electronic filters.

The main component of the design is the backbone. It is connected to elastic beam structures on each side, which allow a movement to both the left and right hand side of the oscillator. To force the system into motion a pair of non-interdigitated comb drives is connected to the backbone. By applying an alternating voltage at a certain frequency to the

## 5.1. Modeling

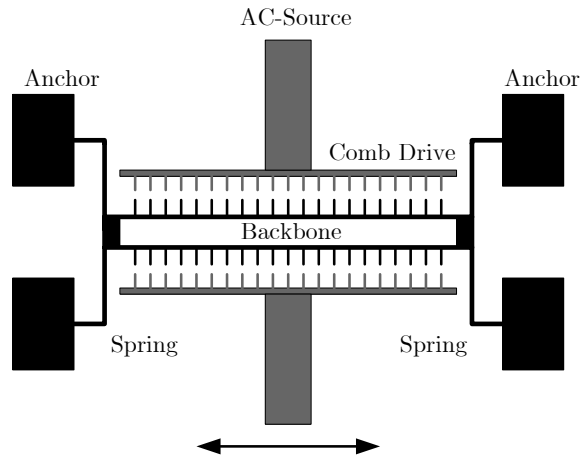


Figure 5.1: Basic design of a single degree of freedom MEMS oscillator.

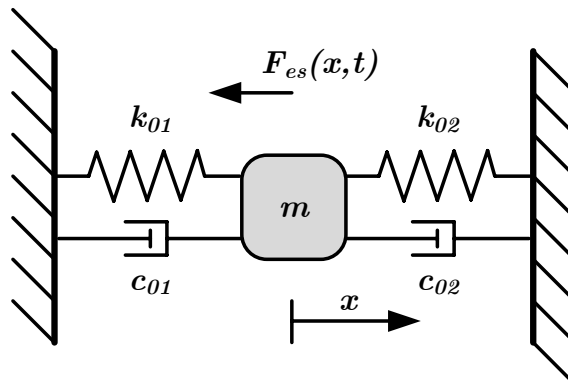


Figure 5.2: Mechanical model of a single degree of freedom MEMS oscillator.

comb drives, the system begins to oscillate at that frequency due to the arising electrostatic forces between the fixed and the free comb.

Looking at the given MEMS oscillator from a mechanical point of view, one may obtain the mechanical model shown in Fig. 5.2. The elastic beam structures are represented by two mechanical springs, connected to either side of the system mass. This system mass  $m$  consists of the oscillating components and therefore it is basically the mass of the oscillators backbone with its comb fingers connected to it. The damping of the system is modeled by two damping elements  $c_{01}$  and  $c_{02}$  that are connected in parallel to the spring elements.

The coordinate  $x$  is introduced to represent the oscillators deflection in horizontal direction (considering Fig. 5.2). Using Newton's laws of motion, the displacement of the MEMS can be described by the following differential equation

$$m\ddot{x} + (c_{01} + c_{02})\dot{x} + F_r(x) + F_{es}(x, t) = 0, \quad (5.1.1)$$

where  $\dot{x}$  and  $\ddot{x}$  are the first and second time derivatives of the displacement  $x$ . The function  $F_r(x)$  represents the elastic mechanical restoring force provided by the two springs  $k_{01}$  and  $k_{02}$ . According to [13], this force can be expressed by a cubic function of displacement. When later dealing with the system parameters of the MEMS, finite element analyses prove, that the mechanical restoring force is indeed a cubic function of displacement, as indicated by the following equation

$$F_r(x) = k_{01}^{lin} x + k_{01}^{nlin} x^3 + k_{02}^{lin} x + k_{02}^{nlin} x^3. \quad (5.1.2)$$

The terms  $k_{01}^{lin}$  and  $k_{02}^{lin}$  represent the effective linear spring coefficients of the left ( $k_{01}$ ) and right ( $k_{02}$ ) spring, and the terms  $k_{01}^{nlin}$  and  $k_{02}^{nlin}$  represent the effective nonlinear spring coefficients of the respective spring. The electrostatic restoring force arising from the comb drives can, according to [13], be modeled by a cubic function of displacement

$$F_{es}(x, t) = (r_{1A}x + r_{3A}x^3)V^2(t). \quad (5.1.3)$$

Due to the alternating voltage applied to the comb drives, the arising electrostatic restoring force is dependent on the time. This time dependency leads to a parametric excitation within the system. The electrostatic coefficients  $r_{1A}$  and  $r_{3A}$  are strongly affected by the design of the comb drives, which will be discussed in Chapter 5.1.2. The function  $V(t)$  represents the AC input signal of the comb drives. In order to achieve a zero phase difference between the linear and nonlinear parametric excitation (as shown later in Eq. 5.1.11), the input signal is defined as follows, see [13]

$$V(t) = V_A \sqrt{1 + \cos(\omega t)}. \quad (5.1.4)$$

Substituting Eqs. (5.1.2), (5.1.3) and (5.1.4) back into differential equation (5.1.1), one obtains the following differential equation for the displacement of the microelectromechanical system

$$m\ddot{x} + (c_{01} + c_{02})\dot{x} + x(k_{01}^{lin} + k_{02}^{lin}) + x^3(k_{01}^{nlin} + k_{02}^{nlin}) + (r_{1A}x + r_{3A}x^3)V_A^2 [1 + \cos(\omega t)] = 0. \quad (5.1.5)$$

## 5.1. Modeling

### 5.1.1 Rescaling displacement and time

For a better interpretation of the upcoming simulation results and efficient numerical treatment it is beneficial to make the differential equation of interest dimensionless. Therefore, a nondimensional parametric excitation frequency  $\Omega$  is introduced. This newly introduced frequency is related to the actual parametric excitation frequency as follows

$$\Omega = \frac{\omega}{\hat{\omega}}, \quad (5.1.6)$$

where  $\hat{\omega}$  is a characteristic reference frequency. It is common to either choose the systems natural frequency or the natural frequency of a subsystem as reference frequency. In the present case, given a system with just a single degree of freedom, it is beneficial to use the systems natural frequency as reference. The natural frequency of the undamped linear time-invariant system is known to be

$$\hat{\omega} = \sqrt{\frac{k_{01}^{lin} + k_{02}^{lin}}{m}}. \quad (5.1.7)$$

In order to obtain a scaled system time  $t$ , a dimensionless time  $\tau$  is introduced as follows

$$\tau = \hat{\omega}t. \quad (5.1.8)$$

That leads to a nondimensional argument of the cosine function

$$\omega t = \Omega \hat{\omega}t = \Omega \tau. \quad (5.1.9)$$

The systems displacement  $x$  is rescaled according to

$$z = \frac{x}{x_0}, \quad (5.1.10)$$

where  $x_0$  is a scaling parameter of the size of the systems physical dimensions. Carrying out the substitutions in Eq. (5.1.5), leads to a nondimensional differential equation of the form

$$z'' + 2z'(\xi_1 + \xi_2) + z[1 + \lambda_1 + \lambda_1 \cos(\Omega\tau)] + z^3[\chi + \lambda_3 + \lambda_3 \cos(\Omega\tau)] = 0, \quad (5.1.11)$$

where the newly introduced differential operators  $z'$ ,  $z''$  and the linear and nonlinear nondimensional parameters are defined as stated in Table 5.1. It can be seen that the effective

Definition	Nondimensional parameter
$z' = \frac{dz}{d\tau}$	Scaled time derivative
$\Omega = \frac{\omega}{\dot{\omega}}$	Nondimensional excitation frequency
$\xi_1 = \frac{c_{01}}{2m\dot{\omega}}$	Scaled damping ratio for $c_{01}$
$\xi_2 = \frac{c_{02}}{2m\dot{\omega}}$	Scaled damping ratio for $c_{02}$
$\lambda_1 = \frac{r_{1A} V_A^2}{k_{01}^{lin} + k_{02}^{lin}}$	Linear electrostatic excitation amplitude
$\lambda_3 = \frac{x_0^2 r_{3A} V_A^2}{k_{01}^{lin} + k_{02}^{lin}}$	Nonlinear electrostatic excitation coefficient
$\chi = \frac{(k_{01}^{nlin} + k_{02}^{nlin}) x_0^2}{k_{01}^{lin} + k_{02}^{lin}}$	Nonlinear mechanical stiffness coefficient

Table 5.1: Nondimensional parameter definitions corresponding to Eq. (5.1.11), adapted from [13].

linear and also nonlinear stiffness (mechanical and electrostatic stiffness combined) is dependent on the amplitude  $V_A$  of the input signal. The practical influence of  $V_A$  on the systems behavior is investigated in Chapter 5.2.1.

To prepare the nondimensional differential equation for the upcoming numerical simulations, one has to make the equation explicit in the highest derivative and reduce the order by introducing an additional equation

$$z' = u, \quad (5.1.12)$$

$$u' = -\left\{2z'(\xi_1 + \xi_2) + z[1 + \lambda_1 + \lambda_1 \cos(\Omega\tau)] + z^3[\chi + \lambda_3 + \lambda_3 \cos(\Omega\tau)]\right\}. \quad (5.1.13)$$

This step is necessary to work with the differential equation in any common simulation software package.

## 5.1.2 System parameters

The system parameters that need to be identified are the mechanical and electrostatic stiffness coefficients, the mass of the backbone and the damping coefficients. In order to obtain these parameters, a basic layout of the MEMS oscillator is given in Fig. 5.3, with its corresponding dimensions stated in Table 5.2. The depth of the oscillator is chosen to be  $D_B = 12\mu\text{m}$ .

The elastic beam structures of the MEMS are designed to have a dept to width ratio of 1/6. This high aspect ratio is of vital importance to validate the modeling assumptions

## 5.1. Modeling

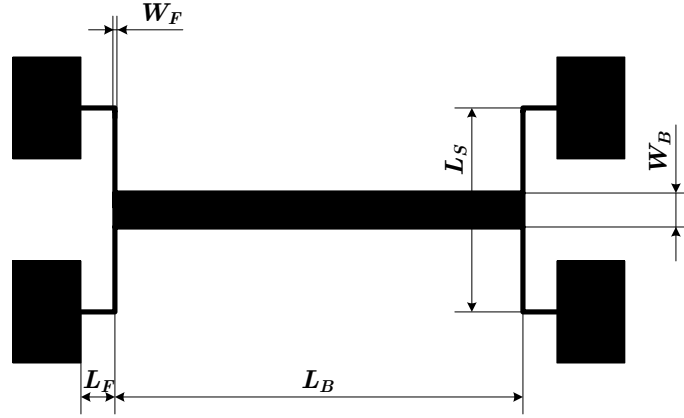


Figure 5.3: Basic layout of a single degree of freedom MEMS oscillator.

Parameter	Value	Dimension unit
$D_B$	12	$\mu\text{m}$
$L_F$	20	$\mu\text{m}$
$L_B$	400	$\mu\text{m}$
$L_S$	420	$\mu\text{m}$
$W_F$	2	$\mu\text{m}$
$W_B$	20	$\mu\text{m}$

Table 5.2: Dimensions of the single degree of freedom MEMS oscillator.

made to derive the differential equation of the oscillator. Due to the high aspect ratio the out of plane stiffness is greater than the in-plane stiffness and therefore it is reasonable to neglect the out of plane motion compared to the in-plane motion.

The length of the beams is selected on the basis of similarly designed MEMS described in [21] and [3]. The backbone is sufficiently long to enable the attachment of several comb fingers. To determine the linear and nonlinear mechanical stiffness coefficients, a nonlinear finite element analyses has been conducted. Two possible design approaches are thereby compared to each other. Figure 5.4 shows the two possible configurations (fixed-fixed and folded) used for the analyses. In both cases the respective endings of the beams are assumed to be fixed in its displacement and rotation.

The material for the MEMS oscillator is defined to be polysilicon, because of its isotropic characteristics and wide spread usage in surface micromachining techniques. Using single crystalline silicon on the other hand would result in a more complex constitutive law given its orthotropic stiffness matrix previously shown in Eq. (2.3.1). The material parameters

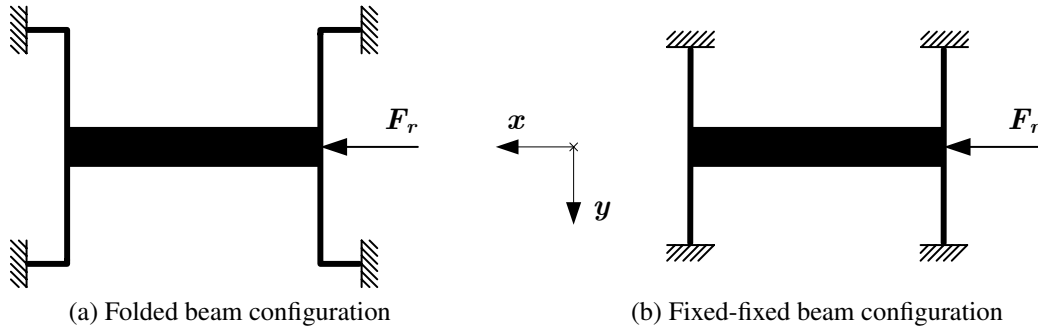


Figure 5.4: Mechanical models used for nonlinear finite element analyses.

used for polysilicon are taken from [16] and are listed below

$$E = 160 \text{ GPa}, \quad \nu = 0.22, \quad G = 65 \text{ GPa}, \quad (5.1.14)$$

where  $E$  is the Young's modulus,  $\nu$  the Poisson ratio and  $G$  the shear modulus.

In order to obtain proper stiffness coefficients, the mechanical restoring force  $F_r$  is incrementally increased during 20 calculation steps and the displacement  $x$  is meanwhile tracked in the middle of the backbone relative to the point of origin. Alternatively, the analysis can be performed by incrementally increasing the displacement and tracking the arising restoring force.

Figure 5.5 shows the calculated force displacement curve using ABAQUS. The crosses represent the folded beam configuration, whereas the circles represent the fixed-fixed configuration. Due to the symmetry of the given problem, only the displacements in positive  $x$ -direction are calculated (first quadrant of Fig. 5.5). The displacements in negative  $x$ -direction (third quadrant of Fig. 5.5) are inserted manually.

As Eq. (5.1.2) suggests, the load displacement curve can be best fitted by a cubic function of displacement (solid lines in Fig. 5.5). A polynomial fitting for the folded beam configuration results in the following equation

$$F_r^{folded}(x) = 7.01x + 0.036x^3, \quad (5.1.15)$$

whereas a polynomial fitting for the fixed-fixed beam load displacement curve results in

$$F_r^{fixed}(x) = 7.34x + 1.298x^3. \quad (5.1.16)$$

## 5.1. Modeling

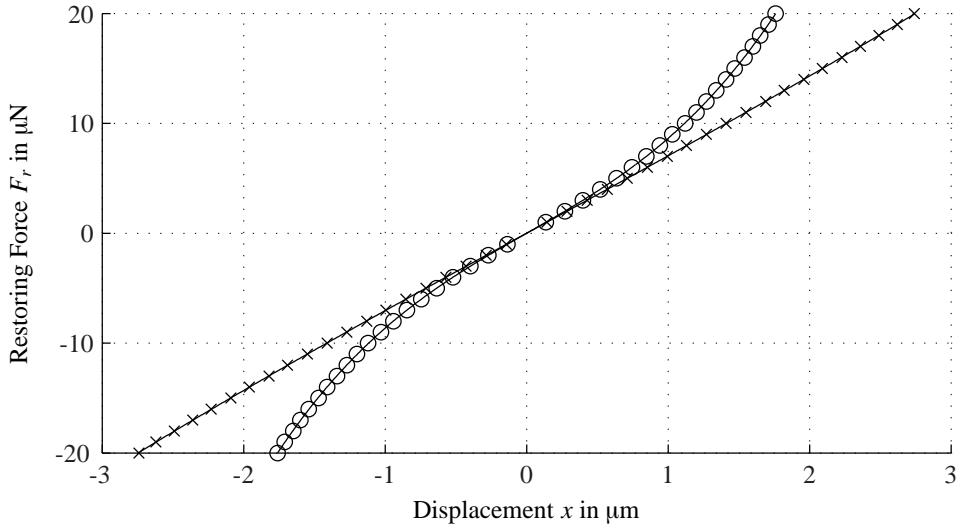


Figure 5.5: Calculated force displacement curve using ABAQUS.

Folded beam			Fixed-fixed beam		
Parameter	Value	Dimension unit	Parameter	Value	Dimension unit
$k_{01}^{lin}$	3.505	$\mu\text{N}/\mu\text{m}$	$k_{01}^{lin}$	3.670	$\mu\text{N}/\mu\text{m}$
$k_{01}^{nlin}$	0.018	$\mu\text{N}/\mu\text{m}^3$	$k_{01}^{nlin}$	0.649	$\mu\text{N}/\mu\text{m}^3$
$k_{02}^{lin}$	3.505	$\mu\text{N}/\mu\text{m}$	$k_{02}^{lin}$	3.670	$\mu\text{N}/\mu\text{m}$
$k_{02}^{nlin}$	0.018	$\mu\text{N}/\mu\text{m}^3$	$k_{02}^{nlin}$	0.649	$\mu\text{N}/\mu\text{m}^3$

Table 5.3: Comparison of the stiffness coefficients for fixed-fixed and folded beam configuration.

Due to the symmetry of the MEMS design and the equal length of the two elastic beams, the springs  $k_{01}$  and  $k_{02}$  feature the same mechanical characteristics. That means extracting the separate stiffness coefficients for each spring is done by simply splitting the fitted stiffness coefficients in Eq. (5.1.15) and (5.1.16) equally to either  $k_{01}$  or  $k_{02}$ . Through this approach one obtains the mechanical stiffness coefficients stated in Table 5.3.

As nonlinearities feature unwanted and more complex characteristics compared to a purely linear system, it is desired to keep them at a minimum. Thus, for the present oscillator design the folded beam configuration is preferred to the fixed-fixed configuration.

Additionally to the purely mechanical stiffness, the presence of electrostatic stiffness, provided by the two comb drives, needs to be considered. A comb drive basically consists of two combs that are arranged with entangled fingers. One comb structure is fixed in

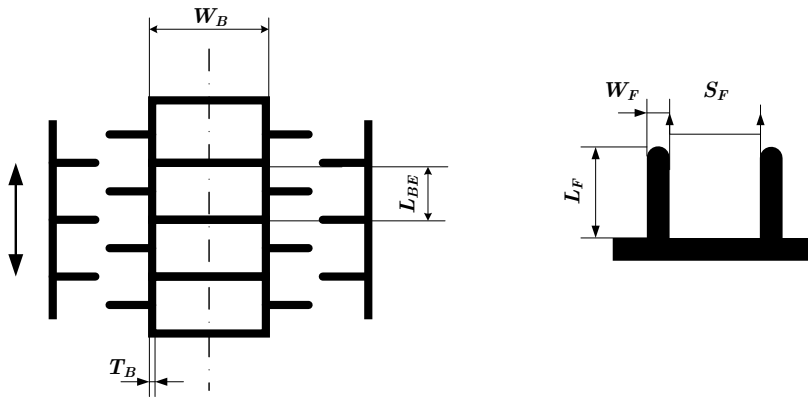


Figure 5.6: Detailed layout of the backbone with attached comb drive.

its displacement and the other comb is free in its motion. Applying a potential difference between the two sets of combs results in electrostatic forces. These arising forces lead to certain deflections of the free comb structure, depending on the design of the device. The deflection of the free comb structure is proportional to the electrostatic force and can hence be modeled by an electrostatic stiffness. Regarding the comb drive design, two common design options are mentioned in [21]. The first possibility is to arrange the comb fingers in an interdigitated way and the second one is to arrange them in a non-interdigitated way. Interdigitated comb fingers result in a motion parallel to the fingers, whereas a non-interdigitated design leads to a motion in perpendicular direction of the comb fingers. As can be seen in Fig. 5.1, the MEMS under consideration is driven by a pair of non-interdigitated comb drives, allowing the backbone to move in horizontal direction, as indicated by the arrow beneath the figure.

As mentioned before, the electrostatic stiffness, provided by the comb drives, is dependent on their design. In [10], the authors analyze the influence of certain comb finger shapes on the resulting stiffness. The present MEMS has a very basic non-interdigitated comb drive design like shown in Fig. 5.6. The initial position of the comb fingers is misaligned. Such a configuration is referred to as a *reduction actuator*. On the other hand, an aligned finger configuration is called *augmentation actuator*.

As evidenced by Fig. 5.6, the comb fingers consist of simple rectangles with its respective free edge rounded off. The backbone is perforated by small rectangles with a width of  $L_{BE}$ . A summary of the comb drive dimensions is stated in Table 5.4. The gap between the fingers of the fixed comb and the free comb is defined as  $1 \mu\text{m}$  and the depth of both the

## 5.1. Modeling

Backbone			Comb drive		
Parameter	Value	Dimension unit	Parameter	Value	Dimension unit
$W_B$	20	$\mu\text{m}$	$W_F$	2	$\mu\text{m}$
$L_{BE}$	10	$\mu\text{m}$	$L_F$	8	$\mu\text{m}$
$T_B$	2	$\mu\text{m}$	$S_F$	10	$\mu\text{m}$
$D_B$	12	$\mu\text{m}$	$D_F$	12	$\mu\text{m}$

Table 5.4: Dimensions of the backbone and the non-interdigitated comb drive.

HASP			COULOMB		
Parameter	Value	Dimension unit	Parameter	Value	Dimension unit
$r_{1A}$	$3.9 \times 10^{-4}$	$\mu\text{N}/\text{V}^2\mu\text{m}$	$r_{1A}$	$3.65 \times 10^{-4}$	$\mu\text{N}/\text{V}^2\mu\text{m}$
$r_{3A}$	$-1.4 \times 10^{-5}$	$\mu\text{N}/\text{V}^2\mu\text{m}^3$	$r_{3A}$	$-1.6E \times 10^{-5}$	$\mu\text{N}/\text{V}^2\mu\text{m}^3$

Table 5.5: Calculated linear electrostatic stiffness  $r_{1A}$  and cubic electrostatic stiffness  $r_{3A}$ .

backbone and the comb drive structure is  $D_B = D_F = 12\mu\text{m}$ .

The dimensions of the comb drive listed in Table 5.4 are taken from [1]. In that paper the authors determine the force versus deflection response of a non-interdigitated comb drive with 128 misaligned comb fingers. Due to arising electric fringing fields around the comb fingers, the comb drive is characterized numerically. Examining the dimensions of the comb fingers shows that the height is much greater than the gap, which makes it reasonable to consider the electric fields around the fingers as varying only in-plane. This assumption justifies the usage of a simplified two dimensional calculation model.

As well as the mechanical stiffness, the electrostatic stiffness may also be represented by a cubic function of the displacement  $x$  (see Eq. 5.1.3). Table 5.5 summarizes the results of two numerical calculations regarding the electrostatic stiffness of the afore described comb drive. Both calculations are based on the comb drive dimensions stated in the right hand side column of Table 5.4. The results obtained with the software package called HASP are taken from [1], whereas the results obtained with the COULOMB software package are taken from [21]. To allow further investigations, the electrostatic stiffness coefficients obtained with COULOMB are used for the present system.

The mass of the backbone is made up of the perforated main structure and the attached comb fingers. Given the density of polysilicon at a value of  $\rho = 2330\text{kg}/\text{m}^3$  one obtains

$$m = V\rho = 1.22 \times 10^{-10}\text{kg},$$

Parameter	Value	Physical unit
$m$	$1.22 \times 10^{-10}$	kg
$c_{01}$	$1.94 \times 10^{-8}$	Ns/m
$c_{02}$	$1.94 \times 10^{-8}$	Ns/m
$k_{01}^{lin}$	3.505	$\mu\text{N}/\mu\text{m}$
$k_{02}^{lin}$	3.505	$\mu\text{N}/\mu\text{m}$
$k_{01}^{nlin}$	0.018	$\mu\text{N}/\mu\text{m}^3$
$k_{02}^{nlin}$	0.018	$\mu\text{N}/\mu\text{m}^3$
$r_{1A}$	$3.65 \times 10^{-4}$	$\mu\text{N}/\text{V}^2\mu\text{m}$
$r_{3A}$	$-1.6 \times 10^{-5}$	$\mu\text{N}/\text{V}^2\mu\text{m}^3$

Table 5.6: Parameter values of the single degree of freedom MEMS oscillator.

as the effective mass of the oscillator.

As the damping of a mechanical system is difficult to assess in theory, the damping coefficients of the present system are taken from [13]. The system discussed therein is similar to the one shown in Fig. 5.1 and has been practically built to experimentally verify certain simulation results. For that reason the specified system damping is a good indication for the occurring damping in the present system. Table 5.6 summarizes all system parameters discussed in this chapter, with its corresponding physical units.

## 5.2 Stability investigation

The stability of the present parametrically excited single degree of freedom oscillator is investigated both analytically and numerically. The first approach is to apply a perturbation analysis to the nondimensional equation of motion and analyze the different characteristic forms of the nonlinearity by looking at the steady state responses. A numerical stability investigation is carried out subsequently, which uses the system parameters to solve the equation of motion in the time domain. Finally both methods of investigation are compared to each other with regard to the first parametric region of instability.

### 5.2.1 Analytical stability investigation

To analyze the impact of nonlinearities on the behavior of the present system, perturbation technique is used. This requires the introduction of a small perturbation parameter  $\epsilon$  to

## 5.2. Stability investigation

the nondimensional equation of motion (5.1.11). Carrying out this substitution leads to the following differential equation

$$z'' + \epsilon 2z'(\xi_1 + \xi_2) + z[1 + \epsilon\lambda_1 + \epsilon\lambda_1 \cos(\Omega\tau)] + \epsilon z^3 [\chi + \lambda_3 + \lambda_3 \cos(\Omega\tau)] = 0. \quad (5.2.1)$$

In analogy to the averaging method described in Chapter 3, the first step is to examine the solution of the differential equation with the parameter  $\epsilon$  set to zero. This leads to the following well known solution

$$z(\tau) = r(\tau) \cos\left(\frac{\Omega\tau}{2} + \psi(\tau)\right), \quad (5.2.2)$$

with its integration constants  $(r_0, \psi_0)$  already replaced by functions of the rescaled time  $\tau$ . Differentiation of Eq. (5.2.2) with respect to  $\tau$  leads to the following expression

$$z'(\tau) = -r(\tau) \sin\left(\frac{\Omega\tau}{2} + \psi(\tau)\right). \quad (5.2.3)$$

Using Eqs. (5.2.2) and (5.2.3) enables the transformation of differential equation (5.2.1) into amplitude and phase coordinates. To capture the dynamic effects near the first parametric resonance ( $\omega = 2\omega_0$ , where  $\omega_0$  is the natural frequency), it is beneficial to define a frequency detuning factor  $\sigma$  as follows [13]

$$\Omega = 2 + \epsilon\sigma. \quad (5.2.4)$$

The value 2 in Eq. (5.2.4) assumes that the first parametric resonance will occur at a nondimensional frequency of  $\Omega = 2$ . Since in the present case the nondimensional frequency  $\Omega$  has been related to the natural frequency of the whole system (see Eq. 5.1.6), this is a valid assumption. The frequency detuning factor  $\sigma$  is a measure for the distance between the actual nondimensional frequency  $\Omega$  and the nondimensional parametric resonance condition for the first parametric resonance. For better legibility, the angular argument is substituted as follows

$$\Phi = \frac{\Omega\tau}{2} + \psi. \quad (5.2.5)$$

By differentiating  $z(\tau)$  one obtains  $z'(\tau)$ , which can be compared with Eq. (5.2.3) and yields the condition

## 5.2. Stability investigation

$$r' \cos(\Phi) - \psi' r \sin(\Phi) = 0. \quad (5.2.6)$$

Differentiation of  $z'(\tau)$  leads to  $z''(\tau)$  which can be substituted into Eq. (5.2.1) along with Eq. (5.2.2), leading to a second condition of the form

$$\begin{aligned} & -\frac{1}{2}\Omega r' \sin(\Phi) - \frac{1}{4}r\Omega^2 \cos(\Phi) - \frac{1}{2}\Omega r\psi' \cos(\Phi) - \epsilon\Omega r(\xi_1 + \xi_2) \sin(\Phi) \\ & + r \cos(\Phi) (1 + \epsilon\lambda_1 + \epsilon\lambda_1 \cos(\Omega\tau)) + \epsilon r^3 \cos^3(\Phi) (\chi + \lambda_3 + \lambda_3 \cos(\Omega\tau)) = 0. \end{aligned} \quad (5.2.7)$$

Solving the system of equations for the terms  $r'$  and  $\psi'$  leads to the following two equations

$$r' = \frac{-r\Omega}{2} \sin(\Phi) \cos(\Phi) - \epsilon(\xi_1 + \xi_2) \sin^2(\Phi) + \frac{2r}{\Omega} \cos^2(\Phi) \quad (5.2.8)$$

$$(1 + \epsilon\lambda_1 + \epsilon\lambda_1 \cos(\Phi)) + \frac{2\epsilon r^3}{\Omega} \cos^4(\Phi) \sin(\Phi) (\chi + \lambda_3 + \lambda_3 \cos(\Phi)),$$

$$\psi' = -\frac{\Omega}{2} \cos^2(\Phi) - \epsilon(\xi_1 + \xi_2) \cos(\Phi) \sin(\Phi) + \frac{2}{\Omega} \cos^2(\Phi) \quad (5.2.9)$$

$$(1 + \epsilon\lambda_1 + \epsilon\lambda_1 \cos(\Omega\tau)) + \frac{2\epsilon r^2}{\Omega} \cos^4(\Phi) (\lambda_3 + \lambda_3 \cos(\Omega\tau)).$$

These two equations can be averaged over the period  $4\pi/\Omega$ , to obtain the following equations [17]

$$r'_a = \frac{1}{8}\epsilon r_a \left[ -8(\xi_1 + \xi_2) + (2\lambda_1 + r_a^2 \lambda_3) \sin(2\psi_a) \right] + \mathcal{O}(\epsilon^2), \quad (5.2.10)$$

$$\psi'_a = \frac{1}{8}\epsilon \left[ 3r_a^2 (\chi + \lambda_3) + 4\lambda_1 - 4\sigma + 2(\lambda_1 + r_a^2 \lambda_3) \cos(2\psi_a) \right] + \mathcal{O}(\epsilon^2), \quad (5.2.11)$$

where  $\epsilon$  terms with orders greater than one are neglected. To analyze the stability of the system, the steady state responses are investigated. In order to obtain these responses, Eqs. (5.2.10) and (5.2.11) are set to zero. The damping coefficients  $\xi_1$  and  $\xi_2$  are neglected, because the characteristic form of the nonlinearity is not affected by damping. By solving the system of equations one obtains six solutions for the amplitude  $r$  and phase  $\psi$ , respectively. In each case one solution is of a trivial form and therefore not of interest. The first solution for amplitude and phase is given by

## 5.2. Stability investigation

$$r_{a1} = \pm \sqrt{2} \sqrt{\frac{\lambda_1}{\lambda_3}}, \quad (5.2.12)$$

$$\psi_{a1} = \frac{1}{2} \left( \pi - \cos^{-1} \left( \frac{\lambda_1 \lambda_3 + 3\lambda_1 \chi + 4\lambda_3 \sigma}{\lambda_1 \lambda_3} \right) \right). \quad (5.2.13)$$

Due to the absence of the frequency detuning parameter  $\sigma$  in the amplitude solution, Eq. (5.2.12) is of a constant amplitude. The remaining nontrivial solutions appear in pairs with its amplitude only varying in sign

$$r_{a2,3} = \pm \sqrt{\frac{4\sigma - 6\lambda_1}{5\lambda_3 + 3\chi}}, \quad (5.2.14)$$

$$\psi_{a2,3} = 0, \quad (5.2.15)$$

$$r_{a4,5} = \pm \sqrt{\frac{4\sigma - 2\lambda_1}{\lambda_3 + 3\chi}}, \quad (5.2.16)$$

$$\psi_{a4,5} = \frac{\pi}{2}. \quad (5.2.17)$$

Each pair of solutions ( $r_{a2,3}$  and  $r_{a4,5}$ ) represent the same physical response, where the denominator is defined by the nonlinear electrostatic excitation coefficient  $\lambda_3$  and the nonlinear mechanical stiffness coefficient  $\chi$ . If these two sets of solutions are analyzed in the nonlinear parameter space  $\chi$ - $\lambda_3$ , one can obtain the transitions of the nonlinear characteristics. Figure 5.7 illustrates the regions where different nonlinear characteristics occur.

For better understanding of the nonlinear characteristics, effective nonlinearities  $\alpha_1$  and  $\alpha_2$  are defined to be the denominators of Eqs. (5.2.14) and (5.2.16), respectively

$$\alpha_1 = 5\lambda_3 + 3\chi, \quad (5.2.18)$$

$$\alpha_2 = \lambda_3 + 3\chi. \quad (5.2.19)$$

Detailed analyses of the effective nonlinearities reveal that three different cases are of particular interest and will therefore be covered in more detail. Since the main interest is to analyze the characteristic forms of the nonlinearity, the influence of damping and higher order nonlinearities ( $\mathcal{O}(\epsilon^2)$ ) are neglected. A more detailed stability investigation concerning a similar parametrically excited system, including the effect of small damping, can be found in [13].

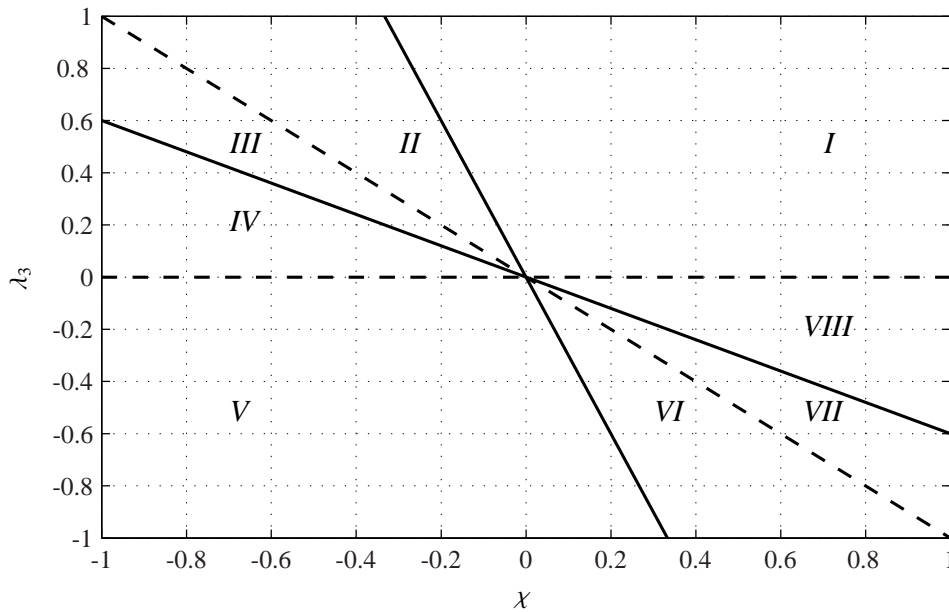


Figure 5.7: Nonlinear characteristics examined in the  $\chi$ - $\lambda_3$  parameter space.

- $\alpha_1 > 0$  and  $\alpha_2 > 0$ :

If both effective nonlinearities are greater than zero the system operates in Section *I* or *VIII* corresponding to Fig. 5.7. This means that the system has a hardening nonlinearity. Plotting the response amplitudes versus frequency detuning results in Figs. 5.8 a) and h), clearly indicating the hardening nonlinearity. The dashed lines indicate unstable response branches, whereas the solid lines indicate stable response branches. By looking at the frequency response corresponding to Section *VIII* (Fig. 5.9 d) it can be seen, that a  $\pi/2$  phase shift occurs between the detuning values of  $\sigma = 1.75$  and  $\sigma = 3.75$ . This shift indicates that the stability of the amplitude response switches between the two branches via the constant amplitude branch as shown in Fig. 5.8 h). Nevertheless the system has a quasi-hardening behavior.

- $\alpha_1 < 0$  and  $\alpha_2 < 0$ :

If on the other hand both effective nonlinearities are smaller than zero, the system operates in Section *IV* or *V* corresponding to Fig. 5.7. This means that the system has a softening nonlinearity. Plotting the response amplitudes versus frequency detuning results in Figs. 5.8 d) and e), clearly indicating the softening nonlinearity. The stability of the response branches in Section *V* again switches between the branches like in

## 5.2. Stability investigation

Section *VIII*. According to the appropriate frequency response plot shown in Fig. 5.9 a), the stability transition takes place between frequency detuning values of  $\sigma = -4$  and  $\sigma = -3$ . The stability switches via the constant amplitude branch, resulting in a quasi-softening nonlinear characteristic.

- $\alpha_1 > 0$  and  $\alpha_2 < 0$  or vice versa:

Additionally to the more common cases covered above, the present parametrically excited system provides mixed nonlinear characteristics as well, meaning that both amplitude response branches bend towards or away from each other. These mixed characteristics occur in Sections *II*, *III*, *VI* and *VII* according to Fig. 5.7 and can be illustrated by plotting the response amplitudes versus frequency detuning, resulting in Figs. 5.8 b), c), f) and g). Concerning Section *VI* and *VII* the stability switches between the two response branches via the constant amplitude branch. The reason for that is the  $\pi/2$  phase shift illustrated in the corresponding frequency response plots (Fig. 5.9 b) and c). The stability transitions occur between frequency detuning values of  $\sigma = -0.25$  and  $\sigma = 0.75$  concerning Section *VI* and  $\sigma = 0.87$  and  $\sigma = 1.88$  concerning Section *VII*, respectively.

To produce Figs. 5.8 and 5.9 different sets of values are taken for parameters  $\chi$  and  $\lambda_3$ , which are stated in the caption of each figure. The linear electrostatic excitation amplitude is set to  $\lambda_1 = 1$ , which leads to the following roots of the amplitude response branches shown in Fig. 5.8.

$$\sigma_1 = \frac{1}{2}\lambda_1 = \frac{1}{2}, \quad \sigma_2 = \frac{3}{2}\lambda_1 = \frac{3}{2} \quad (5.2.20)$$

### 5.2.2 Numerical stability investigation

The numerical approach is to solve the given equation of motion in the time domain and examine the resulting vibrations to analyze the stability of the present system. By using the system parameters stated in Table 5.6, setting the scaling parameter to  $x_0 = 1\mu\text{m}$  and assuming an initial displacement of  $x(t = 0) = 1\mu\text{m}$  and no initial velocity, results in two nondimensional initial conditions of the form

## 5.2. Stability investigation

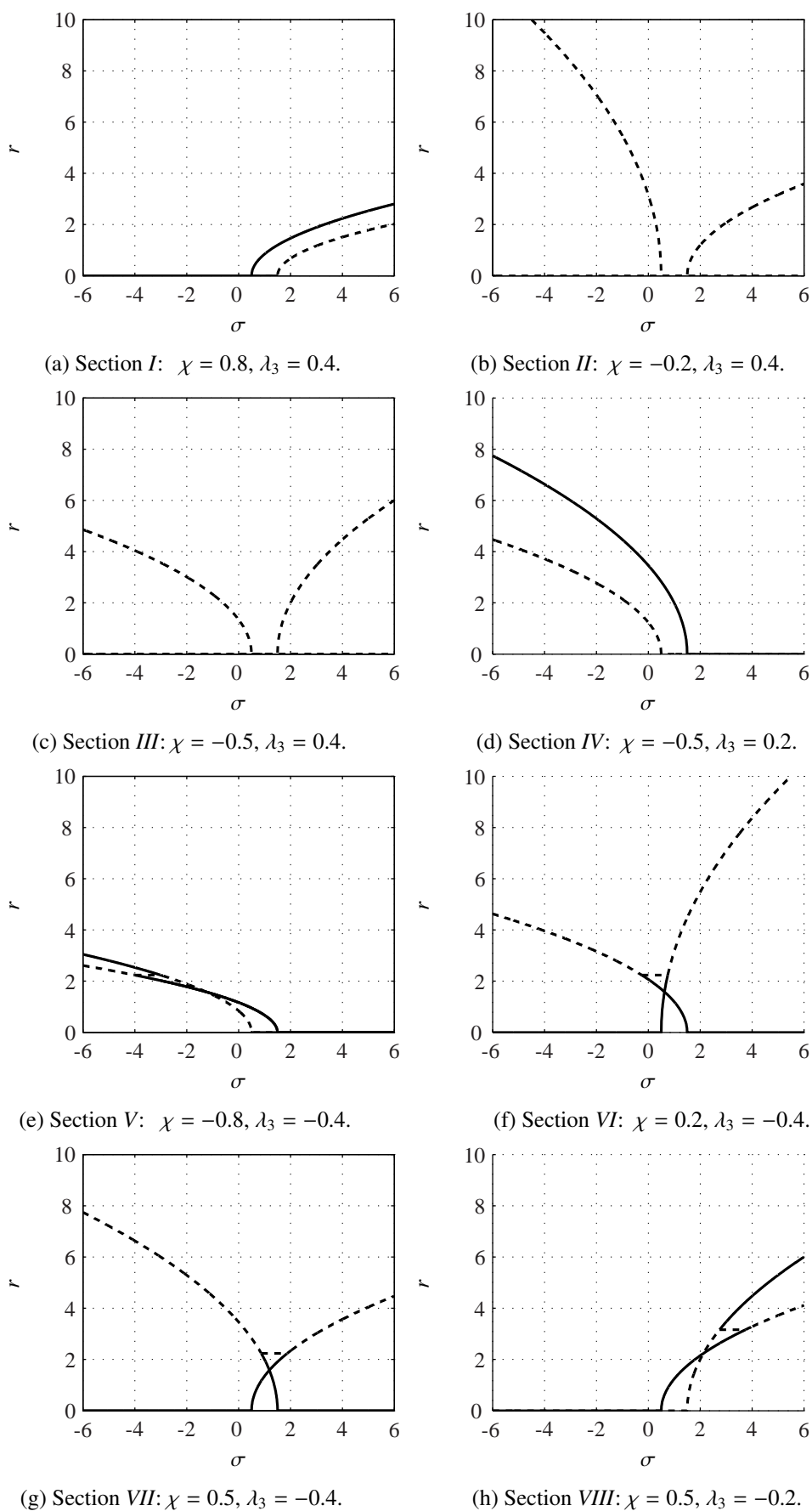


Figure 5.8: Amplitude responses for different sections corresponding to Fig. 5.7.

## 5.2. Stability investigation

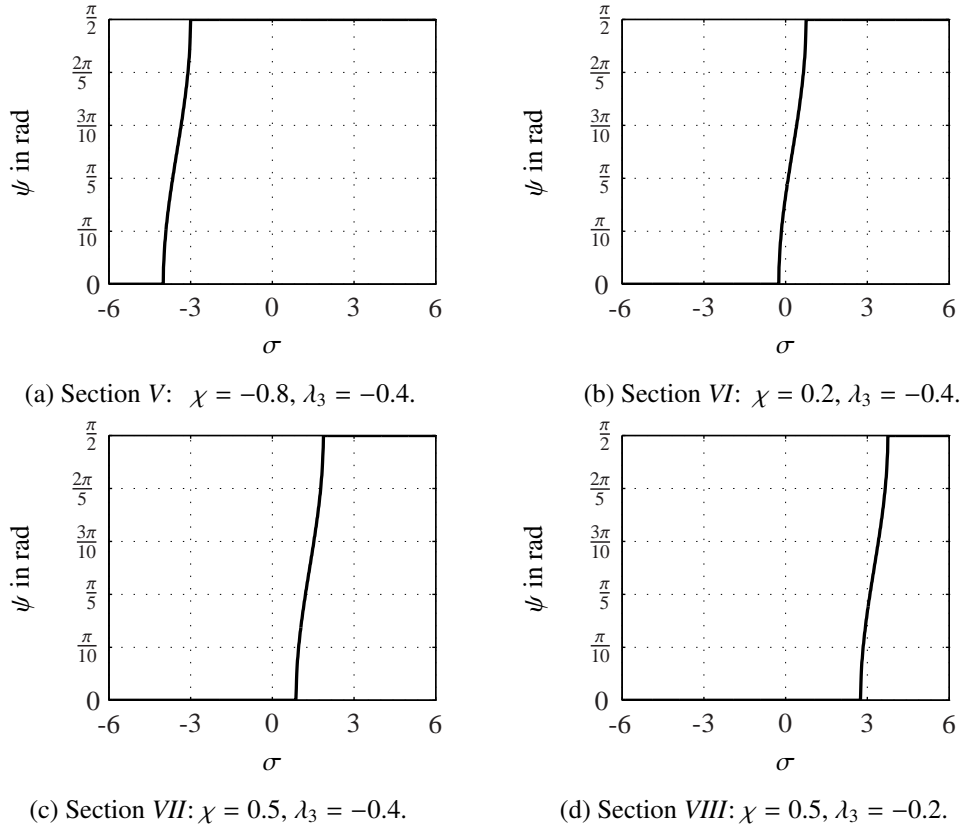


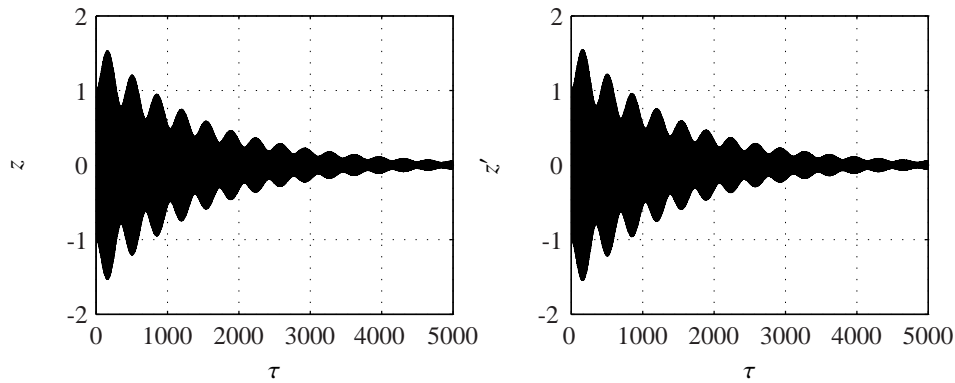
Figure 5.9: Frequency responses for different sections corresponding to Fig. 5.7.

$$z(\tau = 0) = \frac{x(t = 0)}{x_0} = 1, \quad (5.2.21)$$

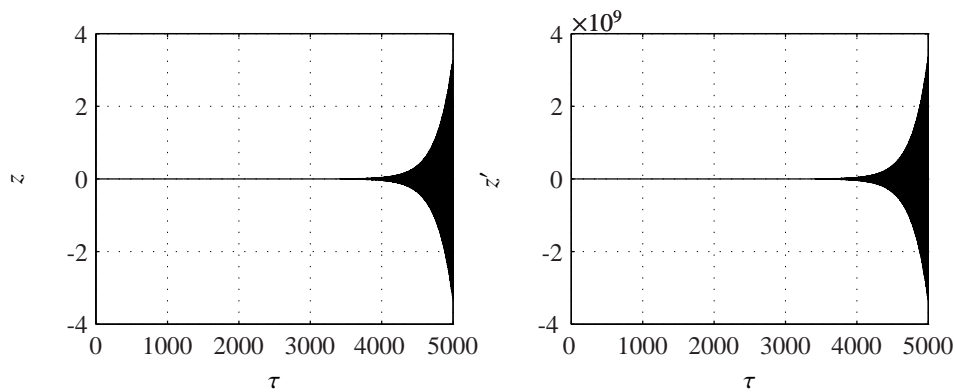
$$z'(\tau = 0) = 0, \quad (5.2.22)$$

which enable the numeric integration of differential equation (5.1.13). For easier interpretation of the results, the nonlinear terms of the equation of motion are neglected first. Choosing a parametric excitation frequency of  $\Omega = 2$ , which equals two times the natural frequency  $\omega_0$  of the system and an amplitude of the input signal of  $V_A = 20V$ , results in the vibration shown in Fig. 5.10 a). The plot clearly shows an exponential decrease of the oscillation amplitude and velocity amplitude with time. This indicates that the system is stable. If the resonance condition for parametrically excited systems is reviewed, it can be seen that at a frequency of  $\omega = 2\omega_0$  the system should exhibit a parametric resonance and therefore be unstable. This difference between theory and simulation is caused by the influence of the alternating voltage amplitude  $V_A$ . Since the linear and nonlinear electrostatic

## 5.2. Stability investigation



(a) Oscillation and velocity amplitude of the linearized system at  $\Omega = 2$  and  $V_A = 20V$ .



(b) Oscillation and velocity amplitude of the linearized system at  $\Omega = 2.02$  and  $V_A = 20V$ .

Figure 5.10: Displacement plots near the first parametric resonance with  $V_A = 20V$ .

parameters  $\lambda_1$  and  $\lambda_3$  in Eq. (5.1.13) are dependent on the amplitude  $V_A$  of the input signal, the systems stability behavior is as well depending on the concrete value of  $V_A$ .

If the parametric excitation frequency is slightly shifted to  $\Omega = 2.02$  and leaving all other parameters (including  $V_A$ ) unchanged, the resulting vibration looks different. As can be seen in Fig. 5.10 b), the oscillation and velocity amplitudes grow exponentially with time and therefore indicate that the system is unstable.

The dependence of the systems stability on the alternating voltage amplitude  $V_A$  is depicted in Fig. 5.11. The solid lines represent the analytically approximated stability boundaries using the averaged equations derived in Chapter 5.2.1, whereas the squares represent the calculated stability boundaries using numerical simulation. The stability chart shows a good match between the analytically and numerically calculated first parametric region of instability, especially for lower voltage amplitudes. As the effect of damping has been neglected when the perturbation technique was applied, the two results differ with present

## 5.2. Stability investigation

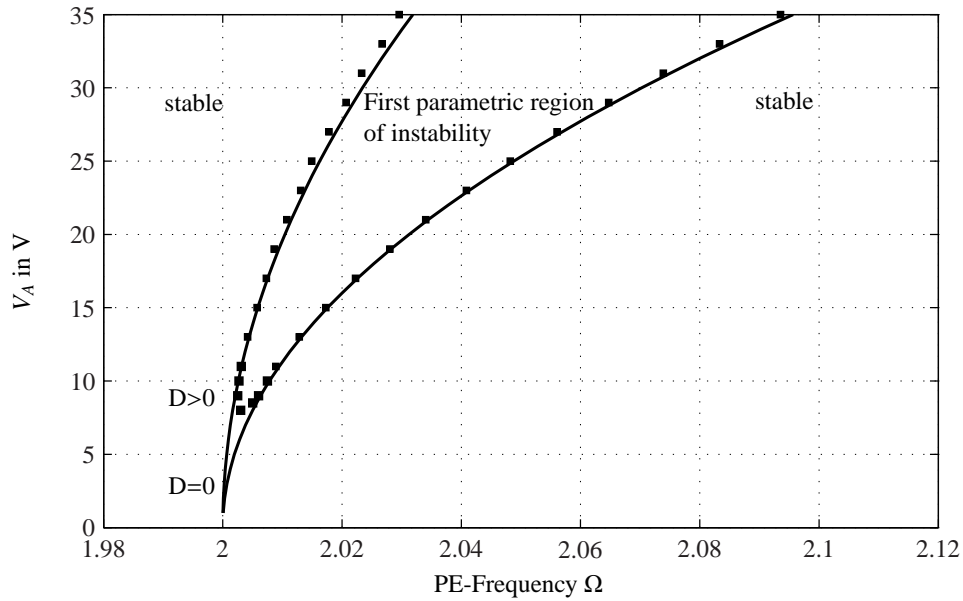


Figure 5.11: First parametric region of instability.

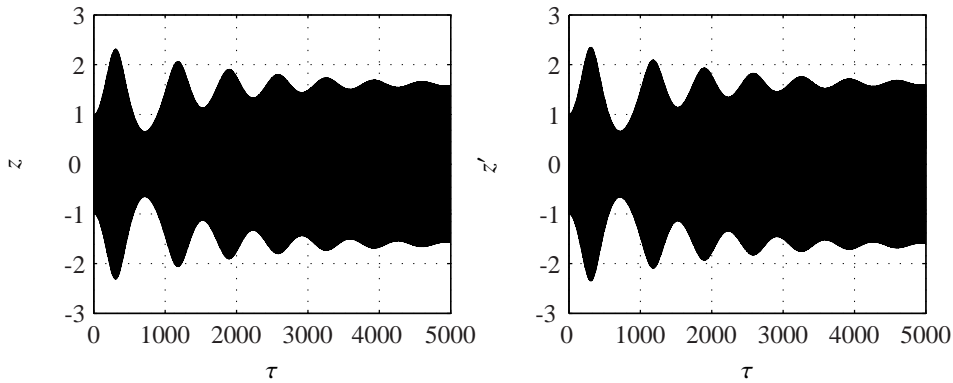


Figure 5.12: Oscillation and velocity amplitude of the nonlinear system at  $\Omega = 2.02$  and  $V_A = 20V$ .

damping ( $D > 0$ ). Due to the quadratic presence of  $V_A$  in the linear electrostatic excitation amplitude  $\lambda_1$ , the stability boundaries are curved and therefore the system is stable at the first parametric resonance frequency  $\Omega = 2$  (see Fig. 5.10 a), except for the theoretical case when  $V_A \ll 1$  and the damping is zero ( $D = \xi_1 + \xi_2 = 0$ ). Inside the stability boundaries the system is unstable proved by exponentially growing oscillation amplitudes.

To illustrate the effect of the nonlinearities in the time domain, Fig. 5.12 shows the resulting vibration with the same parameters used to produce Fig. 5.10 b). The system be-

## 5.2. Stability investigation

havior is still unstable due to the growing amplitudes, but in comparison to the purely linear system, the oscillation and velocity amplitudes are limited by the nonlinearities. Since the spacing of the comb fingers is limited to  $10\mu\text{m}$ , this well expected phenomenon indicates the proper operation of the oscillator, even when operated at a parametric resonance.



# Investigation of a two degree of freedom parametrically excited MEMS

On the basis of investigations concerning a single degree of freedom microelectromechanical system oscillator, this chapter deals with a parametrically excited MEMS oscillator with two degrees of freedom. First a mechanical model is developed and suitable differential equations are derived. Based on that differential equations, the aim is to analyze the parametric resonances, especially the parametric anti-resonance phenomenon already mentioned in Chapter 3. To identify the various resonant regions, the monodromy matrix of the system is numerically calculated, whereupon its eigenvalues are used to determine the stability of the system. Afterwards, a parameter study is carried out to individually optimize the linear system parameters, in order to obtain a maximized occurrence of the anti-resonance effect.

## 6.1 Modeling

The desired oscillator design with two degrees of freedom is achieved by combining two oscillators with a system design similar to the one shown in Fig. 5.1. Instead of the two fixed anchors on the right hand side, another set of springs connected to a backbone is attached to the original design. An additional set of non-interdigitated comb drives is connected to the newly introduced backbone. The expansion of the single degree of freedom system design may result in an oscillator with a basic layout shown in Fig. 6.1.

## 6.1. Modeling

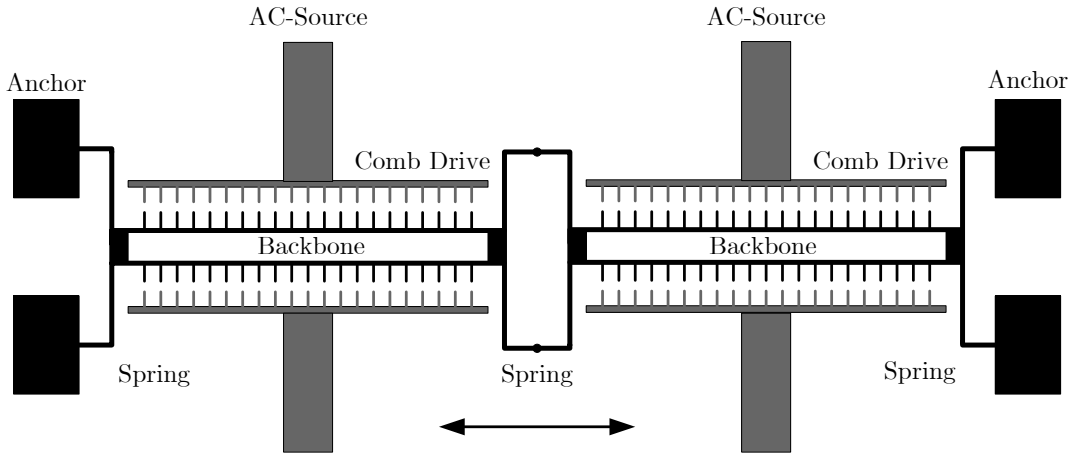


Figure 6.1: Basic design of a two degree of freedom MEMS oscillator.

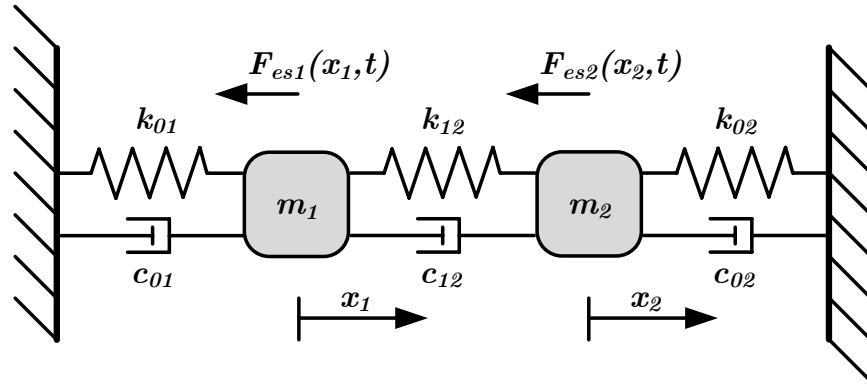


Figure 6.2: Mechanical model of a two degree of freedom MEMS oscillator.

As in the previous chapter, the elastic beams are mechanically modeled by springs named  $k_{01}$ ,  $k_{12}$  and  $k_{02}$ . The two backbone structures of the system are represented by the masses  $m_1$  and  $m_2$ . The two sets of non-interdigitated comb drives result in electrostatic restoring forces named  $F_{es1}$  and  $F_{es2}$ , acting on the particular system mass. The existing system damping is represented by three mechanical dampers named  $c_{01}$ ,  $c_{12}$  and  $c_{02}$ . These model assumptions result in the mechanical model shown in Fig. 6.2.

Introducing the coordinates  $x_1$  and  $x_2$ , representing the oscillators deflection in horizontal direction, results in an oscillating mechanical system with two degrees of freedom that can be described by the following equation of motion in matrix form

$$\mathbf{M}\ddot{\mathbf{x}} + \mathbf{C}\dot{\mathbf{x}} + \mathbf{F}_r(\mathbf{x}) + \mathbf{F}_{es}(\mathbf{x}, t) = 0, \quad (6.1.1)$$

where the electrostatic restoring forces are represented by the matrix  $\mathbf{F}_{es}$  and the mechanical restoring forces, provided by the springs, are represented by the matrix  $\mathbf{F}_r$ . The mass matrix is denoted  $\mathbf{M}$ , the damping matrix  $\mathbf{C}$  and the vector of deflections  $\mathbf{x}$

$$\mathbf{M} = \begin{bmatrix} m_1 & 0 \\ 0 & m_2 \end{bmatrix}, \quad \mathbf{C} = \begin{bmatrix} c_{01} + c_{12} & -c_{12} \\ -c_{12} & c_{02} + c_{12} \end{bmatrix}, \quad \mathbf{x} = \begin{bmatrix} x_1 \\ x_2 \end{bmatrix}. \quad (6.1.2)$$

It is assumed that the mechanical and electrostatic stiffness show the same nonlinear characteristics as in the single degree of freedom case. Therefore, the stiffness matrices are split into linear and nonlinear parts. This results in slightly different equations of motion

$$\mathbf{M}\ddot{\mathbf{x}} + \mathbf{C}\dot{\mathbf{x}} + \mathbf{F}_r^{lin}(\mathbf{x}) + \mathbf{F}_r^{nlin}(\mathbf{x}^3) + \mathbf{F}_{es}^{lin}(\mathbf{x}, t) + \mathbf{F}_{es}^{nlin}(\mathbf{x}^3, t) = 0. \quad (6.1.3)$$

Fitting the nonlinear mechanical restoring forces by cubic functions of displacement, results in the following stiffness matrix  $\mathbf{F}_r$

$$\mathbf{F}_r(\mathbf{x}) = \mathbf{F}_r^{lin}(\mathbf{x}) + \mathbf{F}_r^{nlin}(\mathbf{x}^3), \quad (6.1.4)$$

$$\mathbf{F}_r(\mathbf{x}) = \begin{bmatrix} k_{01}^{lin} + k_{12}^{lin} & -k_{12}^{lin} \\ -k_{12}^{lin} & k_{02}^{lin} + k_{12}^{lin} \end{bmatrix} \mathbf{x} + \begin{bmatrix} (k_{01}^{nlin} + k_{12}^{nlin})x_1^2 + 3k_{12}^{nlin}x_2^2 & -3k_{12}^{nlin}x_1^2 - k_{12}^{nlin}x_2^2 \\ -k_{12}^{nlin}x_1^2 - 3k_{12}^{nlin}x_2^2 & 3k_{12}^{nlin}x_1^2 + (k_{02}^{nlin} + k_{12}^{nlin})x_2^2 \end{bmatrix} \mathbf{x}.$$

As for the single degree of freedom oscillator, the nonlinear electrostatic restoring forces are modeled by Eq. (5.1.3). Adapting this equation to the present system with two degrees of freedom  $x_1$  and  $x_2$ , results in a time dependent stiffness matrix of the following form

$$\mathbf{F}_{es}(\mathbf{x}, t) = \begin{bmatrix} F_{es1}(x_1, t) \\ F_{es2}(x_2, t) \end{bmatrix}, \quad (6.1.5)$$

$$\mathbf{F}_{es}(\mathbf{x}, t) = \mathbf{F}_{es}^{lin}(\mathbf{x}, t) + \mathbf{F}_{es}^{nlin}(\mathbf{x}^3, t),$$

$$\mathbf{F}_{es}(\mathbf{x}, t) = \begin{bmatrix} r_{1A}V_A^2(1 + \cos(\omega t)) & 0 \\ 0 & r_{1A}V_A^2(1 + \cos(\omega t)) \end{bmatrix} \mathbf{x} + \begin{bmatrix} r_{3A}V_A^2x_1^2(1 + \cos(\omega t)) & 0 \\ 0 & r_{3A}V_A^2x_2^2(1 + \cos(\omega t)) \end{bmatrix} \mathbf{x}.$$

The time dependency of that matrix introduces parametric excitation to the system.

## 6.1. Modeling

### 6.1.1 Rescaling displacement and time

For a better interpretation of the upcoming simulation results and efficient numerical treatment, the nonlinear differential equations (6.1.1) are scaled. Therefore a nondimensional parametric excitation frequency  $\Omega$  is introduced. This frequency is related to the actual parametric excitation frequency as follows

$$\Omega = \frac{\omega}{\hat{\omega}}, \quad (6.1.6)$$

where  $\hat{\omega}$  is a characteristic reference frequency. It is common to either choose the systems natural frequency or the natural frequency of a subsystem as reference frequency. In the present case, a linearized version of the system shown in Fig. 6.2 is considered, with all spring constants except  $k_{01}^{lin}$  set to zero. The remaining time-invariant subsystem consist only of mass  $m_1$  and the linear mechanical spring  $k_{01}^{lin}$ . The natural frequency of that subsystem is known to be

$$\hat{\omega} = \sqrt{\frac{k_{01}^{lin}}{m_1}}. \quad (6.1.7)$$

To obtain a scaled system time, a dimensionless time  $\tau$  is introduced by multiplying time  $t$  with the afore defined reference frequency  $\hat{\omega}$

$$\tau = \hat{\omega}t. \quad (6.1.8)$$

That nondimensional time consequently leads to a nondimensional argument of the trigonometric function

$$\omega t = \Omega \hat{\omega} t = \Omega \tau. \quad (6.1.9)$$

The displacements  $x_1$  and  $x_2$  of the oscillator are rescaled according to

$$z_1 = \frac{x_1}{x_0}, \quad z_2 = \frac{x_2}{x_0}, \quad (6.1.10)$$

where  $x_0$  is a scaling parameter introduced to obtain nondimensional system deflections. In order to gain meaningful oscillation amplitudes when applying numerical simulation in the time domain, it is beneficial to use a scaling parameter in the size of the systems physical dimensions (e.g. the maximum possible deflection due to the spacing of the comb fingers).

Carrying out the rescaling substitutions leads to a nondimensional differential equation in matrix form

$$\mathbf{z}'' + \hat{\mathbf{C}}\mathbf{z}' + \hat{\mathbf{F}}_{es}(\mathbf{z}) + \cos(\Omega\tau)\hat{\mathbf{P}}_C(\mathbf{z}) + \hat{\mathbf{F}}_r(\mathbf{z}) = 0. \quad (6.1.11)$$

By splitting the stiffness matrices into linear and nonlinear parts, the differential equations can be rewritten as follows

$$\mathbf{z}'' + \hat{\mathbf{C}}\mathbf{z}' + \hat{\mathbf{F}}_{es}^{lin}(\mathbf{z}) + \hat{\mathbf{F}}_{es}^{nlin}(\mathbf{z}^3) + \cos(\Omega\tau) [\hat{\mathbf{P}}_C^{lin}(\mathbf{z}) + \hat{\mathbf{P}}_C^{nlin}(\mathbf{z}^3)] + \hat{\mathbf{F}}_r^{lin}(\mathbf{z}) + \hat{\mathbf{F}}_r^{nlin}(\mathbf{z}^3) = 0, \quad (6.1.12)$$

whereas the rescaled damping matrix is denoted  $\hat{\mathbf{C}}$  and the vector of deflections  $\mathbf{z}$

$$\hat{\mathbf{C}} = \begin{bmatrix} 2(\xi_{01} + \xi_{12}) & -2\xi_{12} \\ -2\gamma\xi_{12} & 2\gamma(\xi_{02} + \xi_{12}) \end{bmatrix}, \quad \mathbf{z} = \begin{bmatrix} z_1 \\ z_2 \end{bmatrix}. \quad (6.1.13)$$

The rescaled mechanical and electrostatic stiffness matrices are denoted  $\hat{\mathbf{F}}_r$  and  $\hat{\mathbf{F}}_{es}$ , respectively. To clearly point out the parametric excitation mechanism, the time dependent part of the electrostatic stiffness matrix is represented by the coefficient matrix  $\hat{\mathbf{P}}_C$  of the parametric stiffness variation. The definitions of these three matrices are listed below, whereas the newly introduced nondimensional parameters are defined as stated in Table 6.1

$$\hat{\mathbf{F}}_r(\mathbf{z}) = \hat{\mathbf{F}}_r^{lin}(\mathbf{z}) + \hat{\mathbf{F}}_r^{nlin}(\mathbf{z}^3), \quad (6.1.14)$$

$$\hat{\mathbf{F}}_r(\mathbf{z}) = \begin{bmatrix} 1 + \beta_{12} & -\beta_{12} \\ -\gamma\beta_{12} & \gamma(\beta_{02} + \beta_{12}) \end{bmatrix} + \begin{bmatrix} (\chi_{01} + \chi_{12})z_1^2 + 3\chi_{12}z_2^2 & -3\chi_{12}z_1^2 - \chi_{12}z_2^2 \\ -\gamma\chi_{12}z_1^2 - 3\gamma\chi_{12}z_2^2 & 3\gamma\chi_{12}z_1^2 + \gamma z_2^2(\chi_{02} + \chi_{12}) \end{bmatrix} \mathbf{z},$$

$$\hat{\mathbf{F}}_{es}(\mathbf{z}) = \hat{\mathbf{F}}_{es}^{lin}(\mathbf{z}) + \hat{\mathbf{F}}_{es}^{nlin}(\mathbf{z}^3), \quad (6.1.15)$$

$$\hat{\mathbf{F}}_{es}(\mathbf{z}) = \begin{bmatrix} \lambda_1 & 0 \\ 0 & \gamma\lambda_1 \end{bmatrix} \mathbf{z} + \begin{bmatrix} \lambda_3 z_1^2 & 0 \\ 0 & \gamma\lambda_3 z_2^2 \end{bmatrix} \mathbf{z},$$

$$\hat{\mathbf{P}}_C(\mathbf{z}) = \hat{\mathbf{P}}_C^{lin}(\mathbf{z}) + \hat{\mathbf{P}}_C^{nlin}(\mathbf{z}^3), \quad (6.1.16)$$

$$\hat{\mathbf{P}}_C(\mathbf{z}) = \begin{bmatrix} \lambda_1 & 0 \\ 0 & \gamma\lambda_1 \end{bmatrix} \mathbf{z} + \begin{bmatrix} \lambda_3 z_1^2 & 0 \\ 0 & \gamma\lambda_3 z_2^2 \end{bmatrix} \mathbf{z}.$$

## 6.1. Modeling

Definition	Nondimensional parameter
$z'_{1,2} = \frac{dz_{1,2}}{d\tau}$	Scaled time derivative
$\Omega = \frac{\omega}{\hat{\omega}}$	Nondimensional excitation frequency
$\gamma = \frac{m_1}{m_2}$	Mass ratio
$\xi_{01} = \frac{c_{01}}{2m_1\hat{\omega}}$	Scaled damping ratio for $c_{01}$
$\xi_{12} = \frac{c_{12}}{2m_1\hat{\omega}}$	Scaled damping ratio for $c_{12}$
$\xi_{02} = \frac{c_{02}}{2m_1\hat{\omega}}$	Scaled damping ratio for $c_{02}$
$\lambda_1 = \frac{r_{1A}V_A^2}{k_{01}^{lin}}$	Linear electrostatic excitation amplitude
$\lambda_3 = \frac{x_0^2 r_{3A} V_A^2}{k_{01}^{lin}}$	Nonlinear electrostatic excitation coefficient
$\beta_{12} = \frac{k_{12}^{lin}}{k_{01}^{lin}}$	Linear mechanical stiffness quotient
$\beta_{02} = \frac{k_{02}^{lin}}{k_{01}^{lin}}$	Linear mechanical stiffness quotient
$\chi_{01} = \frac{k_{01}^{nl} x_0^2}{k_{01}^{lin}}$	Nonlinear mechanical stiffness coefficient
$\chi_{12} = \frac{k_{12}^{nl} x_0^2}{k_{01}^{lin}}$	Nonlinear mechanical stiffness coefficient
$\chi_{02} = \frac{k_{02}^{nl} x_0^2}{k_{01}^{lin}}$	Nonlinear mechanical stiffness coefficient

Table 6.1: Nondimensional parameter definitions corresponding to Eqs. (6.1.11), adapted from [13].

To prepare the rescaled equations of motion for upcoming numerical simulations they have to be made explicit in its highest derivative. Moreover, the order is reduced by introducing additional equations. This step is necessary to use the nondimensional differential equations with any common simulation software package, as numerical integration is limited to first order differential equations.

$$\mathbf{z}' = \mathbf{u}, \quad (6.1.17)$$

$$\mathbf{u}' = -\left\{ \hat{\mathbf{C}}\mathbf{z}' + \hat{\mathbf{F}}_{es}^{lin}(\mathbf{z}) + \hat{\mathbf{F}}_{es}^{nl}(\mathbf{z}^3) + \cos(\Omega\tau) \left[ \hat{\mathbf{P}}_C^{lin}(\mathbf{z}) + \hat{\mathbf{P}}_C^{nl}(\mathbf{z}^3) \right] + \hat{\mathbf{F}}_r^{lin}(\mathbf{z}) + \hat{\mathbf{F}}_r^{nl}(\mathbf{z}^3) \right\} \quad (6.1.18)$$

### 6.1.2 System parameters

The parameters of the present microelectromechanical system oscillator shown in Fig. 6.2 are basically the same as obtained in Chapter 5 for the single degree of freedom MEMS

Parameter	Value	Dimension unit
$m_1$	$1.22 \times 10^{-10}$	kg
$m_2$	$2.44 \times 10^{-10}$	kg
$c_{01}$	$1.94 \times 10^{-8}$	Ns/m
$c_{12}$	$3.88 \times 10^{-8}$	Ns/m
$c_{02}$	$1.94 \times 10^{-8}$	Ns/m
$k_{01}^{lin}$	3.505	$\mu\text{N}/\mu\text{m}$
$k_{12}^{lin}$	1.753	$\mu\text{N}/\mu\text{m}$
$k_{02}^{lin}$	3.505	$\mu\text{N}/\mu\text{m}$
$k_{01}^{nlin}$	0.018	$\mu\text{N}/\mu\text{m}^3$
$k_{12}^{nlin}$	0.009	$\mu\text{N}/\mu\text{m}^3$
$k_{02}^{nlin}$	0.018	$\mu\text{N}/\mu\text{m}^3$
$r_{1A}$	$3.65 \times 10^{-4}$	$\mu\text{N}/\text{V}^2\mu\text{m}$
$r_{3A}$	$-1.6 \times 10^{-5}$	$\mu\text{N}/\text{V}^2\mu\text{m}^3$

Table 6.2: Parameter values of the two degree of freedom MEMS oscillator.

oscillator. The mechanical spring coefficients  $k_{01}$  and  $k_{02}$  stay exactly the same, whereas the newly introduced spring  $k_{12}$  results from a serial connection of two springs with the same characteristics as  $k_{01}$  and  $k_{02}$ . The system mass  $m_1$  is identical to the mass  $m$  of the single degree of freedom oscillator. In order to detect a significant anti-resonance phenomenon within the system, it is necessary to choose the ratio between the two system masses  $m_1$  and  $m_2$  greater or equal to two.

$$\gamma = \frac{m_1}{m_2} \geq 2 \quad (6.1.19)$$

There is no proof for this condition, but several numerical simulations of parametrically excited systems (e.g. in [5]) have indicated the validity of that recommendation. For the present system the mass  $m_2$  is set to be two times the value of  $m_1$ . The damping coefficients  $c_{01}$  and  $c_{02}$  retain the same value as in the single degree of freedom design shown in Fig. 5.2. The newly introduced damping element  $c_{12}$  results from a serial connection of two dampers with the same characteristics as  $c_{01}$  and  $c_{02}$ . The physical dimensions of the two sets of comb drives are defined to be the same as stated in Table 5.4 for the single degree of freedom oscillator. Therefore, the linear and nonlinear electrostatic coefficients  $r_{1A}$  and  $r_{3A}$  retain the same value as well. Table 6.2 summarizes the obtained parameters for the present oscillator shown in Fig. 6.2.

## 6.2 Linear system

To investigate the stability of the present two degree of freedom microelectromechanical system, its matrix differential equation is first linearized to apply the Floquet method described in Chapter 3. Carrying out the linearization results in the following equations of motion

$$\mathbf{z}'' + \hat{\mathbf{C}}\mathbf{z}' + \hat{\mathbf{F}}_{es}^{lin}(\mathbf{z}) + \cos(\Omega\tau)\hat{\mathbf{P}}_C^{lin}(\mathbf{z}) + \hat{\mathbf{F}}_r^{lin}(\mathbf{z}) = 0, \quad (6.2.1)$$

where the nonlinear stiffness matrices are set to zero

$$\hat{\mathbf{F}}_{es}^{nlin}(\mathbf{z}^3) = \mathbf{0}, \quad \hat{\mathbf{P}}_C^{nlin}(\mathbf{z}^3) = \mathbf{0}, \quad \hat{\mathbf{F}}_r^{nlin}(\mathbf{z}^3) = \mathbf{0}. \quad (6.2.2)$$

### 6.2.1 Numerical stability investigation

In order to obtain the parametric resonances and combination resonances before applying numerical simulation, a modal analysis is carried out on the undamped linear time-invariant (LTI) system. Therefore the rescaled damping matrix  $\hat{\mathbf{C}}$  and the linear coefficient matrix  $\hat{\mathbf{P}}_C^{lin}$  of the parametric stiffness variation are neglected along with the nonlinear stiffness matrices. The matrix differential equation (6.2.1) is thereby further simplified to

$$\mathbf{z}'' + \hat{\mathbf{F}}_{es}^{lin}(\mathbf{z}) + \hat{\mathbf{F}}_r^{lin}(\mathbf{z}) = 0. \quad (6.2.3)$$

As the addition of both stiffness matrices leads to a positive definite matrix, the resulting eigenvalue problem

$$\left[ (\hat{\mathbf{F}}_{es}^{lin} + \hat{\mathbf{F}}_r^{lin}) - \Omega^2 \right] \mathbf{v} = 0, \quad (6.2.4)$$

can be solved using appropriate algorithms. The resulting natural frequencies of the undamped LTI-system

$$\begin{aligned} \Omega_1 &= \min \left( \text{eig} \left( \hat{\mathbf{F}}_{es}^{lin} + \hat{\mathbf{F}}_r^{lin} \right) \right), \\ \Omega_2 &= \max \left( \text{eig} \left( \hat{\mathbf{F}}_{es}^{lin} + \hat{\mathbf{F}}_r^{lin} \right) \right), \end{aligned} \quad (6.2.5)$$

may be arranged in a diagonal matrix as previously shown in Eq. (3.1.6). Due to the rescaling of the differential equations, the natural frequencies obtained are dimensionless.

Description	Parameter	Value
Reference frequency	$\hat{\omega}$	$\sqrt{k_{01}^{lin}/m_1}$
Natural frequency	$\Omega_1$	0.8256
Natural frequency	$\Omega_2$	1.3266
Parametric resonance	$2\Omega_1$	1.6512
Parametric resonance	$2\Omega_2$	2.6532
Combination resonance	$\Omega_1 + \Omega_2$	2.1522
Combination resonance	$\Omega_2 - \Omega_1$	0.501

Table 6.3: Nondimensional parametric resonances and combination resonances obtained through modal analysis.

Table 6.3 summarizes the first parametric resonances and combination resonances for the case where  $n = 1$ . The dimensioned resonance frequencies can easily be calculated using Eq. (6.1.6) together with the definition of the characteristic reference frequency.

If the Floquet method, previously described in Chapter 3.5, is applied to the linearized equations of motion (6.2.1), three-dimensional stability plots can be produced. Two axes are used to vary certain system parameters and the third axis is used to plot the magnitude of the maximum eigenvalue of the monodromy matrix  $\Lambda$ . If that eigenvalue is greater than one, the system is unstable and if it is less than one, the system is stable. Figure 6.3 shows a stability chart where the nondimensional parametric excitation frequency  $\Omega$  is plotted against the amplitude  $V_A$  of the input voltage.

The resulting stability chart is comparable to Fig. 5.11, created for the single degree of freedom system. The only differences are the display format and the different occurring parametric resonances due to the addition of a second degree of freedom. The stability chart shows a good match between the theoretical parametric resonance conditions (3.1.7), (3.1.8) and the numerical simulation (for the case where  $n = 1$ ). Furthermore the instability wedges are again curved, due to the quadratic presence of  $V_A$  in the linear electrostatic excitation amplitude  $\lambda_1$ . As expected, along with the first parametric resonances  $2\Omega_1$  and  $2\Omega_2$  and the first combination resonance  $\Omega_1 + \Omega_2$ , also the anti-resonance phenomenon is detected. Due to the fact that the characteristic of the first parametric anti-resonance at  $\Omega = \Omega_2 - \Omega_1$  is difficult to establish from the stability chart, Fig. 6.4 shows a magnification of the relevant PE-frequency range. It can be seen that the maxima of the eigenvalues of the monodromy matrix decrease in the region near the anti-resonance, indicating that the

## 6.2. Linear system

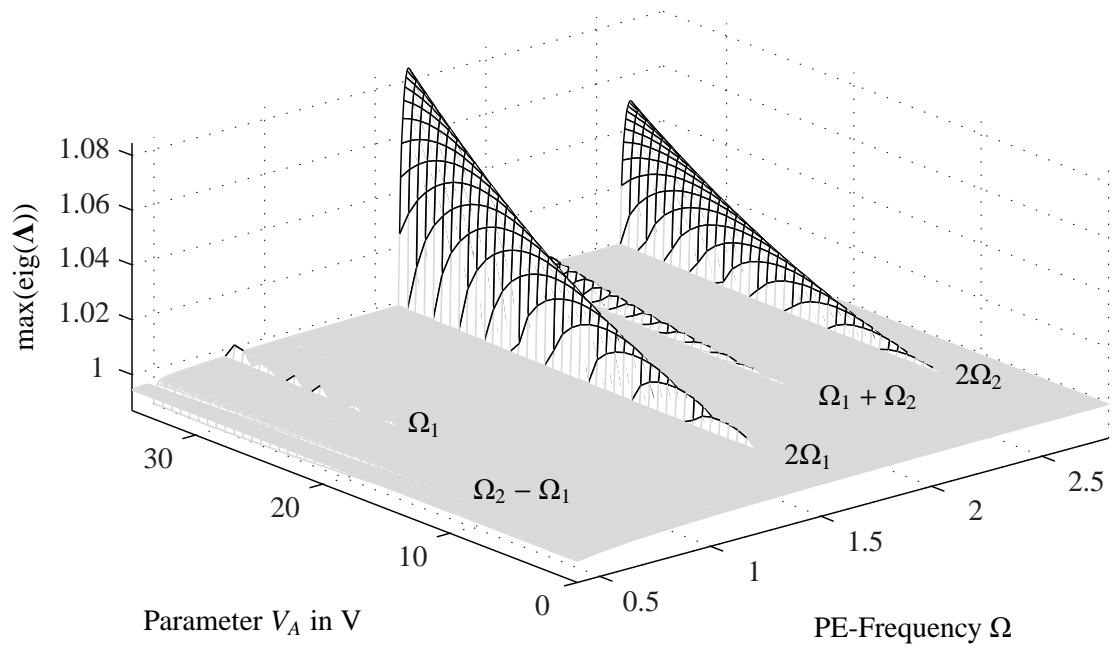


Figure 6.3: Numerical study for PE-Frequency  $\Omega$  and input voltage  $V_A$ . Parameter values are taken from Table 6.2.

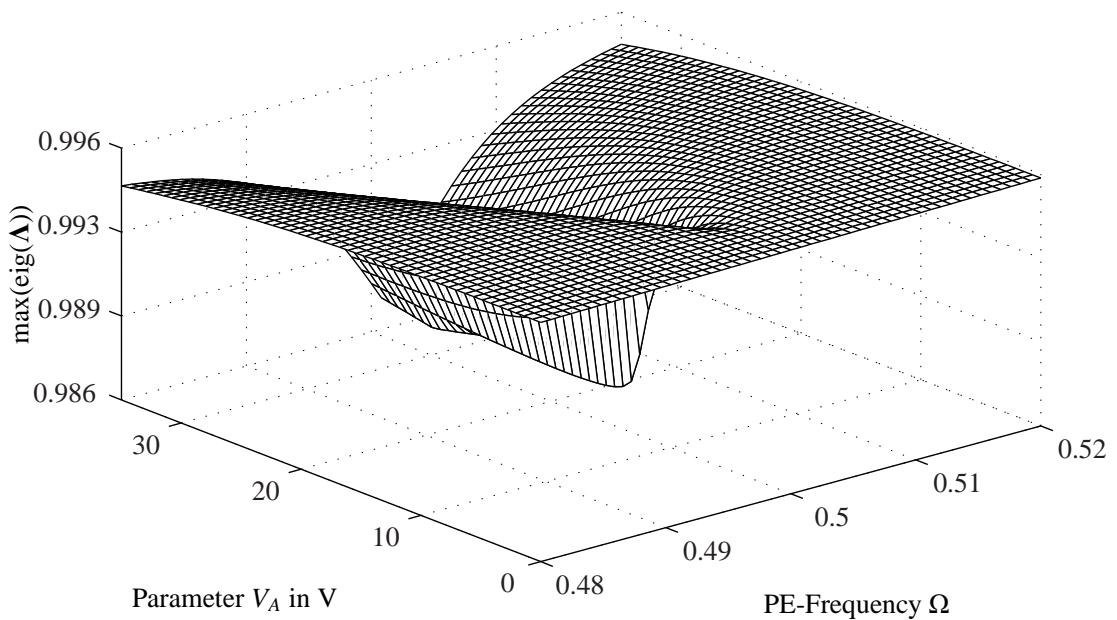


Figure 6.4: Numerical study for PE-Frequency  $\Omega$  and input voltage  $V_A$  showing first anti-resonance  $\Omega_2 - \Omega_1$ . Parameter values are taken from Table 6.2.

system does not only remain in a stable condition, but also its stability may be enhanced. In addition to the first parametric resonances also a higher order resonance at  $\Omega = \Omega_1$  appears in the stability chart. This parametric resonance is due to the present damping of minor importance compared to the first order parametric resonances (see Eq. 3.1.3).

To validate the obtained stability chart, the linearized equations of motion are numerically solved in the time domain. For that, the scaling parameter is set to  $x_0 = 1\mu\text{m}$ . Assuming initial displacements of  $x_{1,2}(t = 0) = 1\mu\text{m}$  and no initial velocities, results in four nondimensional initial conditions of the form

$$z_{1,2}(\tau = 0) = \frac{x_{1,2}(t = 0)}{x_0} = 1, \quad (6.2.6)$$

$$z'_{1,2}(\tau = 0) = 0, \quad (6.2.7)$$

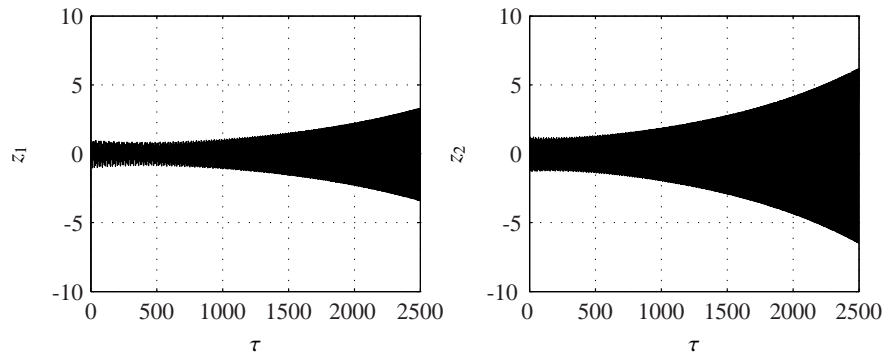
which allow the numerical integration of Eqs. (6.2.1). Figure 6.5 shows the obtained vibrations corresponding to each instability region in Fig. 6.3. The exponential growth of the oscillation amplitudes  $z_1$  and  $z_2$  with time, shows that the system is indeed unstable at excitation frequencies near  $\Omega_1$ ,  $2\Omega_1$ ,  $2\Omega_2$  and  $\Omega_1 + \Omega_2$ .

To show the beneficial characteristic of the parametric anti-resonance phenomenon, the system is analyzed in the time domain and compared to an arbitrarily chosen stable system state. The four initial conditions stated beforehand are used to calculate the vibrations at the parametric excitation frequencies  $\Omega = 2.2$  and  $\Omega = \Omega_2 - \Omega_1$  shown in Fig. 6.6. It can be seen that in both cases the oscillation amplitudes exponentially decrease with time, indicating that the system is stable. The main difference is that the oscillation amplitudes decrease faster when operating the MEMS oscillator at the parametric anti-resonance frequency, meaning that the vibration damping is increased at that specific excitation frequency.

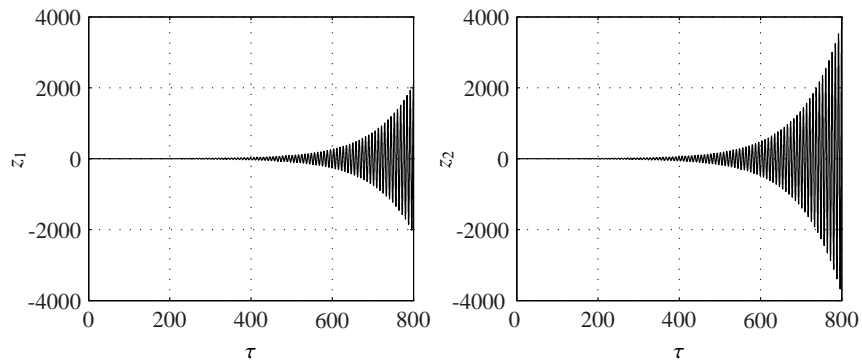
### 6.2.2 Parameter study

The increased vibration damping in the region of the first parametric anti-resonance is a very desirable characteristic, as it may enhance the system's stability. To obtain an oscillator design where that anti-resonance phenomenon occurs at a maximum, a parameter study is carried out. Therefore the Floquet method is well suited, because the stability of the system can be analyzed using relatively few computational time. By varying every linear system parameter in a separate simulation, they can be optimized with respect to the

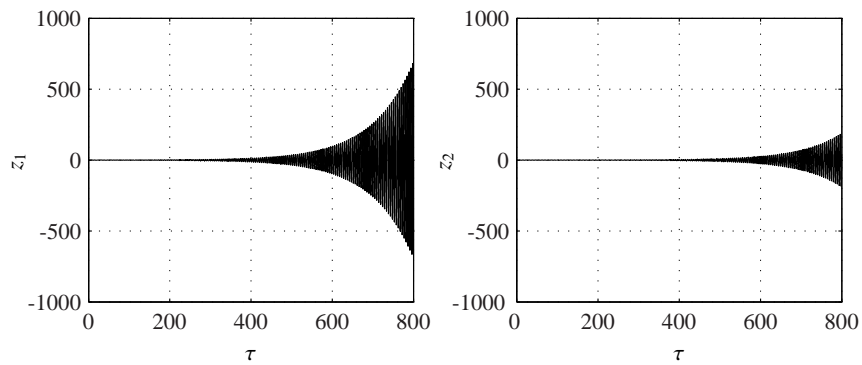
## 6.2. Linear system



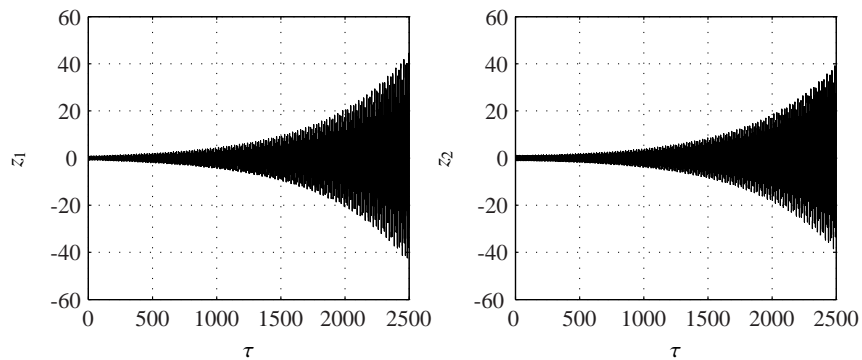
(a) Displacements  $z_1, z_2$  of the linearized system at  $\Omega = \Omega_1$  and  $V_A = 35\text{V}$ .



(b) Displacements  $z_1, z_2$  of the linearized system at  $\Omega = 2\Omega_1$  and  $V_A = 25\text{V}$ .

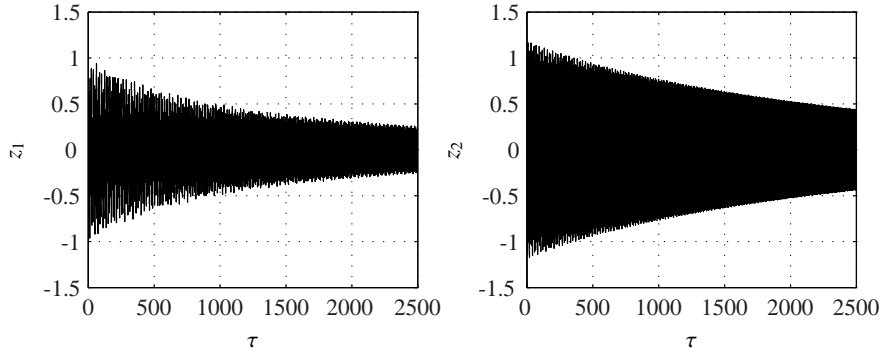
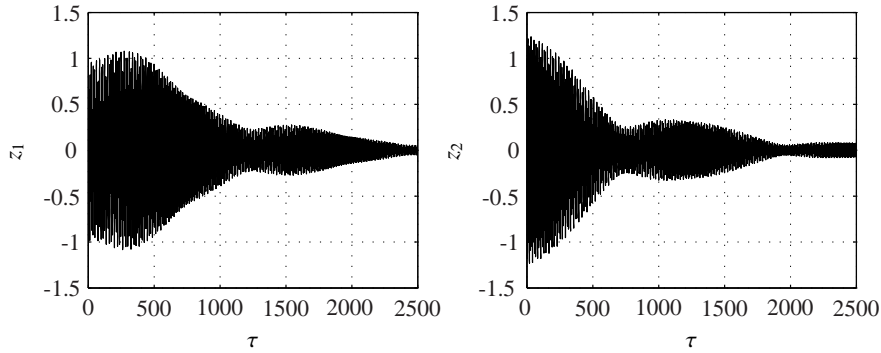


(c) Displacements  $z_1, z_2$  of the linearized system at  $\Omega = 2\Omega_2$  and  $V_A = 25\text{V}$ .



(d) Displacements  $z_1, z_2$  of the linearized system at  $\Omega = \Omega_1 + \Omega_2$  and  $V_A = 25\text{V}$ .

Figure 6.5: Displacements  $z_1, z_2$  at PE-Resonances  $\Omega_1, 2\Omega_1, 2\Omega_2$  and  $\Omega_1 + \Omega_2$  with default parameters taken from Table 6.2.

(a) Displacements  $z_1, z_2$  of the linearized system at  $\Omega = 2.2$  and  $V_A = 25V$ .(b) Displacements  $z_1, z_2$  of the linearized system at  $\Omega = \Omega_2 - \Omega_1$  and  $V_A = 25V$ .Figure 6.6: Displacements  $z_1, z_2$  at PE-Frequency  $\Omega = 2.2$  and first anti-resonance  $\Omega_2 - \Omega_1$  with default parameters taken from Table 6.2.

anti-resonance phenomenon. In the three dimensional diagrams depicted in Figs. 6.8-6.17 a), the nondimensional parametric excitation frequency  $\Omega$  is plotted on one axis and the magnitude of the maximum eigenvalue of the monodromy matrix  $\Lambda$  is plotted on the other. The remaining third axis is used to alternately plot one of the linear system parameters. To maintain the clarity of the three dimensional figures, a minimum step size must be used for the nondimensional excitation frequency and the corresponding linear system parameter. Due to that step size, the depiction of the first anti-resonance is not always clearly resolved and may be ragged. In order to properly detect the maximum occurrence of the first anti-resonance, additional diagrams are attached (see Figs. 6.8-6.17 b). These show the difference between the magnitude of the maximum eigenvalue  $\max(\text{eig}(\Lambda))$  at the frequency  $\Omega = \Omega_2 - \Omega_1$  and a frequency close-by. The anti-resonance phenomenon occurs at a maximum where that difference  $\Delta\max(\text{eig}(\Lambda))$  reaches its maximum. Figure 6.7 illustrates that method, whereas the calculation algorithm is defined as follows

## 6.2. Linear system

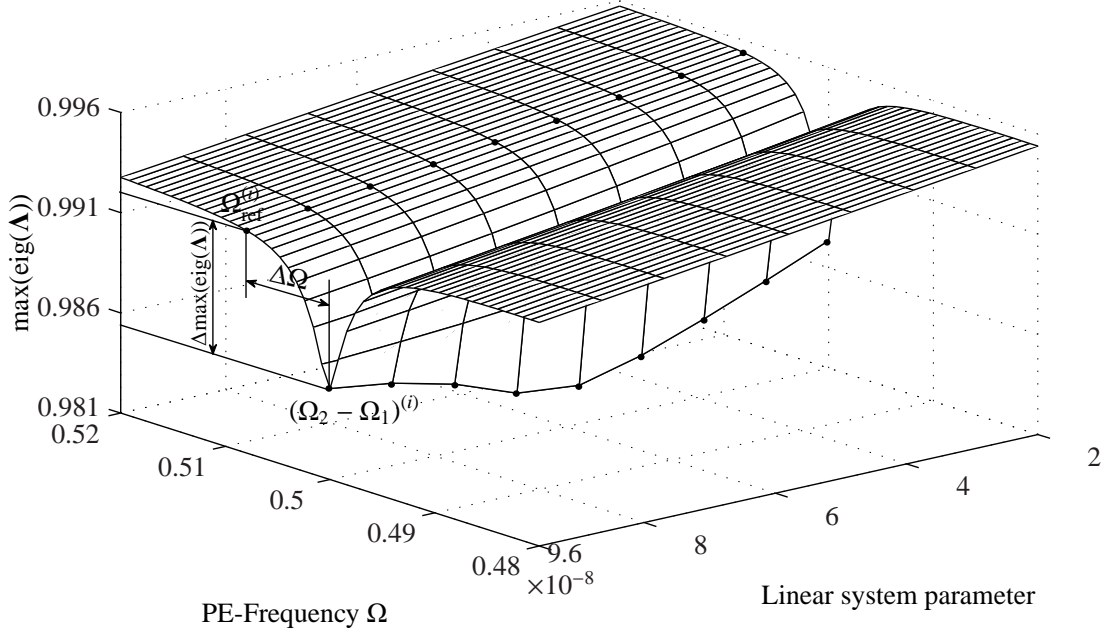


Figure 6.7: Method to detect the maximum occurrence of the first anti-resonance  $\Omega_2 - \Omega_1$ .

$$\Delta\max(\text{eig}(\mathbf{\Lambda})) = \max(\text{eig}(\mathbf{\Lambda}))\left(\Omega_{\text{ref}}^{(i)}\right) - \max(\text{eig}(\mathbf{\Lambda}))\left((\Omega_2 - \Omega_1)^{(i)}\right), \quad i = 1 \dots j. \quad (6.2.8)$$

The discretization of the parametric excitation frequency is represented by the variable  $i$  that ranges from one to  $j$ , where  $j$  is the number of discretization steps. As the anti-resonance frequency may change with a varying linear system parameter, it is constantly recalculated using Eqs. (6.2.5).

- *Numerical studies for masses  $m_1$  and  $m_2$ :*

Figure 6.8 a) shows the first anti-resonance  $\Omega = \Omega_2 - \Omega_1$  for a varying system mass  $m_1$ . It can be seen that a change in mass leads to a curved anti-resonance region due to its presence in the  $\hat{\mathbf{F}}_{es}$  and  $\hat{\mathbf{F}}_r$  matrices, which define the natural frequencies (eigenvalues) of the undamped LTI-system. The corresponding Fig. 6.8 b) indicates that at a mass of  $m_1 = 1.8 \times 10^{-10}\text{kg}$ , the occurrence of the anti-resonance has a local maximum. Figure 6.9 again shows the first anti-resonance, but for a varying mass  $m_2$ . The corresponding Fig. 6.9 b) indicates that the occurrence of the anti-resonance has a local maximum at the same value as mass  $m_1$ . This can be explained by the neglect of the influence that both parameters have on each other. To achieve a

desired mass ratio  $\gamma$  that fulfills condition (6.1.19) the second mass is set to a value of  $m_2 = 3.6 \times 10^{-10}$  kg.

- *Numerical studies for damping coefficients  $c_{01}, c_{12}$  and  $c_{02}$ :*

Concerning the damping coefficients  $c_{01}$  and  $c_{12}$ , Figs. 6.10 and 6.11 clearly illustrate that the occurrence of the anti-resonance has a well pronounced maximum, at a value of  $6.0 \times 10^{-8}$  Ns/m. On the other hand, the result of the numerical study for damping coefficient  $c_{02}$ , depicted in Fig. 6.12, shows that the occurrence of the anti-resonance has a maximum at a value of  $c_{02} = 2.0 \times 10^{-8}$  Ns/m. Compared to the simulation studies for the system masses, the anti-resonance region is not curved. That is because the damping has no notable effect on the natural frequencies of the system. It is therefore reasonable to neglect its influence for theoretical modal analysis (see Eq. 6.2.3).

- *Numerical studies for mechanical stiffness coefficients  $k_{01}^{lin}, k_{12}^{lin}$  and  $k_{02}^{lin}$ :*

The results of the numerical studies concerning the linear mechanical stiffness coefficients are shown in Figs. 6.13 a), 6.14 a) and 6.15 a). As the system masses, the mechanical stiffness coefficients have a major impact on the natural frequencies of the system as well, resulting in a curvature of the anti-resonance region. The corresponding Figs. 6.13 b), 6.14 b) and 6.15 b) indicate that the occurrence of the first anti-resonance has a maximum at stiffness values of  $k_{01}^{lin} = 1.9 \mu\text{N}/\mu\text{m}$ ,  $k_{12}^{lin} = 1.4 \mu\text{N}/\mu\text{m}$  and  $k_{02}^{lin} = 8.0 \mu\text{N}/\mu\text{m}$ .

- *Numerical study for linear electrostatic coefficient  $r_{1A}$ :*

Analyzing the occurrence of the first anti-resonance by varying the linear electrostatic coefficient  $r_{1A}$ , results in Fig. 6.16 a). It can be seen that the parameter  $r_{1A}$  needs to exceed a certain threshold, in order to enable an occurrence of the anti-resonance effect. Furthermore the occurrence reaches its local maximum at a value of  $r_{1A} = 3.8 \times 10^{-4} \mu\text{N}/\text{V}^2\mu\text{m}$ , indicated by Fig. 6.16 b).

- *Numerical study for alternating voltage amplitude  $V_A$ :*

The numerical study for the amplitude  $V_A$  of the input signal is depicted in Fig. 6.17 a) and shows the same characteristic as the study for the linear electrostatic stiffness coefficient  $r_{1A}$ . The parameter  $V_A$  needs to exceed a certain threshold to enable an occurrence of the anti-resonance effect and reaches a local maximum at a value of

## 6.2. Linear system

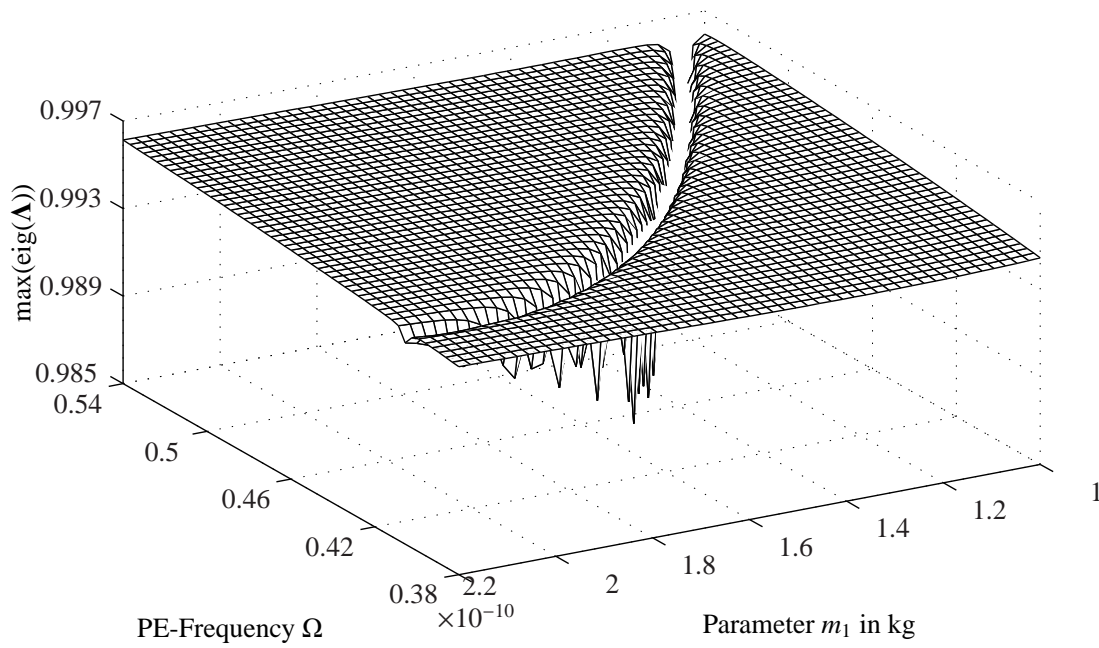
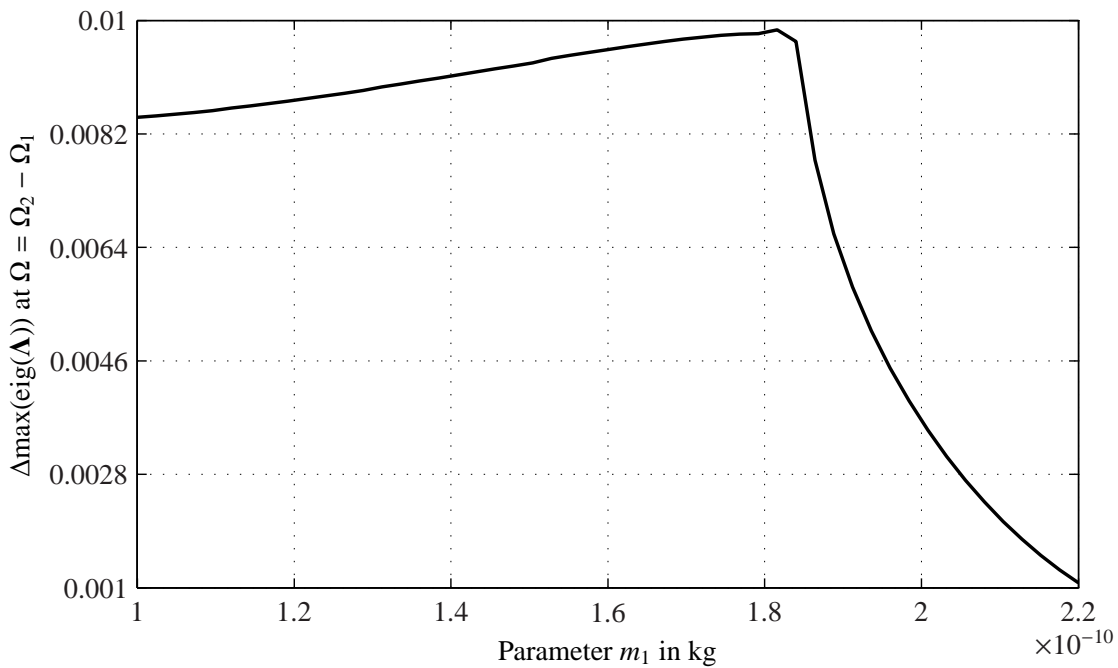
Parameter	Value	Dimension unit	$\Delta\Omega$	$j$
$m_1$	$1.8 \times 10^{-10}$	kg	0.016	50
$m_2$	$3.6 \times 10^{-10}$	kg	0.016	50
$c_{01}$	$6.0 \times 10^{-8}$	Ns/m	0.008	50
$c_{12}$	$6.0 \times 10^{-8}$	Ns/m	0.008	50
$c_{02}$	$4.0 \times 10^{-7}$	Ns/m	0.008	50
$k_{01}^{lin}$	1.9	$\mu\text{N}/\mu\text{m}$	0.036	50
$k_{12}^{lin}$	1.4	$\mu\text{N}/\mu\text{m}$	0.022	50
$k_{02}^{lin}$	8.0	$\mu\text{N}/\mu\text{m}$	0.024	50
$r_{1A}$	$3.8 \times 10^{-4}$	$\mu\text{N}/\text{V}^2\mu\text{m}$	0.012	50
$V_A$	16	V	0.016	50

Table 6.4: Optimized parameter values of the linearized two degree of freedom MEMS.

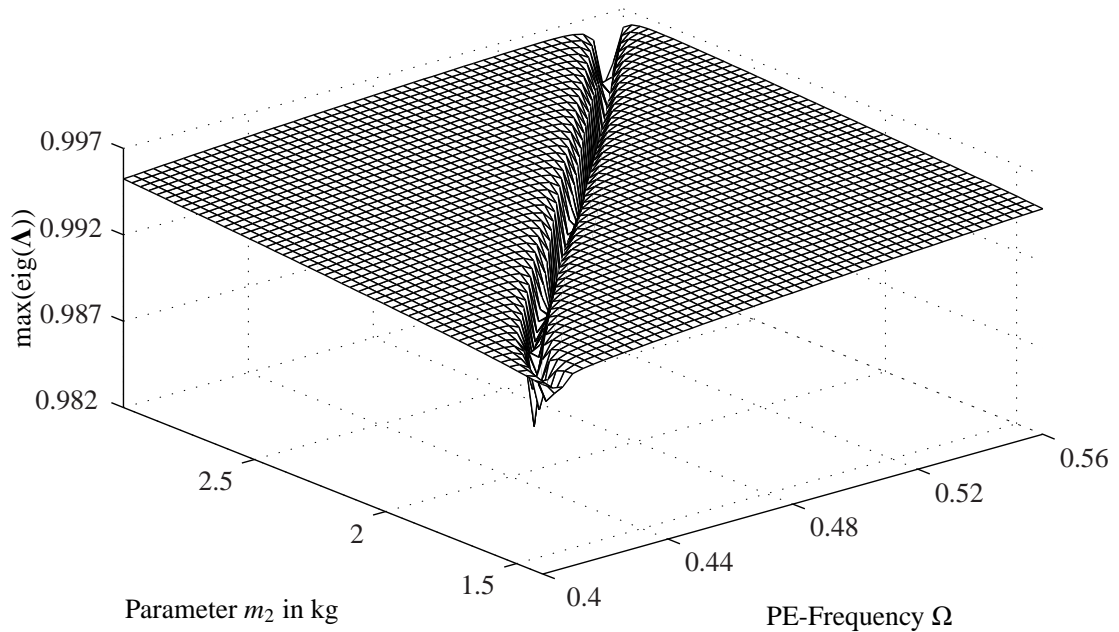
$V_A = 16\text{V}$ , as can be seen in Fig. 6.17 b). This similar characteristic arises because both parameters contribute to the linear electrostatic excitation amplitude  $\lambda_1$ . Due to the quadratic presence of  $V_A$  in  $\lambda_1$ , it has a greater influence on the natural frequencies than the linear electrostatic coefficient  $r_{1A}$ . This is evidenced by a slight shift of the first anti-resonance frequency shown in Fig. 6.17 a), between a parameter range of 20 to 40V. This shift is not properly detected by the algorithm stated in Eq. (6.2.8), because the calculation of the anti-resonance frequency  $(\Omega_2 - \Omega_1)^{(i)}$  is based on the undamped LTI-system, which is a simplified model. This results in a decrease of  $\Delta\max(\text{eig}(\mathbf{\Lambda}))$  after passing a value of  $V_A = 16\text{V}$  shown in Fig. 6.17 b). If Fig. 6.17 a) is examined more closely, it can be seen that  $\Delta\max(\text{eig}(\mathbf{\Lambda}))$  actually remains at more or less the same value after passing the point where  $V_A = 16\text{V}$ . Therefore the parameter maximum shown in Fig. 6.17 b) is a bit falsified, but it is still reasonable to choose  $V_A = 16\text{V}$  as the local optimum.

Table 6.4 summarizes the linear system parameters, individually optimized for a maximum occurrence of the first anti-resonance  $\Omega = \Omega_2 - \Omega_1$ . Additionally, the frequency shift  $\Delta\Omega$  between the reference frequency  $\Omega_{\text{ref}}^{(i)}$  and the anti-resonance frequency  $(\Omega_2 - \Omega_1)^{(i)}$ , along with the number of increments  $j$ , is stated.

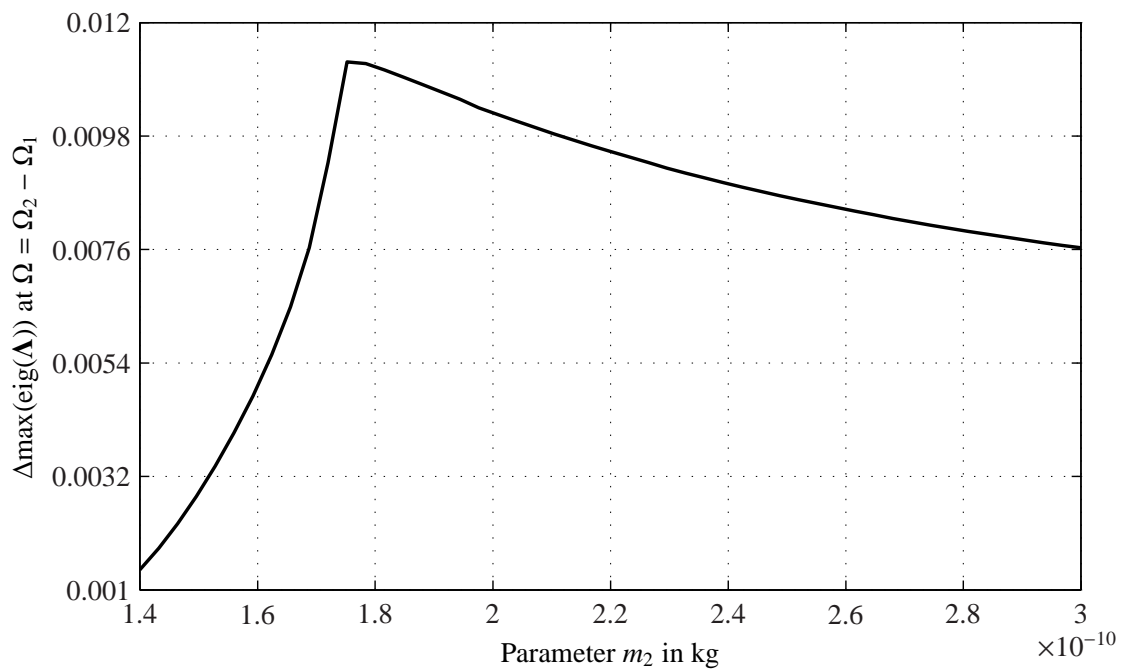
To obtain the exact set of parameters where the anti-resonance occurs at a maximum, the influence of the parameters among each other must be considered as well. As no global optimization has been carried out in this thesis, the individually optimized parameters stated in Table 6.4 can only be seen as an approximation for the actual global parameter optimum.

(a) Parameter study for the first anti-resonance  $\Omega_2 - \Omega_1$  with parameters from Table 6.2.(b) Difference of maximum eigenvalue at first anti-resonance  $\Omega_2 - \Omega_1$  with parameters from Table 6.2.Figure 6.8: Numerical study for PE-Frequency  $\Omega$  and mass  $m_1$ .

## 6.2. Linear system

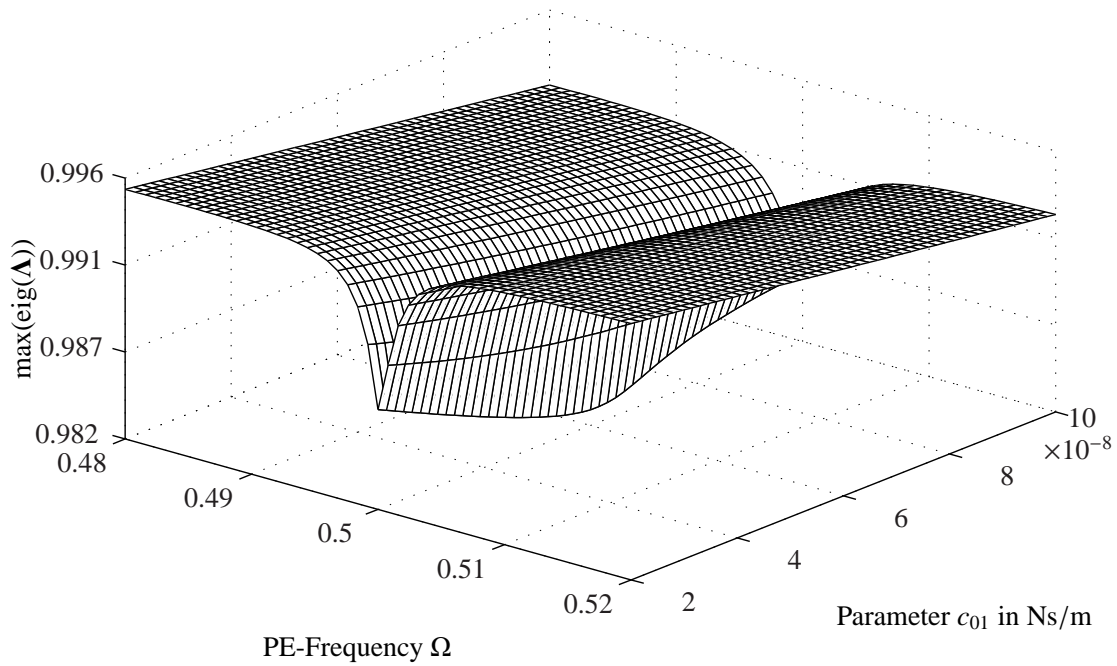


(a) Parameter study for the first anti-resonance  $\Omega_2 - \Omega_1$  with parameters from Table 6.2.

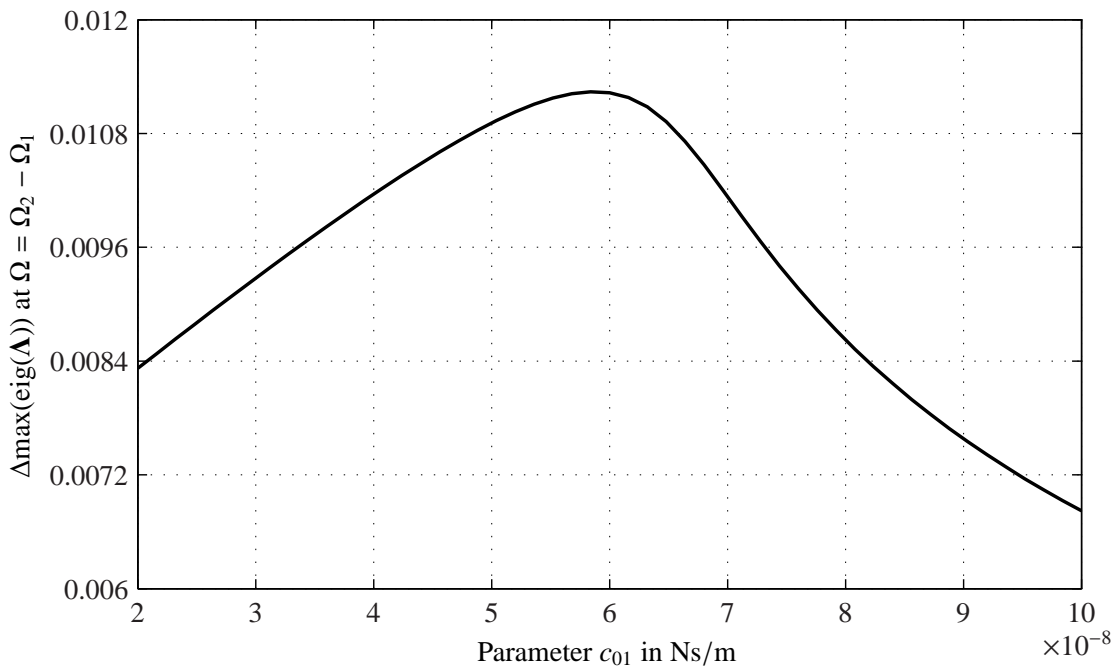


(b) Difference of maximum eigenvalue at first anti-resonance  $\Omega_2 - \Omega_1$  with parameters from Table 6.2.

Figure 6.9: Numerical study for PE-Frequency  $\Omega$  and mass  $m_2$ .



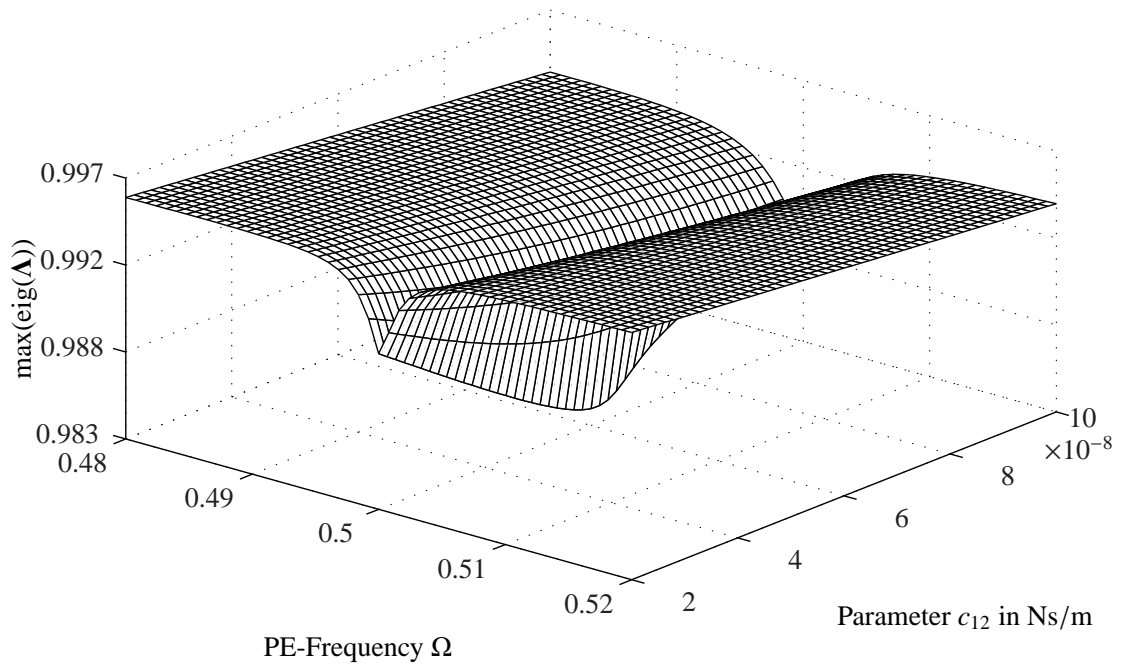
(a) Parameter study for the first anti-resonance  $\Omega_2 - \Omega_1$  with parameters from Table 6.2.



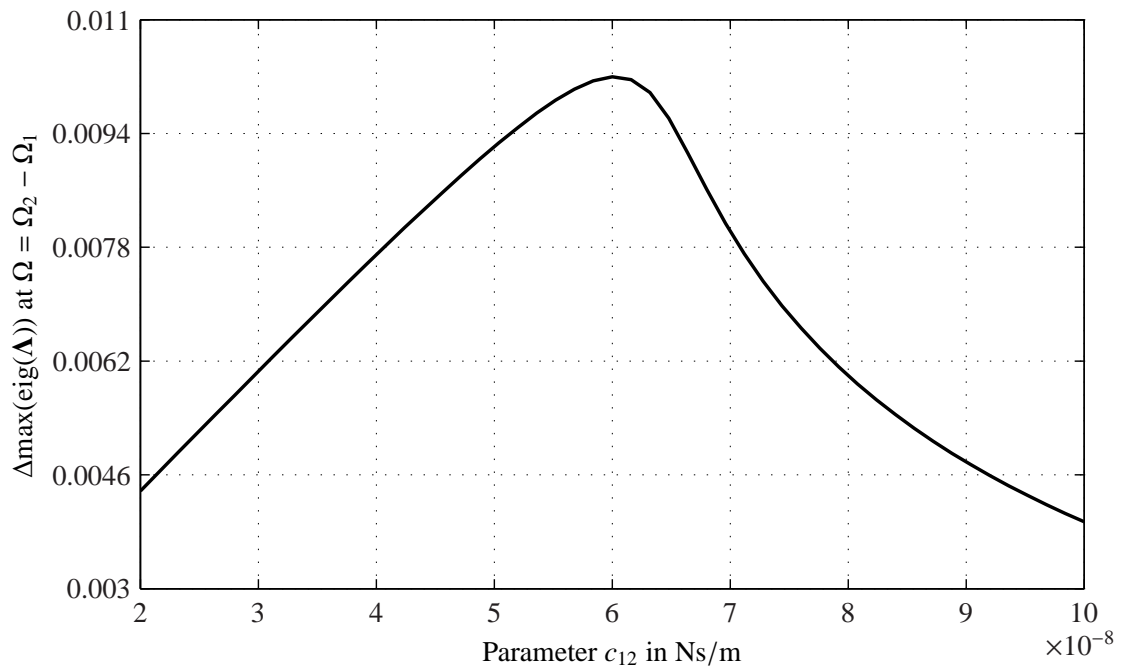
(b) Difference of maximum eigenvalue at first anti-resonance  $\Omega_2 - \Omega_1$  with parameters from Table 6.2.

Figure 6.10: Numerical study for PE-Frequency  $\Omega$  and damping coefficient  $c_{01}$ .

## 6.2. Linear system

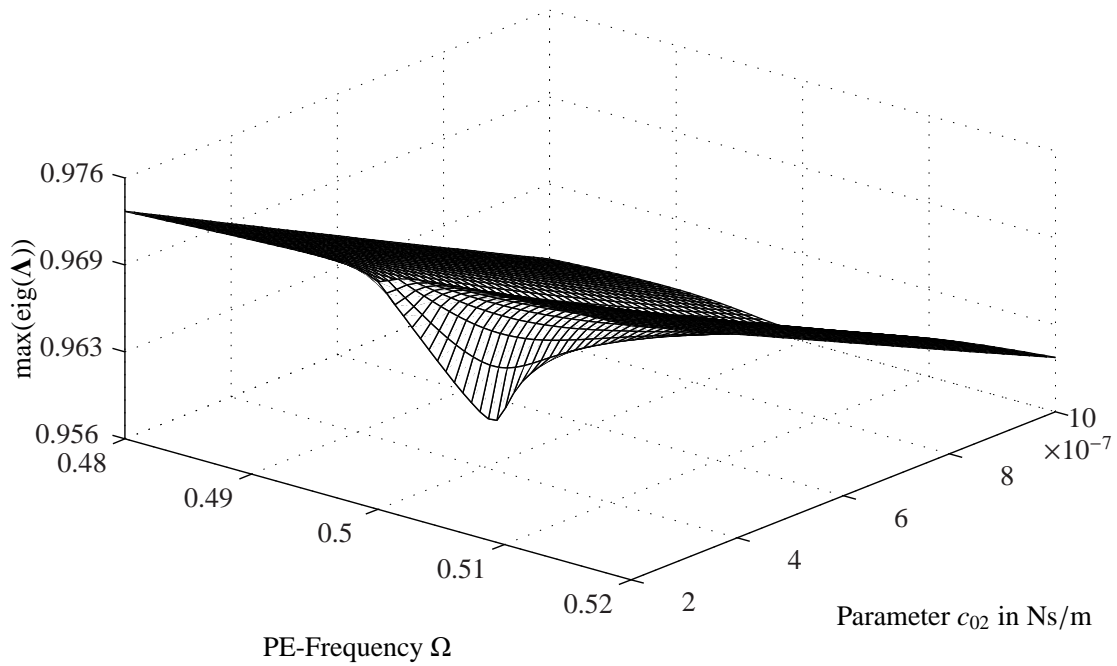


(a) Parameter study for the first anti-resonance  $\Omega_2 - \Omega_1$  with parameters from Table 6.2.

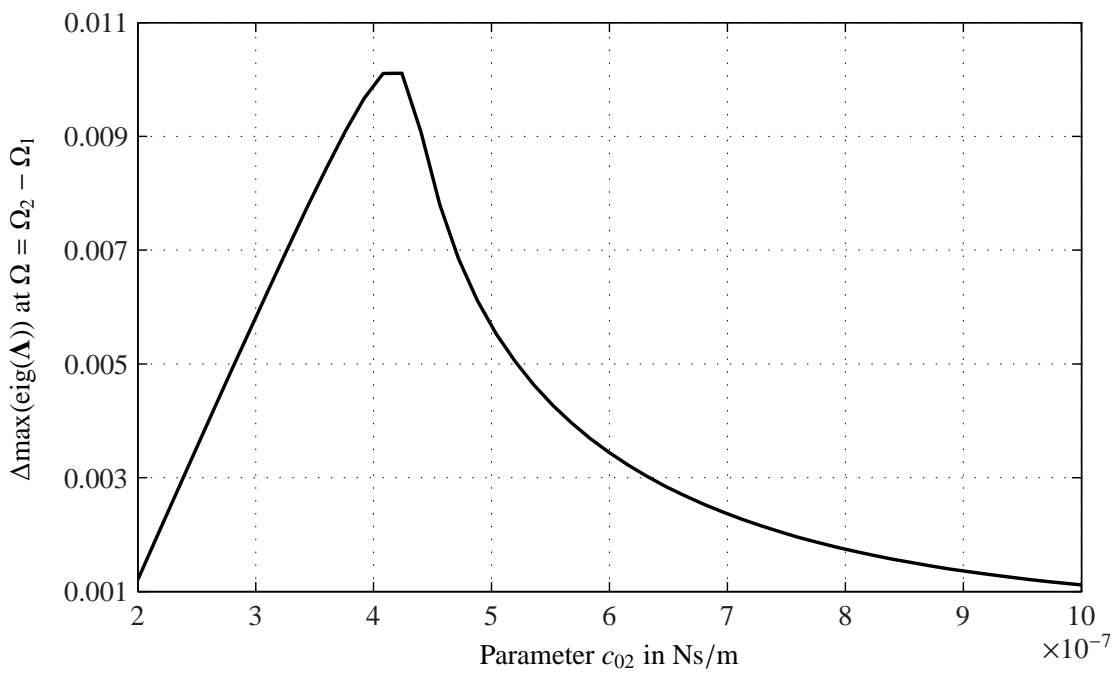


(b) Difference of maximum eigenvalue at first anti-resonance  $\Omega_2 - \Omega_1$  with parameters from Table 6.2.

Figure 6.11: Numerical study for PE-Frequency  $\Omega$  and damping coefficient  $c_{12}$ .



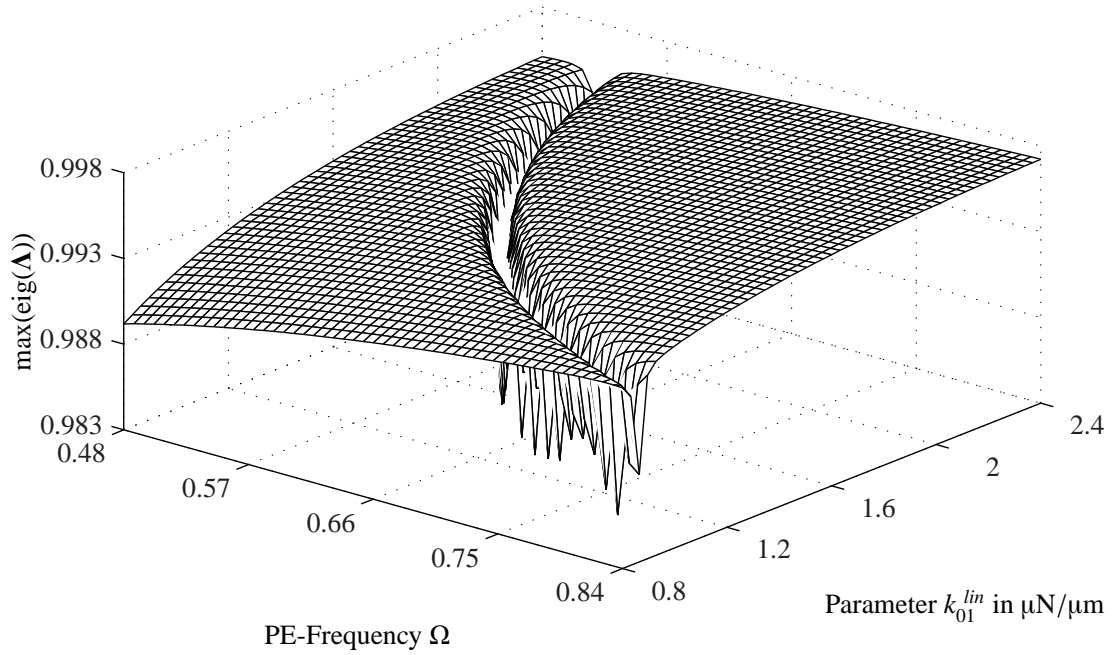
(a) Parameter study for the first anti-resonance  $\Omega_2 - \Omega_1$  with parameters from Table 6.2.



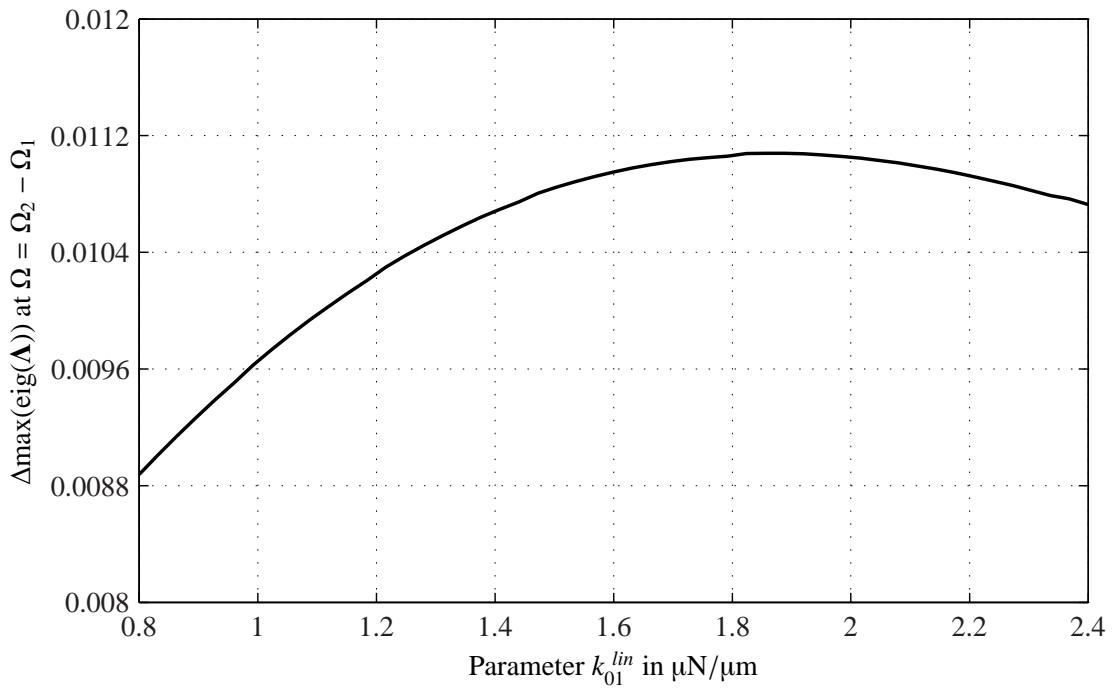
(b) Difference of maximum eigenvalue at first anti-resonance  $\Omega_2 - \Omega_1$  with parameters from Table 6.2.

Figure 6.12: Numerical study for PE-Frequency  $\Omega$  and damping coefficient  $c_{02}$ .

## 6.2. Linear system

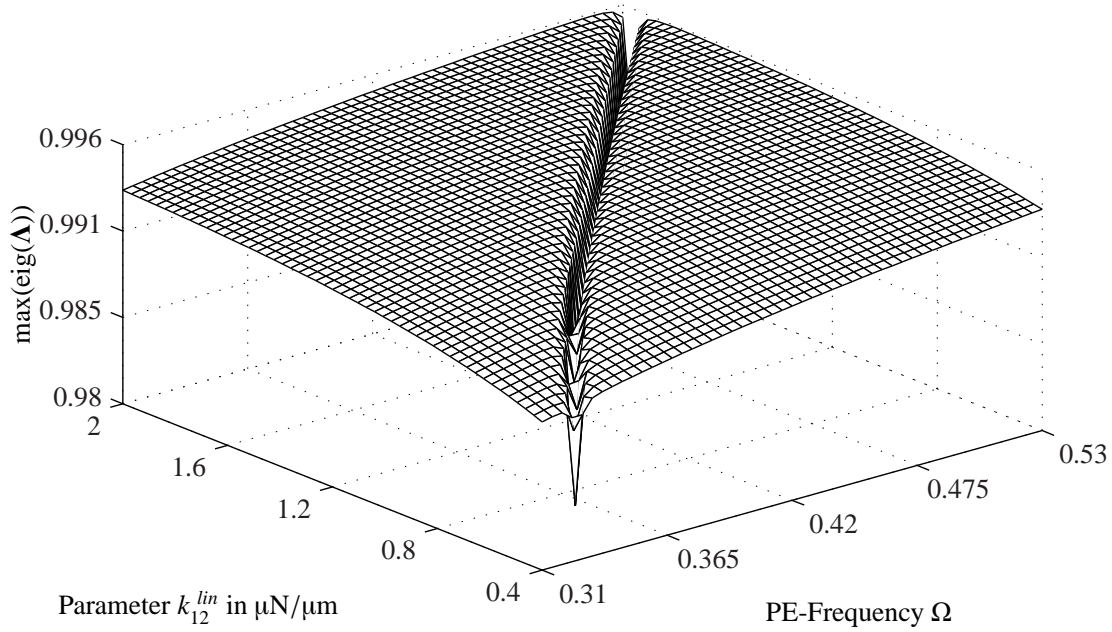


(a) Parameter study for the first anti-resonance  $\Omega_2 - \Omega_1$  with parameters from Table 6.2.

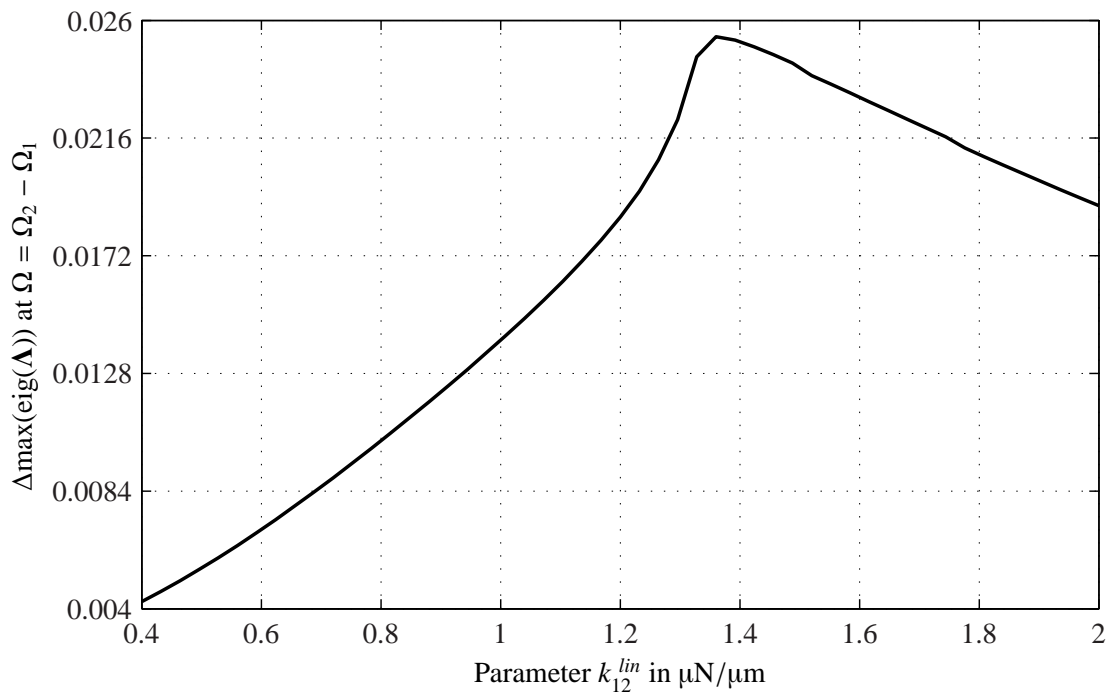


(b) Difference of maximum eigenvalue at first anti-resonance  $\Omega_2 - \Omega_1$  with parameters from Table 6.2.

Figure 6.13: Numerical study for PE-Frequency  $\Omega$  and mechanical stiffness coefficient  $k_{01}^{lin}$ .



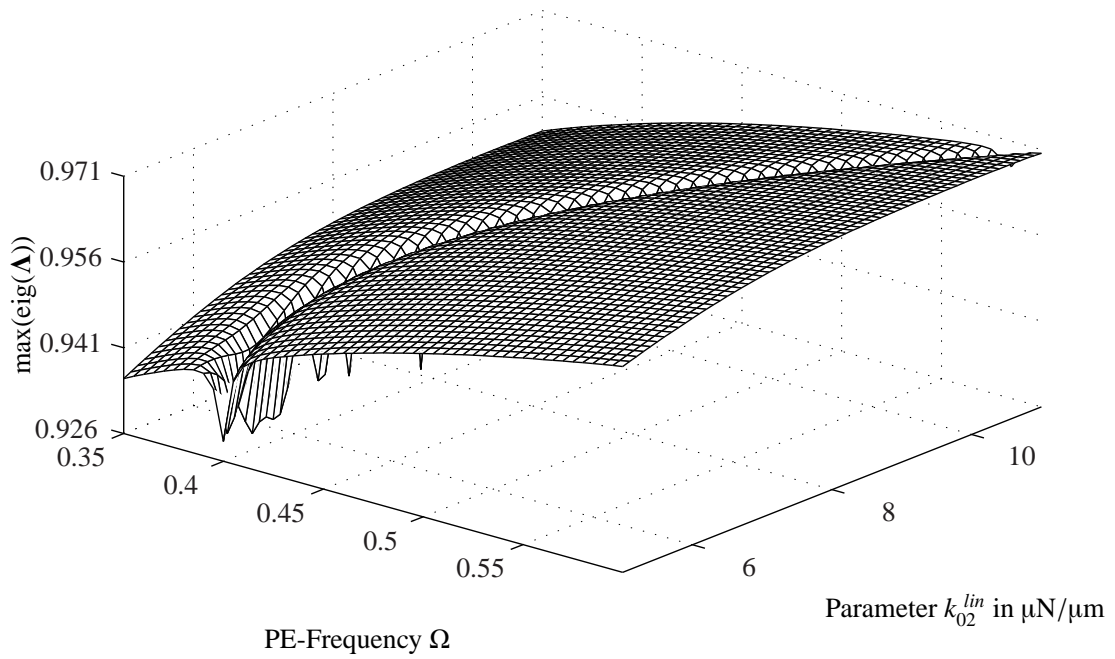
(a) Parameter study for the first anti-resonance  $\Omega_2 - \Omega_1$  with parameters from Table 6.2.



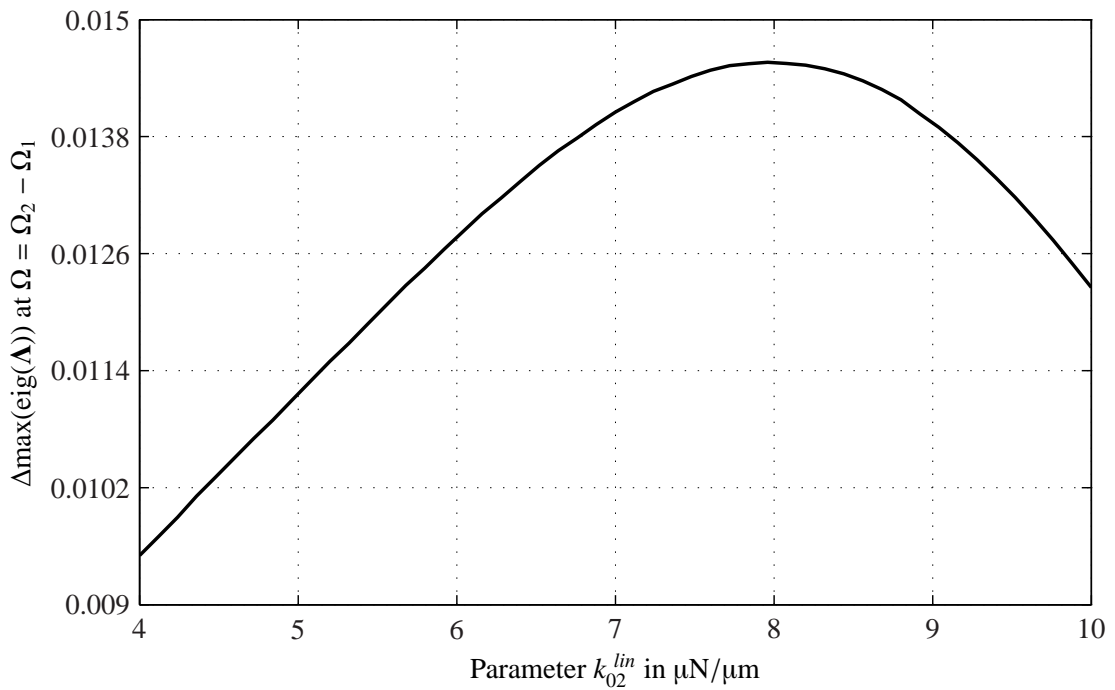
(b) Difference of maximum eigenvalue at first anti-resonance  $\Omega_2 - \Omega_1$  with parameters from Table 6.2.

Figure 6.14: Numerical study for PE-Frequency  $\Omega$  and mechanical stiffness coefficient  $k_{12}^{lin}$ .

## 6.2. Linear system

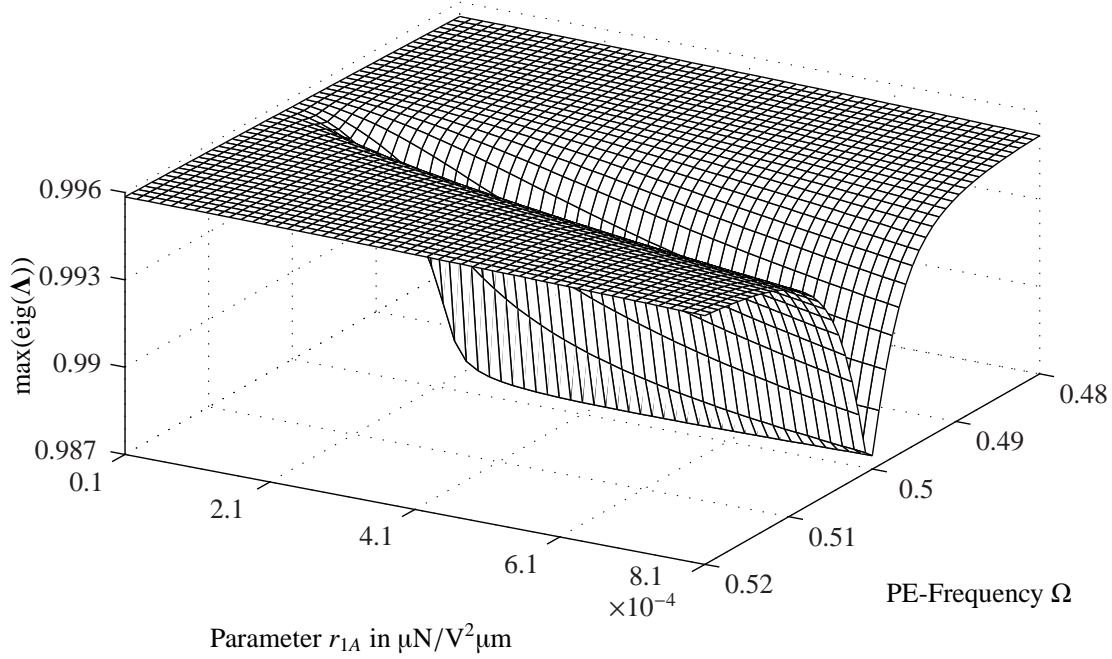


(a) Parameter study for the first anti-resonance  $\Omega_2 - \Omega_1$  with parameters from Table 6.2.

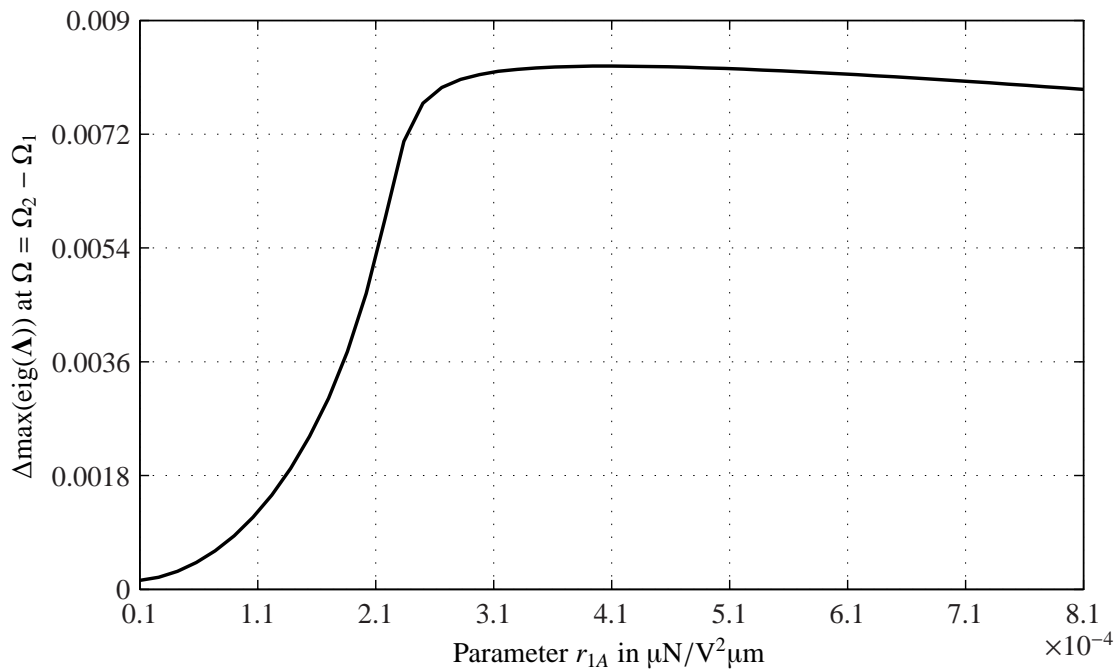


(b) Difference of maximum eigenvalue at first anti-resonance  $\Omega_2 - \Omega_1$  with parameters from Table 6.2.

Figure 6.15: Numerical study for PE-Frequency  $\Omega$  and mechanical stiffness coefficient  $k_{02}^{lin}$ .



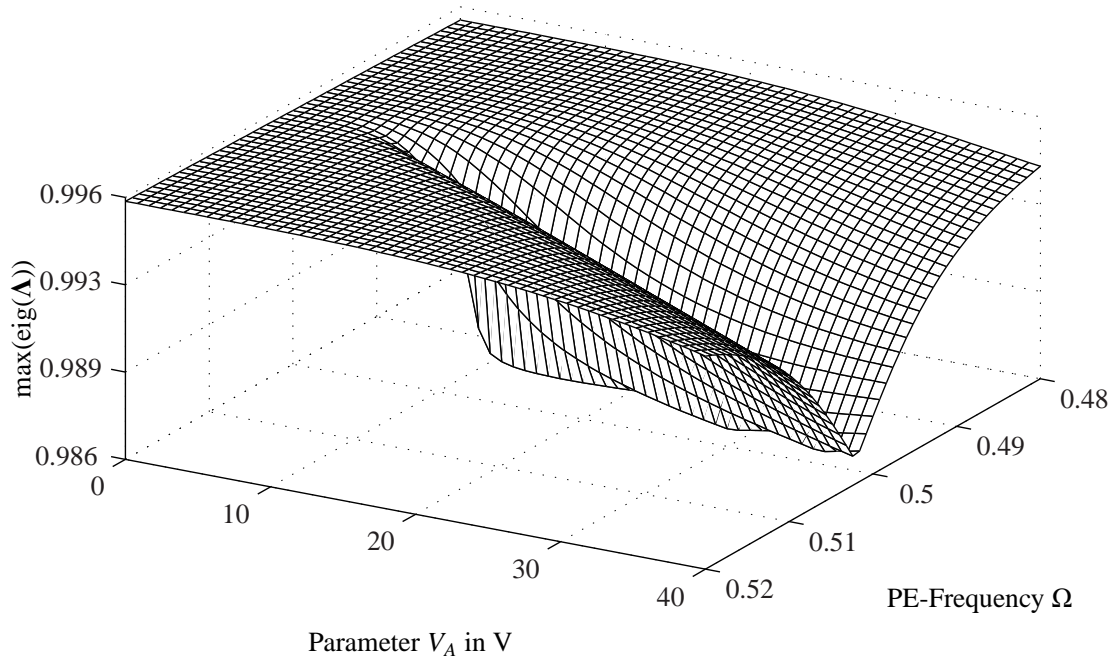
(a) Parameter study for the first anti-resonance  $\Omega_2 - \Omega_1$  with parameters from Table 6.2.



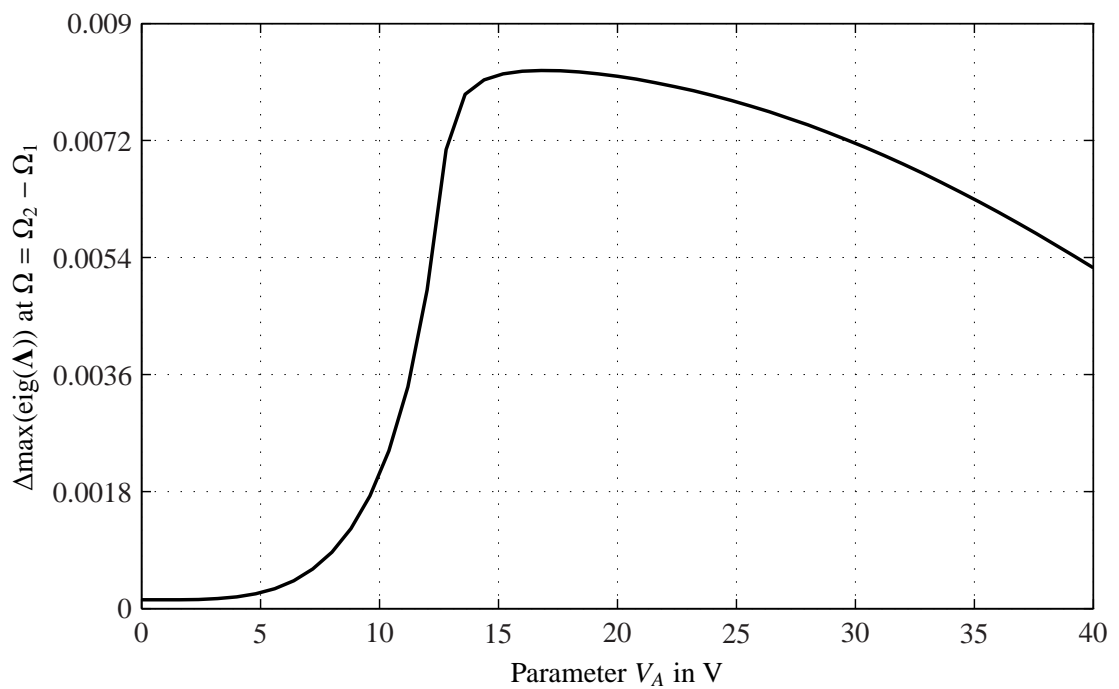
(b) Difference of maximum eigenvalue at first anti-resonance  $\Omega_2 - \Omega_1$  with parameters from Table 6.2.

Figure 6.16: Numerical study for PE-Frequency  $\Omega$  and linear electrostatic coefficient  $r_{1A}$ .

## 6.2. Linear system



(a) Parameter study for the first anti-resonance  $\Omega_2 - \Omega_1$  with parameters from Table 6.2.



(b) Difference of maximum eigenvalue at first anti-resonance  $\Omega_2 - \Omega_1$  with parameters from Table 6.2.

Figure 6.17: Numerical study for PE-Frequency  $\Omega$  and alternating voltage amplitude  $V_A$ .

By taking the parameters from Table 6.4 as a basis for another numerical study where the linear stiffness coefficient  $k_{02}^{lin}$  is optimized with respect to the first parametric anti-resonance, the difference between the individually optimized parameters (Table 6.4) and the global parameter optimum can be estimated. Figure 6.18 indicates that the occurrence of the first anti-resonance has a maximum at a value of  $k_{02}^{lin} = 7.5\text{Ns/m}$ . Assuming that this value represents the global optimum, results in a difference between the local and global optimum of

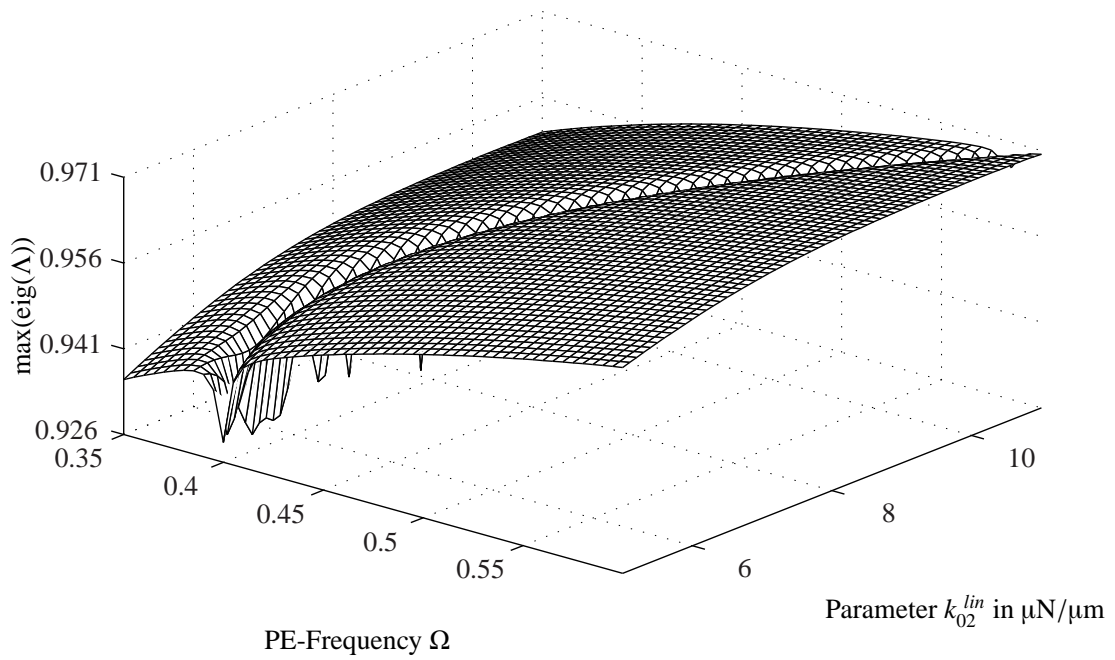
$$\Delta = 100 \cdot \left( 1 - \frac{k_{02, global}^{lin}}{k_{02, local}^{lin}} \right) = 6.25\%. \quad (6.2.9)$$

That difference suggests that the parameter study is a feasible approximation for the global parameter optimum with respect to the first parametric anti-resonance.

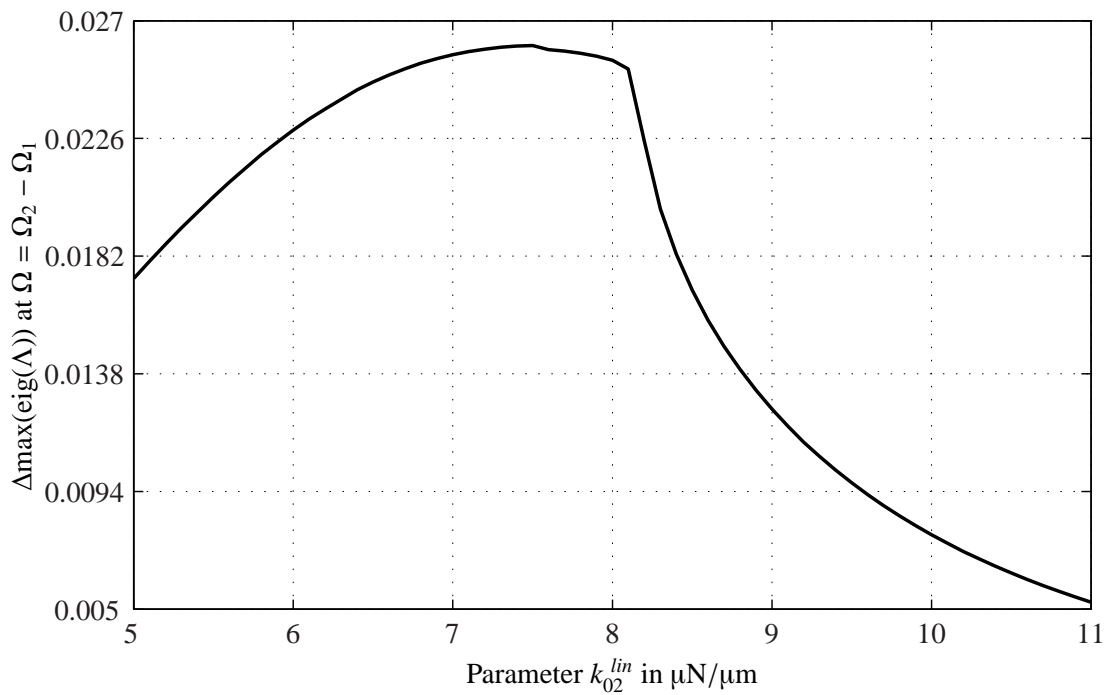
To visualize the effect of the parameter optimization, the occurrence of the first anti-resonance at  $\Omega = \Omega_2 - \Omega_1$  is analyzed with two different sets of parameters. Figure 6.19 a) shows a stability chart using the non-optimized (default) linear system parameters stated in Table 6.2. In comparison to that, Fig. 6.19 b) shows a stability chart using the optimized linear system parameters, gathered through the parameter study and stated in Table 6.4.

A comparison of both stability charts shows that the set of optimized parameters leads to a more pronounced occurrence of the first anti-resonance than the set of default parameters. As the magnitude of the maximum eigenvalue does not directly reflect the oscillation amplitudes, both stability charts are just an indication for the actual occurrence of the anti-resonance. To verify that estimation, the system is analyzed in the time domain as well. Taking initial conditions (6.2.6) and (6.2.7), allow the numerical integration of the linearized matrix differential equation (6.2.1), leading to Fig. 6.20. Due to the decrease of the oscillation amplitudes with time, both displacement plots reveal a stable system behavior, as expected when operating the oscillator near the first anti-resonance frequency. By examining Fig. 6.20 b) closely, it can be seen that the oscillation amplitude grows from  $z_1(\tau = 0) = 1$  to a value of  $z_1 = 1.5$  within a very short time  $\tau$ , before exponentially decreasing over the remaining time. It can as well be seen that this exponential decrease of the amplitudes  $z_1$  and  $z_2$  in Fig. 6.20 b), is more pronounced than in Fig. 6.20 a). This fact acknowledges the premise that the set of optimized parameters leads to a stronger occurrence of the anti-resonance phenomenon. The displacement plots as well prove that a more pronounced occurrence of the anti-resonance connotes enhanced vibration damping.

## 6.2. Linear system

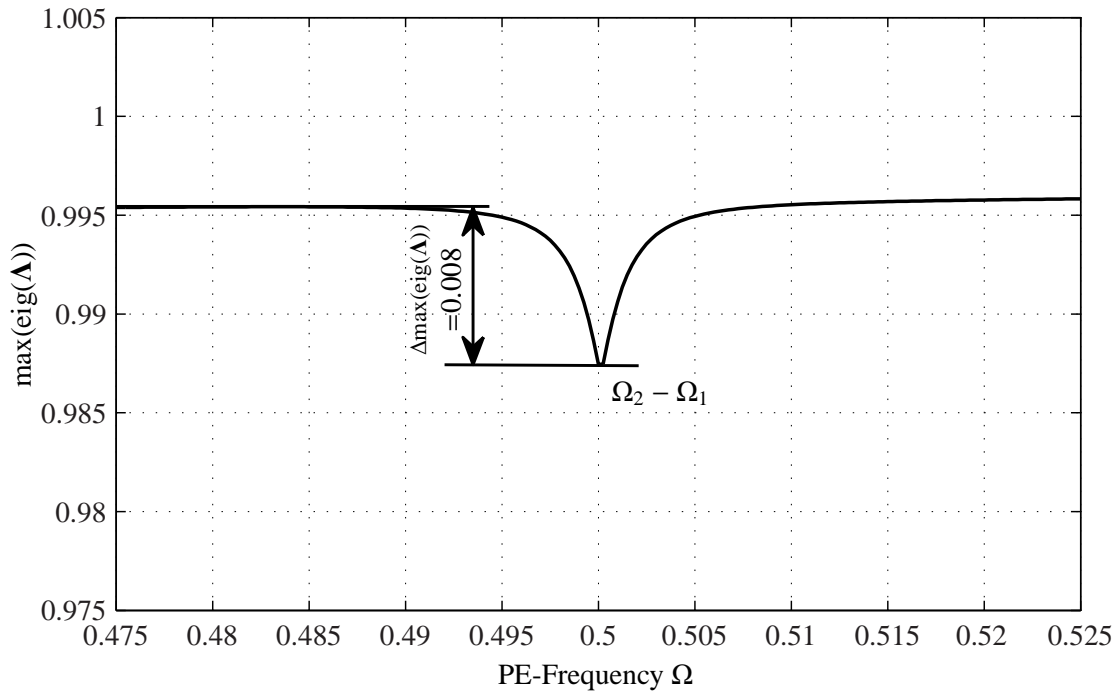


(a) Parameter study for the first anti-resonance  $\Omega_2 - \Omega_1$  with parameters from Table 6.4.

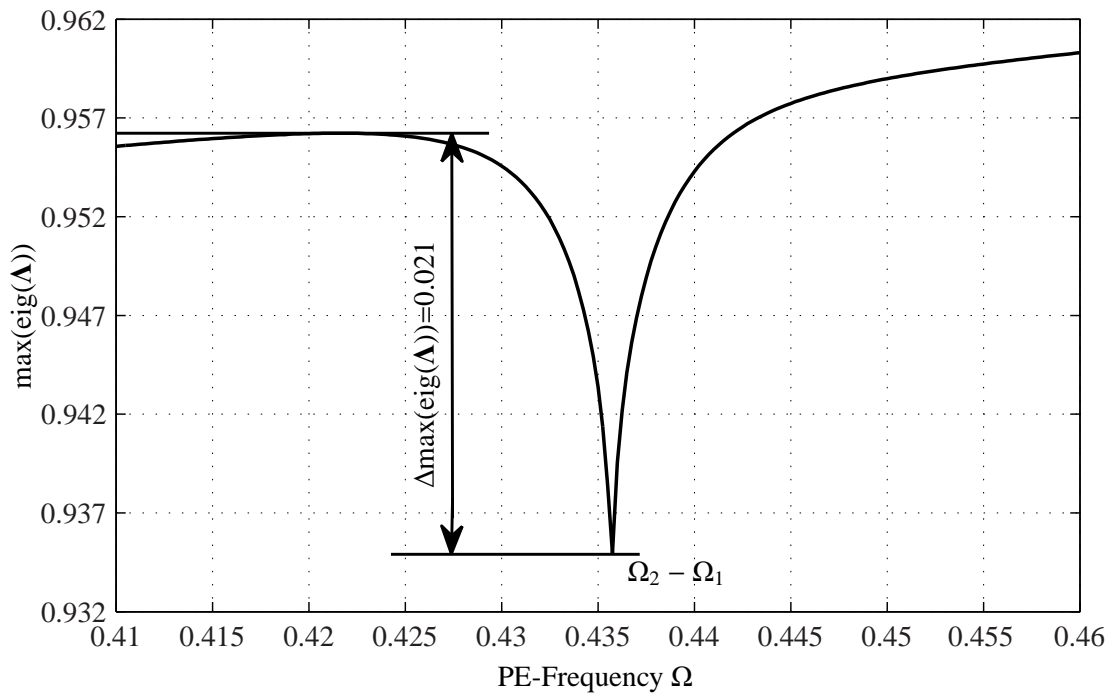


(b) Difference of maximum eigenvalue at first anti-resonance  $\Omega_2 - \Omega_1$  with parameters from Table 6.4.

Figure 6.18: Approximated global anti-resonance optimum for PE-Frequency  $\Omega$  and stiffness coefficient  $k_{02}^{lin}$ .



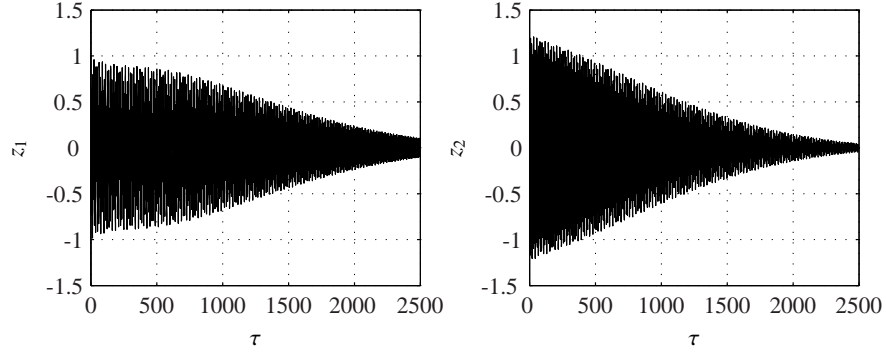
a) First anti-resonance at  $\Omega = \Omega_2 - \Omega_1$  and  $V_A = 16\text{V}$  with default parameters taken from Table 6.2.



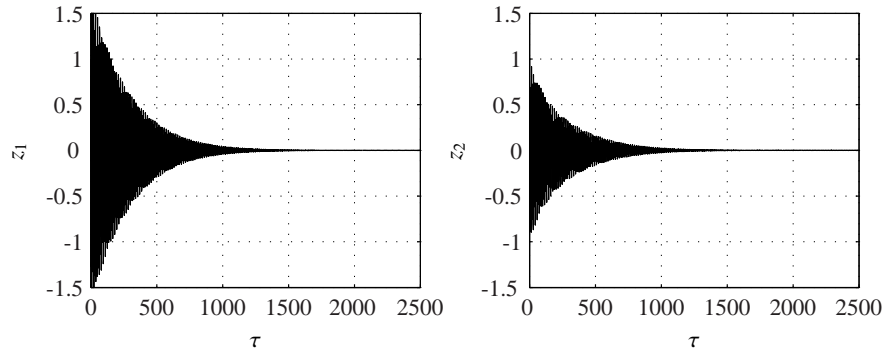
b) First anti-resonance at  $\Omega = \Omega_2 - \Omega_1$  and  $V_A = 16\text{V}$  with optimized parameters taken from Table 6.4.

Figure 6.19: Stability charts showing first anti-resonance at  $\Omega = \Omega_2 - \Omega_1$  with different sets of parameters.

### 6.3. Nonlinear system



(a) Displacements  $z_1, z_2$  of the linearized system at  $\Omega = \Omega_2 - \Omega_1$  with  $V_A = 16V$  and default parameters taken from Table 6.2.



(b) Displacements  $z_1, z_2$  of the linearized system at  $\Omega = \Omega_2 - \Omega_1$  with  $V_A = 16V$  and optimized parameters taken from Table 6.4.

Figure 6.20: Displacements  $z_1, z_2$  at  $\Omega = \Omega_2 - \Omega_1$  with different sets of parameters.

## 6.3 Nonlinear system

To investigate the influence of the nonlinearities on the system behavior, the previously neglected matrices for the nonlinear terms are taken into account

$$\hat{\mathbf{F}}_{es}^{nlin}(\mathbf{z}^3) \neq \mathbf{0}, \quad \hat{\mathbf{P}}_C^{nlin}(\mathbf{z}^3) \neq \mathbf{0}, \quad \hat{\mathbf{F}}_r^{nlin}(\mathbf{z}^3) \neq \mathbf{0}, \quad (6.3.1)$$

resulting in the following nonlinear matrix differential equation already obtained at the start of this chapter

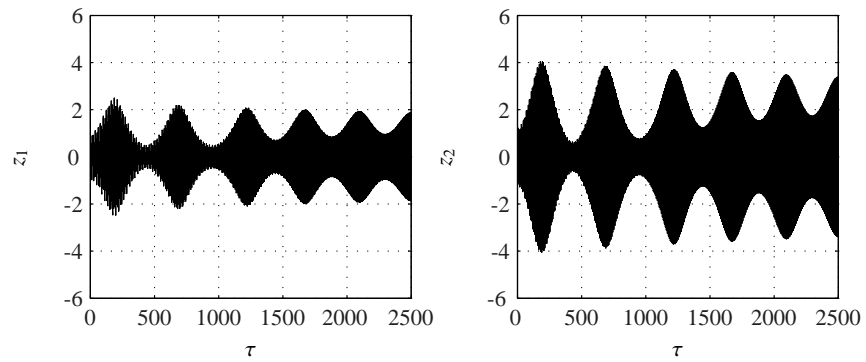
$$\mathbf{z}'' + \hat{\mathbf{C}}\mathbf{z}' + \hat{\mathbf{F}}_{es}^{lin}(\mathbf{z}) + \hat{\mathbf{F}}_{es}^{nlin}(\mathbf{z}^3) + \cos(\Omega\tau) \left[ \hat{\mathbf{P}}_C^{lin}(\mathbf{z}) + \hat{\mathbf{P}}_C^{nlin}(\mathbf{z}^3) \right] + \hat{\mathbf{F}}_r^{lin}(\mathbf{z}) + \hat{\mathbf{F}}_r^{nlin}(\mathbf{z}^3) = \mathbf{0}. \quad (6.3.2)$$

### 6.3.1 Numerical stability investigation

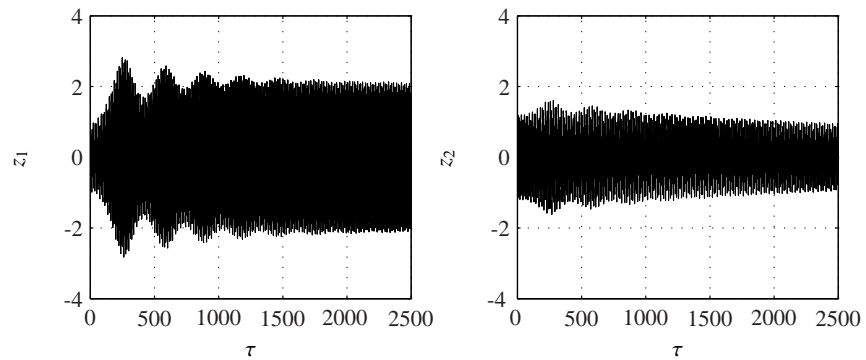
To analyze the stability of the system, the given nonlinear matrix differential equation is solved in the time domain by using initial conditions (6.2.6) and (6.2.7). Figure 6.21 shows displacement plots at characteristic frequencies. As with the single degree of freedom oscillator, the nonlinearities cause the oscillation amplitudes to reach a limit cycle. This can easily be seen by comparing the displacement plots of the linearized system in Fig. 6.5 with the ones shown in Fig. 6.21. It can as well be seen that for the three parametric resonances considered, the intervals of instability do not change by including nonlinear effects.

Figure 6.21 d) shows the displacements  $z_1$  and  $z_2$  at the first anti-resonance  $\Omega = \Omega_2 - \Omega_1$ . Comparing that plot to the one shown in Fig. 6.20 a), leads to the conclusion that the consideration of the nonlinearities has no remarkable effect on the resulting vibrations. The reason for this is that the nonlinear mechanical and electrostatic stiffness coefficients are much smaller than their linear counterparts. Thus, it is confirmed that the nonlinearities have no negative consequences for the exploitation of the parametric anti-resonance phenomenon and hence, the performed linear stability analysis and parameter study are appropriate methods of investigation.

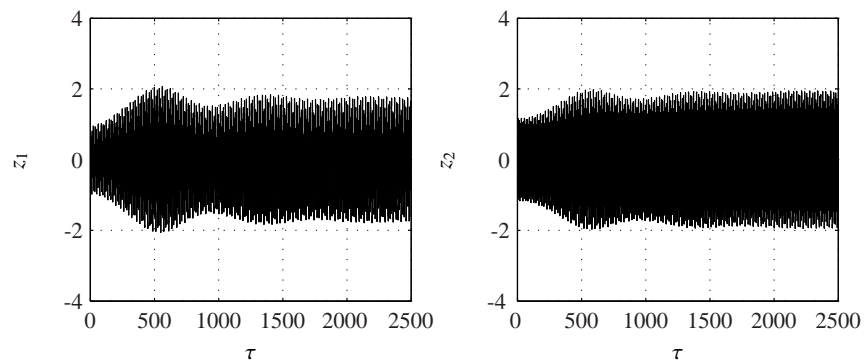
### 6.3. Nonlinear system



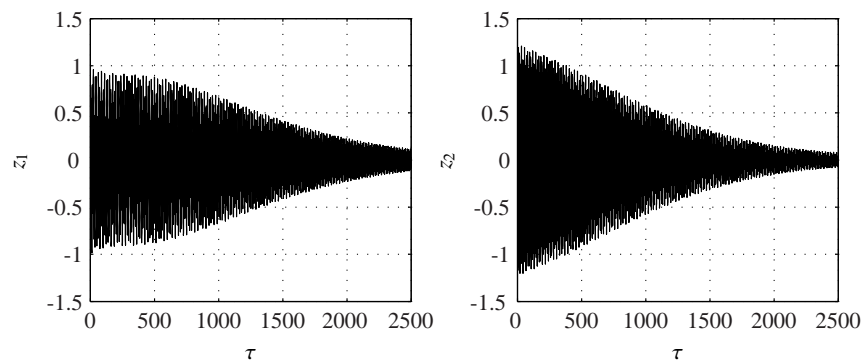
(a) Displacements  $z_1, z_2$  at  $\Omega = 2\Omega_1$  with  $V_A = 25V$ .



(b) Displacements  $z_1, z_2$  at  $\Omega = 2\Omega_2$  with  $V_A = 25V$ .



(c) Displacements  $z_1, z_2$  at  $\Omega = \Omega_1 + \Omega_2$  with  $V_A = 25V$ .



(d) Displacements  $z_1, z_2$  at  $\Omega = \Omega_2 - \Omega_1$  with  $V_A = 16V$ .

Figure 6.21: Displacements  $z_1, z_2$  at PE-Resonances  $2\Omega_1$ ,  $2\Omega_2$ ,  $\Omega_1 + \Omega_2$  and  $\Omega_2 - \Omega_1$  with  $V_A = 25V$  and default parameters taken from Table 6.2.

# Optimized MEMS design with respect to the parametric anti-resonance phenomenon

By the parameter study described in Chapter 6, the linear system parameters have been optimized with respect to the first antiresonance, occurring at a frequency of  $\Omega = \Omega_2 - \Omega_1$ . The further aim is to create an oscillator design that is represented by a mechanical model according to the optimized parameters summarized in Table 6.4. To achieve that, the first step is to identify the beam lengths corresponding to the optimized linear mechanical stiffness coefficients  $k_{01}^{lin}$ ,  $k_{12}^{lin}$  and  $k_{02}^{lin}$ . Then the two sets of comb drives need to be designed in a way that they match the optimized linear electrostatic coefficient  $r_{1A}$ . In addition, the different perforations of the two system backbones need to result in the adequate mass ratio  $\gamma$ . All these aspects must be considered and will be covered in more detail in the following.

## 7.1 Mechanical stiffness

To obtain the physical dimensions of the elastic beam structures corresponding to the optimized stiffness coefficients, a finite element analyses was carried out. In contrast to the calculations described in Chapter 5, the aim is not to produce force displacement plots for a given geometry, but to find a geometry for a given force displacement relation.

## 7.2. Electrostatic restoring force and mass ratio

The basic shape of the three springs is specified by the design of the oscillator shown in Fig. 6.1. As the optimized linear stiffness coefficients  $k_{01}$  and  $k_{02}$  have distinct values, their corresponding beams have different dimensions as well. Moreover, the resulting beam structures should provide equal displacements when deflected to the right and left hand side. In the case of the single degree of freedom MEMS oscillator shown in Fig. 5.1, this condition is fulfilled due to the vertical symmetry of the design. To achieve the same for the present system design, the design of the springs  $k_{01}$  and  $k_{02}$  has to be changed to a fixed-fixed configuration as shown in Fig. 5.4 b). Taking a fixed-fixed beam with a pre-set cross-section into consideration, the only free adjustable dimension is the length of the beam itself. Performing an FEM-assisted parameter study to obtain the beam lengths corresponding to the optimized linear stiffness values  $k_{01}^{lin}$  and  $k_{02}^{lin}$  results in force displacement plots 7.1 a) and c). The resulting beam lengths related to the plots are listed in Table 7.1.

Spring	Linear stiffness coefficient	Nonlinear stiffness coefficient	Beam length
$k_{01}$	$2.083\mu\text{N}/\mu\text{m}$	$0.35\mu\text{N}/\mu\text{m}^3\mu\text{N}$	$510\mu\text{m}$
$k_{12}$	$1.465\mu\text{N}/\mu\text{m}$	0	$400\mu\text{m}$
$k_{02}$	$7.979\mu\text{N}/\mu\text{m}$	$1.453\mu\text{N}/\mu\text{m}^3\mu\text{N}$	$320\mu\text{m}$

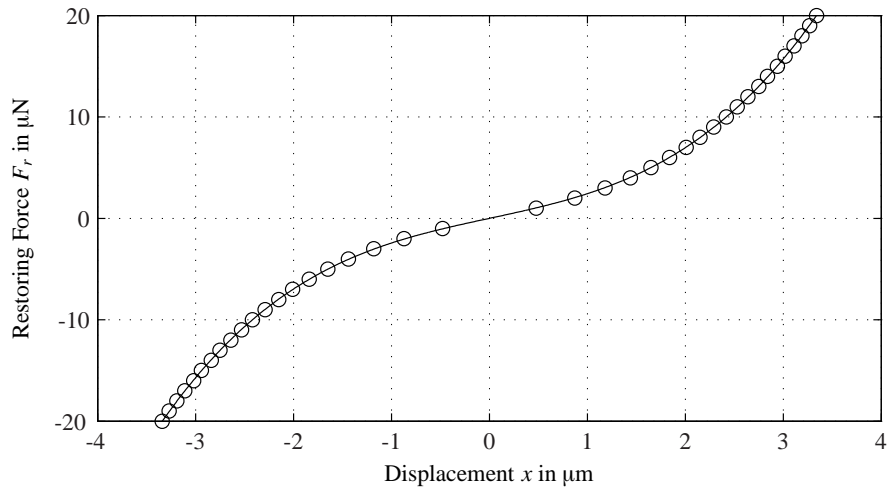
Table 7.1: Calculated beam lengths for springs  $k_{01}$ ,  $k_{12}$  and  $k_{02}$  using finite element analysis.

As spring  $k_{12}$  is a combination of two folded beams, the resulting structure provides equal displacements for push and for pull forces. By defining the length of the folded part and performing another FEM-assisted parameter study, the length of the beam structure is obtained. Figure 7.1 b) shows the resulting force displacement plot and the related beam length is stated in Table 7.1. As already evidenced by Fig. 5.5, the folded beam configuration provides smaller nonlinear mechanical coefficients than the fixed-fixed configuration. In the case of spring  $k_{12}$ , the combination of two folded beams results in a purely linear equivalent mechanical stiffness, indicated by the resulting linear force displacement relation.

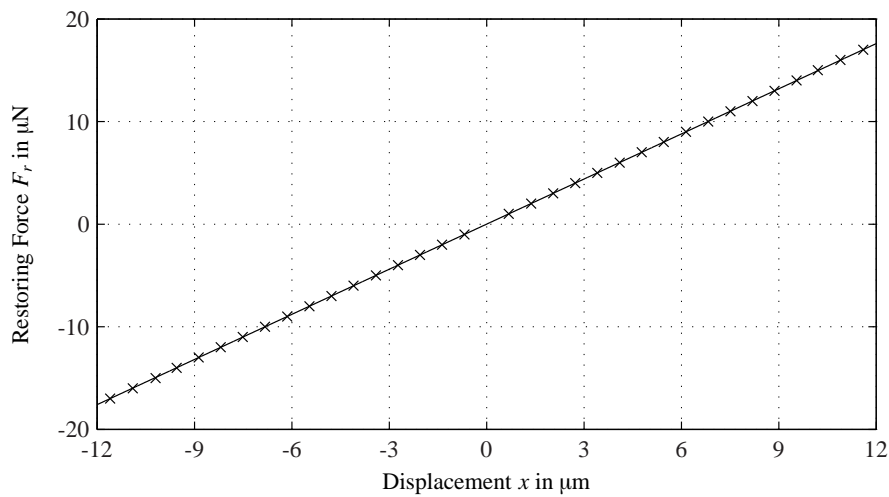
## 7.2 Electrostatic restoring force and mass ratio

The value of the optimized linear electrostatic coefficient is just slightly different from the non-optimized one and still lies in between the numerical calculation results summarized in

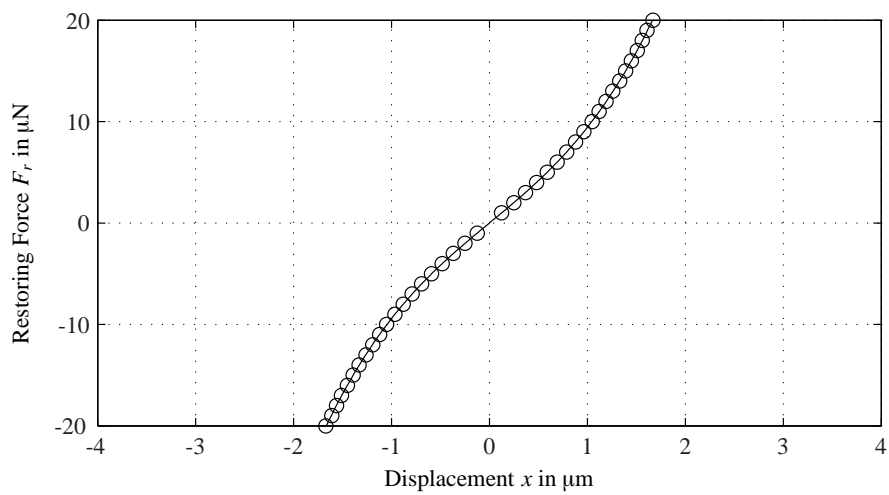
## 7.2. Electrostatic restoring force and mass ratio



(a) Calculated nonlinear force displacement relation for spring  $k_{01}$ .



(b) Calculated nonlinear force displacement relation for spring  $k_{12}$ .



(c) Calculated nonlinear force displacement relation for spring  $k_{02}$ .

Figure 7.1: Calculated nonlinear force displacement relations for springs  $k_{01}$ ,  $k_{12}$  and  $k_{02}$  using finite element analysis.

### 7.3. Damping

Table 5.5. As both calculations are based on the same comb drive design, it can be applied for the optimized design without any modification. That results in an oscillator consisting of two sets of non-interdigitated comb drives with 128 misaligned comb fingers each. The dimensions of the comb drive are stated in the right hand column of Table 5.4.

To achieve the desired mass ratio of  $\gamma = 2$ , the dimensions of the second backbone (represented by  $m_2$ ) needs to be different from the first backbone (represented by  $m_1$ ). If the same perforation is applied to both backbones, the thickness  $T_B$  or the depth  $D_B$  of the later structure needs to be changed. If the feature depth is kept at  $12\mu\text{m}$  and the thickness at  $2\mu\text{m}$ , the width of the rectangles to be removed  $L_{BE}$  (see Fig. 5.6), may be decreased.

## 7.3 Damping

The numerical studies concerning the damping coefficients have shown that the occurrence of the first anti-resonance has well pronounced maxima. That result, along with condition (3.1.3), indicates the vital importance of damping to the occurrence of parametric resonances and anti-resonances. As it is not practical to define a certain value of damping to be implemented into the oscillator, the aim of the parameter optimization concerning the damping coefficients is to analyze the impact that damping has on the stability behavior of the system. A more detailed investigation concerning damping may take place after the manufacturing of a MEMS prototype similar to the present MEMS oscillator, involving several experiments and measurements.

## 7.4 Oscillator design

If the optimized linear system parameters are transformed into an oscillator design, one obtains the basic layout shown in Fig. 7.2. As previously mentioned the two outer springs are replaced by two beams in a fixed-fixed configuration compared to the original folded design shown in Fig. 6.1.

The corresponding dimensions to the design depicted in Fig. 7.2 are stated in Table 7.2, whereas the complete set of optimized parameters is summarized in Table 7.3. As both backbone structures are represented schematically, a certain perforation needs to be applied in order to achieve the desired masses  $m_1$  and  $m_2$ . The design of both comb drives is shown in Fig. 5.6 with its corresponding dimensions stated in the right hand column of Table 5.4.

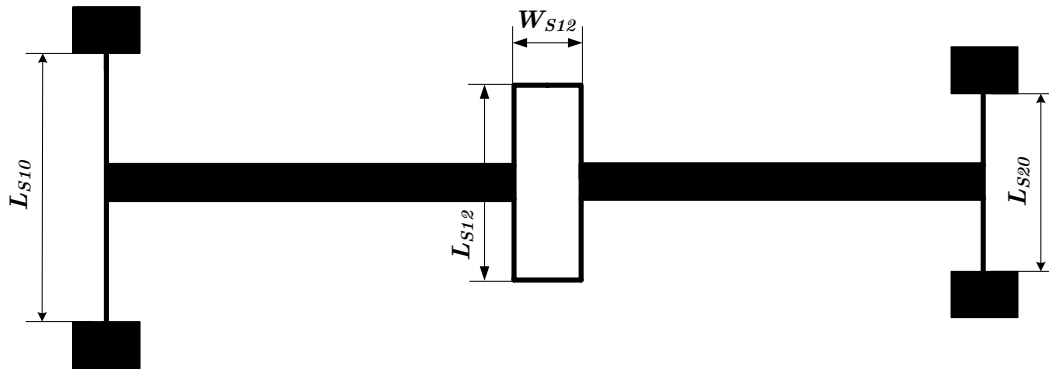


Figure 7.2: MEMS design proposal for maximum occurrence of the anti-resonance effect.

Parameter	Value	Dimension unit
Width of springs	2	$\mu\text{m}$
Width of backbone	20	$\mu\text{m}$
Length of backbone	400	$\mu\text{m}$
Depth	12	$\mu\text{m}$
$L_{S10}$	510	$\mu\text{m}$
$L_{S12}$	400	$\mu\text{m}$
$L_{S20}$	320	$\mu\text{m}$
$W_{S12}$	40	$\mu\text{m}$

Table 7.2: Optimized dimensions of the two degree of freedom MEMS oscillator.

Parameter	Value	Dimension unit
$m_1$	$1.8 \times 10^{-10}$	kg
$m_2$	$3.6 \times 10^{-10}$	kg
$c_{01}$	$6.0 \times 10^{-8}$	Ns/m
$c_{12}$	$6.0 \times 10^{-8}$	Ns/m
$c_{02}$	$4.0 \times 10^{-7}$	Ns/m
$k_{01}^{lin}$	2.083	$\mu\text{N}/\mu\text{m}$
$k_{12}^{lin}$	1.465	$\mu\text{N}/\mu\text{m}$
$k_{02}^{lin}$	7.979	$\mu\text{N}/\mu\text{m}$
$k_{01}^{nlin}$	0.35	$\mu\text{N}/\mu\text{m}^3$
$k_{12}^{nlin}$	0	
$k_{02}^{nlin}$	1.453	$\mu\text{N}/\mu\text{m}^3$
$r_{1A}$	$3.8 \times 10^{-4}$	$\mu\text{N}/\text{V}^2\mu\text{m}$
$r_{3A}$	$-1.69 \times 10^{-5}$	$\mu\text{N}/\text{V}^2\mu\text{m}^3$
$V_A$	16	V

Table 7.3: Optimized system parameters of the two degree of freedom MEMS.

#### 7.4. Oscillator design

To keep the computational time within a reasonable limit, the number of simulation runs for the FEM-assisted parameter studies was limited. This is why the linear mechanical stiffness coefficients stated in Table 7.3 do not exactly match the ones obtained through the parameter study described in Chapter 6.2.2.

## Conclusions and future work

Parametric excitation may provide desirable features when applied to mechanical systems as shown in [5]. Considering microelectromechanical systems, so far parametric excitation is mainly used to take advantage of parametric resonances. Such systems basically consist of a comb drive connected to a single degree of freedom oscillator. The investigations described in Chapter 6 suggest that the usage of MEMS oscillators with two degrees of freedom provides additional benefits compared to a design with just a single degree of freedom. Not only are the regions where parametric resonances occur increased, but also a very interesting parametric anti-resonance phenomenon appears. This effect may be used to introduce additional vibration damping to the system, in order to enhance the systems stability.

The numerical parameter study carried out in Chapter 6.2.2 shows that the anti-resonance effect is quite sensitive to changes within the system parameters. It also indicates that a certain optimum exists wherein the occurrence of that effect reaches a maximum. That optimum is approximated by a parameter study where the influence of the parameters among each other has been neglected. The transformation of the optimized system parameters to an actual design is depicted in Fig. 7.2, which is intended to be the starting point for further investigations. They will require that some additional issues are addressed. An adequate manufacturing technology needs to be found considering that both backbones, including the elastic folded beams in between, provide a relatively long self-supporting structure of about 840  $\mu\text{m}$ . Depending on that manufacturing technology the MEMS material needs to be defined. As for the finite element analyses polycrystalline silicon is assumed, the stiff-

ness calculations need to be adapted, if a different material is selected. Actual measurement of the systems vibrations may be complicated by the fact that the system only performs in-plane motion. Hence the needed equipment is rather complex. In [7] the authors describe a fiber-optic laser Doppler vibrometer to dynamically measure in-plane motion of MEMS. As an alternative the measurement can be carried out using a CCD camera based system. Such a method is discussed in [18].

In conclusion, the detection of the parametric anti-resonance phenomenon in a micro-electromechanical system is a first step showing the potential benefits that this effect can have on such systems.

# Bibliography

- [1] Adams S.G., Bertsch F.M., Shaw K.A., MacDonald N.C.: *Independent tuning of linear and nonlinear stiffness coefficients*. Journal of Microelectromechanical Systems, 7(2):172-180, 1998.
- [2] Cartmell M.: *Introduction to Linear, Parametric and Nonlinear Vibrations*. London, Chapman and Hall, 1990.
- [3] DeMartini B.E., Rhoads J.F., Turner K.L., Shaw S.W., Moehlis J.: *Linear and Nonlinear Tuning of Parametrically Excited MEMS Oscillators*. Journal of Microelectromechanical Systems, 16:310-318, 2007.
- [4] Ecker H.: *Parametric excitation in engineering systems*. Proceedings of COBEM, Gramado, RS, Brazil, 2009.
- [5] Ecker H.: *Suppression of self-excited vibrations in mechanical systems by parametric stiffness excitation*, ARGESIM, Wien, 2005.
- [6] Ghodssi R., Lin P.Y.: *MEMS Materials and Processes Handbook*. Springer, 2011.
- [7] Kim M.G., Jo K., Kwon S.H., Jang W., Park Y., Lee J.H.: *Fiber-optic laser Doppler vibrometer to dynamically measure MEMS actuator with in-plane motion*. Journal of Microelectromechanical Systems, 18:1365-70, 2009.
- [8] Madou M.J.: *Fundamentals of Microfabrication*. 2nd ed., CRC Press, 2002.
- [9] Maluf N., Williams K.: *An Introduction to Microelectromechanical Systems Engineering*. Artech House, 2004.

## Bibliography

- [10] Mukherjee S., MacDonald N.C.: *Optimal shape design of an electrostatic comb drive in microelectromechanical systems*. Journal of Microelectromechanical Systems, 7(1):16-26, 1998.
- [11] Narducci M., Figueras E., Lopez M.J., Gracia I., Fonseca L., Santander J., Cane C.: *A High Sensitivity Silicon Microcantilever Based Mass Sensor*. IEEE Sensors Conference, 1127-1130, 2008.
- [12] Raskin J.P., Brown A.R., Khuri-Yakub B., Rebeiz G.M.: *A novel parametric-effect MEMS amplifier*, Journal of Microelectromechanical Systems, 9(4):528-537, 2000.
- [13] Rhoads J.F., Shaw S.W., Turner K.L., Moehlis J., DeMartini B.E., Zhang W.: *Generalized Parametric Resonance in Electrostatically Actuated Microelectromechanical Oscillators*. Journal of Sound and Vibration, 296(4-5):797-829, 2006.
- [14] Rhoads J.F., Shaw S.W., Turner K.L., Baskaran R.: *Tunable MEMS filters that exploit parametric resonance*. ASME Journal of Vibration and Acoustics, 127(5):423-430, 2005.
- [15] Rugar D., Grutter P.: *Mechanical parametric amplification and thermomechanical noise squeezing*. Phys. Rev. Lett., 67(6):699-702, 1991.
- [16] Sharpe W.N.: *Mechanical properties of MEMS materials*. in: M. Gad-el-Hak (Ed.), The MEMS Handbook, CRC Press, Boca Raton, FL, 2002.
- [17] Shaw S.W., Turner K.L., Rhoads J.F., Baskaran R.: *Parametrically excited MEMS-based filters*. Proceedings of the IUTAM Symposium on Chaotic Dynamics and Control of Systems and Processes, 137-146, 2003.
- [18] Teyssieux D., Euphrasie S., Cretin B.: *MEMS in-plane motion/vibration measurement system based CCD camera*. Measurement, 44(10):2205-2216, 2011.
- [19] Verhulst F.: *Methods and applications of singular perturbations*. Springer, 2005.
- [20] Yie Z., Zielke M.A., Burgner C.B., Turner K.L.: *Comparison of parametric and linear mass detection in the presence of detection noise*. Journal of Micromechanics and Microengineering, 21, 2011.

- [21] Zhang W., Baskaran R., Turner K.L.: *Effect of cubic nonlinearity on auto-parametrically amplified resonant MEMS mass sensor*. Sensors and Actuators A: Physical, 102(1-2):139-150, 2002.
- [22] Zhang W., Turner K.L.: *A mass sensor based on parametric resonance*. Proceedings of the Workshop on Solid-State Sensors and Actuators, 49-52, Hilton Head, South Carolina, 2004.
- [23] Zhang W., Turner K.L.: *Frequency tuning and control of parametrically resonant mass-sensors*. Journal of Vacuum Science and Technology A, 23(4):841-845, 2005.